The Effects of Gravitational Wave Recoil in Giant Elliptical Galaxies

---

Nader Khonji
Supervisor: Dr. Alessia Gualandris
Co-Supervisor: Prof. Justin Read

Astrophysics PhD
University of Surrey
2025-07-19

Summary

Scouring by supermassive black hole (SMBH) binaries is the most accepted mechanism for the formation of the cores seen in giant elliptical galaxies. However, an additional mechanism is required to explain the largest observed cores. A likely mechanism is gravitational wave (GW) recoil, which is expected to naturally occur following SMBH mergers.

We model core formation by both scouring and recoil, performing N-body simulations of galactic mergers of multicomponent galaxies, based on the observed parameters of massive elliptical galaxies with cores > 0.5 kpc. After scouring is complete, the SMBHs are merged and given a GW recoil kick of between 0.1 and 0.9 of the escape speed (v_{esc}) of the remnant galaxies. We confirm that binary scouring forms cores < 1.3 kpc in size, but find that recoil kicks with $< 0.5\, v_{\mathrm{esc}}$ are necessary to form the largest cores. Furthermore, we find that large kicks leave a unique signature of a flat core in the 3D stellar density, and that stars bound to the SMBH remnant after smaller kicks can be dragged back to the centre, forming a cusp in the density profile within the flattened core. This new 'black hole dragging' mechanism may explain the apparent nuclear star clusters observed at the centres of some galaxies with large cores.

Finally, as a first step towards predicting whether GW recoil has occurred in observed giant elliptical galaxies, we refit the surface brightness profiles of 24 galaxies with cores $>$ 0.5 kpc using a single (core-Sérsic) model. This self-consistent dataset lays the foundation for harnessing the presence of flat cores and/or apparent nuclear star clusters to empirically constrain the black hole recoil velocity distribution function. This, in turn, will provide constraints on the distribution function of black hole spin in the most massive black holes.

Declaration

This thesis and the work to which it refers are the results of my own efforts. Any ideas, data, images or text resulting from the work of others (whether published or unpublished, and including any content generated by a deep learning/artificial intelligence tool) are fully identified as such within the work and attributed to their originator in the text, bibliography or in footnotes. This thesis has not been submitted in whole or in part for any other academic degree or professional qualification. I agree that the University has the right to submit my work to the plagiarism detection service TurnitinUK for originality checks. Whether or not drafts have been so-assessed, the University reserves the right to require an electronic version of the final document (as submitted) for assessment as above. [1]. Chapter 3 is based on the published paper:

- **Chapter 3**: Nader Khonji, Alessia Gualandris, Justin I. Read, Walter Dehnen. The Astrophysical Journal, Volume 974, Issue 4, 2024 October 20, Pages 204-219.

Chapter 4 has been submitted to The Astrophysical Journal, has received favourable reviewer comments, and will be resubmitted shortly:

- **Chapter 4**: Nader Khonji, Alessia Gualandris, Justin I. Read, Walter Dehnen.

Signature

20th May 2025

Date

---

[1] This declaration is not in my own words but was downloaded from `https://surrey-content.surrey.ac.uk/sites/default/files/2023-07/statement-of-originality-declaration.docx`

Acknowledgements

First and foremost, I would like to express my deepest gratitude to my supervisors, Dr. Alessia Gualandris and Prof. Justin Read, for their invaluable guidance and support throughout this project.

I would like to acknowledge support from the Science and Technology Facilities Council, whose generous funding made this work possible.

I would also like to thank all members of the Astrophysics Department, for making my time at the University of Surrey so memorable and enjoyable, not least the evenings at the King's Head!

Finally, I would like to thank my family. To my wife Deborah, thank you for helping me through the challenges of the last few years, and for your encouragement and support to change to a career in the field I am most passionate about. To my children, Hannah, Harrison and Laurelin, thank you for managing so well all the times Dad was working instead of being with you! I am very lucky that we all remain so close.

Contents

List of Figures

List of Tables

Chapter 1

Introduction

In this chapter, I present the key background material necessary to understand the rest of this thesis work. In 1.1, I begin with a review of the Standard Cosmological Model and hierarchical formation of structure. Then, in 1.2, I consider the main theories of formation for elliptical galaxies, before discussing their light profiles, including the presence of cores in larger galaxies, and how the profiles are modelled. In 1.3, I discuss the nature of black holes and theories for their formation and growth. Next, in 1.4, I move on to the scaling relations of elliptical galaxies, the evidence for supermassive black holes (SMBHs) in their nuclei, and the scaling relations between SMBHs and their host galaxies. In 1.5, I examine the phases of core formation, and the likely mechanisms involved, including the established 'binary scouring' method and the possibility of gravitational wave (GW) recoil. The latter is discussed in more detail in 1.6, before the chapter concludes with an outline and motivation for the remainder of this thesis in 1.7.

1.1 Cosmology

1.1.1 Cosmology and Galaxy Formation

The vast majority of the baryons in the Universe are in the intergalactic medium, with only $\sim 18\%$ in a 'collapsed phase', as galaxies and their groups or clusters (Shull et al., 2012), and just $\sim 10\%$ of these in elliptical galaxies (Driver et al., 2007). Despite this, and their wide range in sizes from dwarfs to giants, elliptical galaxies dominate the stellar mass function above $\sim 10^{10.5}\,\mathrm{M}_\odot$ (Figure 1.1, Thanjavur et al., 2016). To understand why requires a theory of both cosmology and galaxy formation.

Galaxies were classified by Hubble (1926), after he confirmed the extragalactic nature of 'nebulae'. With extremely limited knowledge available, his classification was based on their shape as seen in projection on the plane of the sky, following the longstanding practice for regular nebulae (Herschel, 1847). There were three main types, elliptical, spiral, and the intermediate lenticular (S0). The latter has the spiral's disky morphology but not its characteristic spiral arms. Elliptical galaxies are also known as early-type galaxies, as they were originally thought to develop into the (late-type) spiral galaxies (Jeans, 1928) and thus Hubble (1936) placed them in the 'early' part of his tuning fork diagram.

Initial 'top-down' theories envisioned the formation of elliptical galaxies from primordial gas, via hydrodynamic processes (Strömberg, 1934), fragmentation (Von Weizsäcker, 1951; Hoyle, 1953), or direct collapse (Eggen et al., 1962). At this time, the scientific community was still divided between proponents of the 'steady-state' theory (Bondi & Gold, 1948), in which matter was continuously created to maintain a constant density, despite

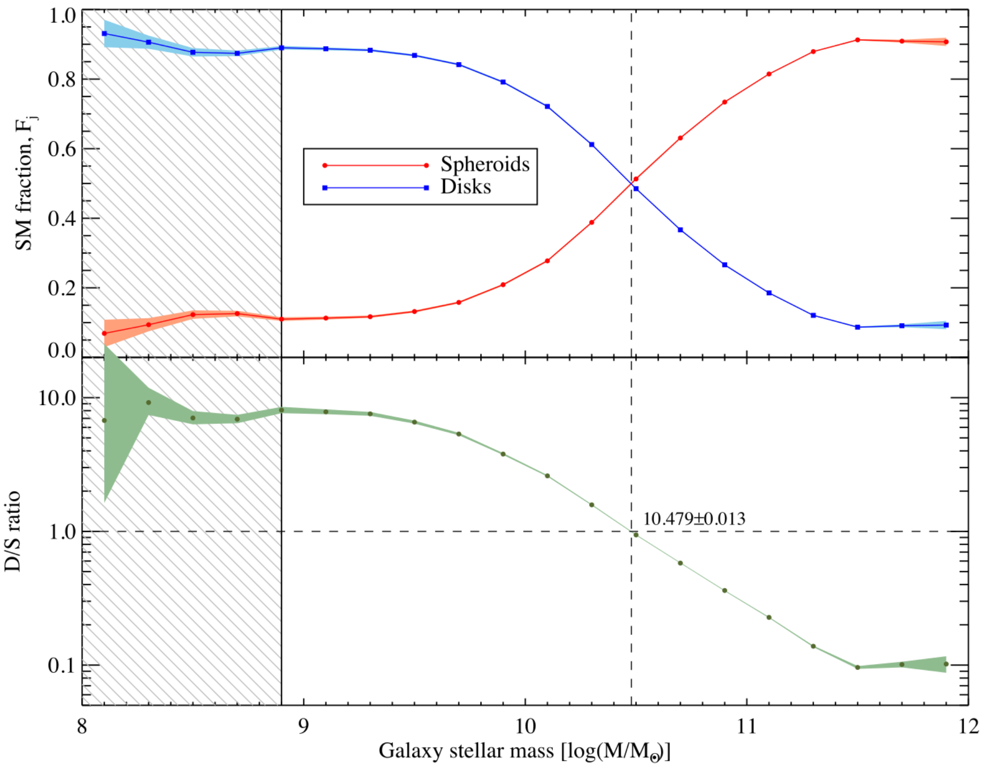

Figure 1.1: The stellar mass function showing the relative contribution of spheroids and disks in galaxies (top) and relative fraction of disc/spheroid mass (bottom). From Thanjavur et al. (2016).

expansion of the Universe (Hubble, 1929), and the 'Big Bang' model (Lemaître, 1931) of its expansion from an infinitely dense singularity. However, the serendipitous discovery of the cosmic microwave background (CMB, Penzias & Wilson, 1965) shifted the balance decisively in favour of the latter.

Peebles (1965) immediately linked the CMB to galaxy formation, as radiation pressure would prevent gravitational collapse of density perturbations. After recombination, the timing of the collapse would depend on the Jeans scale (Gamow, 1954). Silk (1968) showed that that the perturbations would be damped by photons before recombination, such that the collapse would occur later.

Dark matter, proposed by Zwicky (1933) after his observation of missing mass in the Coma cluster, became more accepted during the 1970s, with the discovery of flat galaxy rotation curves (Rubin & Ford Jr, 1970; Rubin et al., 1980). Theory (Peebles, 1982) and simulations (White et al., 1983) suggested that the particles involved were slow-moving cold dark matter (CDM). In the 1990s, the first evidence of accelerated expansion of the Universe was found from observations of Type 1a supernovae (Riess et al., 1998; Perlmutter et al., 1999), leading to the adoption of a cosmological constant (Λ) or 'dark energy'. The combination of these theories resulted in the development of the ΛCDM model of cosmology and the 'bottom-up' theory of galaxy formation described in the next section.

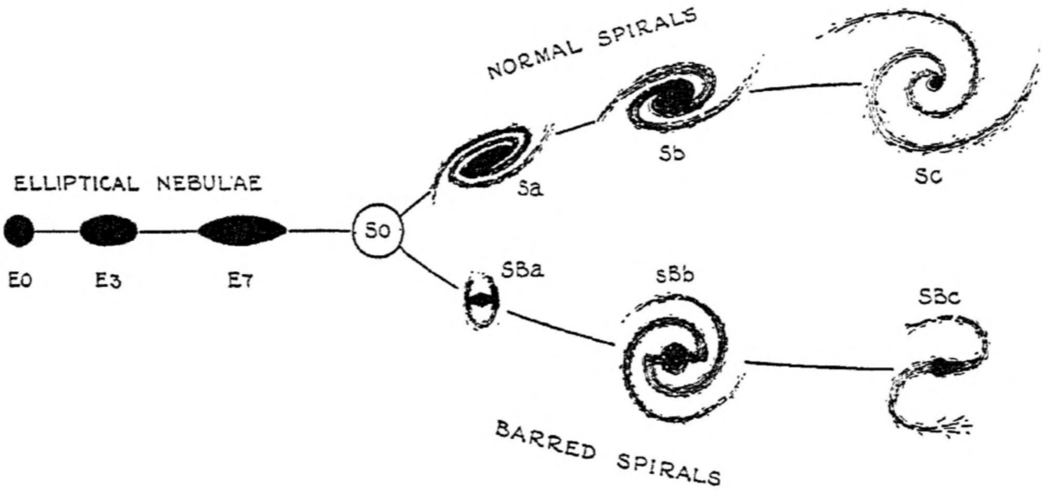

Figure 1.2: Hubble's sequence of nebular types. From Hubble (1936).

1.1.2 Hierarchical structure formation

Whilst the discovery of the CMB answered some cosmological questions, it also gave rise to new problems. These include the homogeneous nature of the CMB between regions that were too widely spaced to be causally related ('the horizon problem', Rindler, 1956; Weinberg, 1972), and the high degree of fine-tuning required to result in a flat universe ('the flatness problem', Dicke R. H. and Peebles P. J. E. in Hawking & Israel, 1979). Inflation (Guth, 1981), a period of exponential growth of the early Universe, was proposed to solve these issues. An important sequel of this rapid expansion is that quantum fluctuations in the inflaton field are 'frozen' as they leave the horizon. As inflation ends, they re-enter as matter density fluctuations (Starobinsky, 1982; Guth & Pi, 1982).

In CDM models of cosmology, the density perturbations grow linearly until a critical point, when CDM condenses before the warmer baryonic matter to form halos (Press & Schechter, 1974; Bardeen et al., 1986). After recombination and sufficient cooling (Rees & Ostriker, 1977), baryonic gas falls into their potential wells, to eventually form visible galaxies (Navarro & White, 1993). Tidal torques during the collapse of the gas clouds generates angular momentum (Hoyle et al., 1949). Although initial simulations indicated this was not conserved due to dissipative processes (Navarro & Benz, 1991), inclusion of supernova feedback boosted the angular momentum (Thacker & Couchman, 2001), resulting in disc-shaped galaxies consistent with observations. Density waves passing through the discs are believed to give rise to spiral structure (Lin & Shu, 1964). Interestingly, the formation of spiral galaxies seems to occur earlier than previously thought: Recent observations with the James Webb Space Telescope (Ferreira et al., 2022) show ~ 10 times more spiral galaxies at $z > 1.5$ than were seen in Hubble Deep Field observations Williams et al. (1996).

Gravity then drives the hierarchical formation of structure in the Universe (Blumenthal et al., 1984), with mergers of the halos into successively larger structures (White & Rees, 1978). This eventually leads to galaxy cluster formation and the possibility of mergers between visible galaxies.

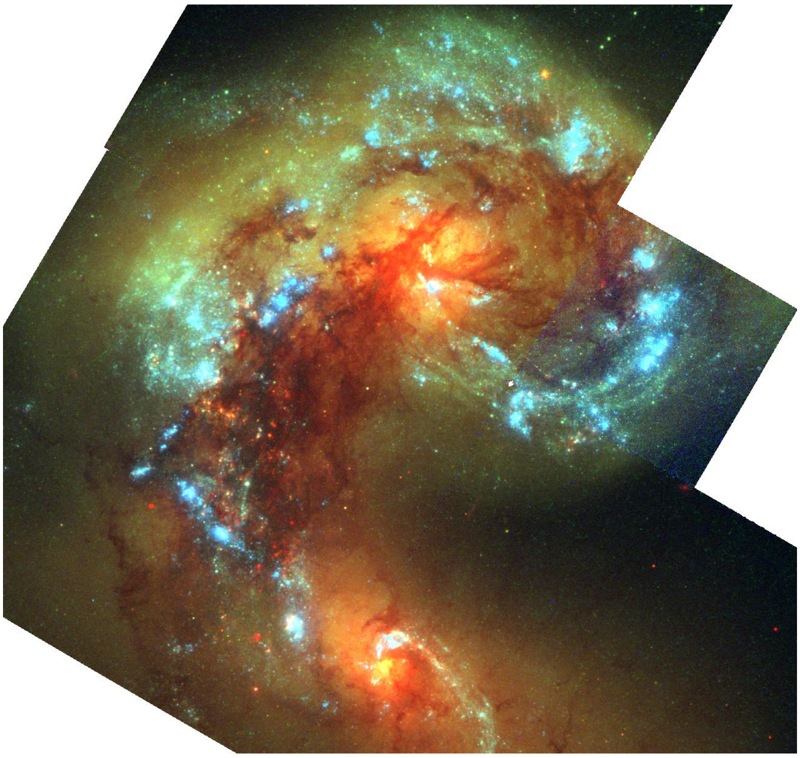

Figure 1.3: The 'Antennae Galaxies' NGC 4038/4039. From the Hubble Legacy Archive (Archive, 2024).

1.2 Elliptical galaxies

1.2.1 Formation theories

The morphology-density relation (Oemler, 1974; Davis & Geller, 1976), and the morphology-radius relation in galaxy clusters (Dressler, 1980), show that galaxies in denser environments are more likely to be elliptical, and those in less dense regions or isolated galaxies are more likely to be spirals. Moore et al. (1996) proposed multiple high-speed encounters or 'galaxy harassment' as an explanatory mechanism. Stripping of gas by such repeated encounters could also result in S0 galaxies (Bekki & Couch, 2011). However, intermediate redshift spiral galaxies do not show the distortion expected from such a mechanism (Couch et al., 1998), and isolated S0 galaxies exist. Hence, the most likely mechanism for the transformation in morphology from spirals to ellipticals is galaxy mergers (Toomre & Toomre, 1972).

Major mergers, those between galaxies of similar mass, of spiral galaxies were first proposed by Toomre & Toomre (1972) as a mechanism for the formation of elliptical galaxies. This mechanism has three phases: (i) tidal friction, due to gravitational interaction between the galaxies, causes distortion and formation of galactic tails; (ii) the resulting transfers of energy and angular momentum lead to orbital decay; (iii) the rapidly changing gravitational field produces violent relaxation, the redistribution of orbits into an equilibrium configuration (Lynden-Bell, 1967), producing the characteristic featureless shape of a pressure-supported elliptical galaxy. Alternatively, elliptical galaxies could arise from mixed (spiral-elliptical) or spheroidal (elliptical-elliptical) mergers (Khochfar & Burkert, 2003), or repeated minor mergers (Bournaud et al., 2007).

Clear evidence of tidal friction in action can be seen in observations of galaxy pairs such as the 'Antennae Galaxies' NGC 4038/4039 (Figure 1.3, Rubin et al., 1970; Whitmore & Schweizer, 1995). However, further important observational evidence of elliptical galaxy formation mechanisms can be found from their observed light profiles. Parameterisation of these profiles is key to understanding and comparing them, and so this will be described in detail in the following section.

1.2.2 Light profiles

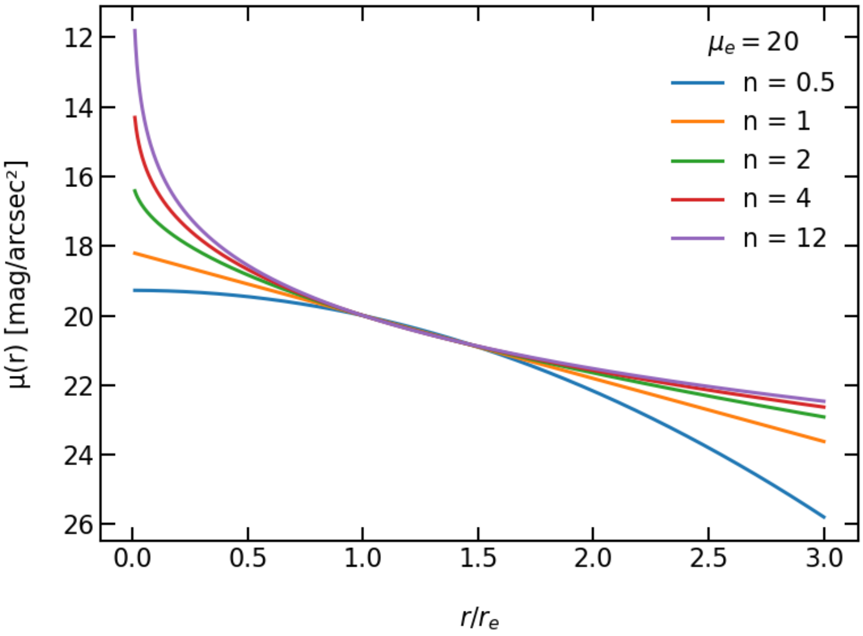

Figure 1.4: Sérsic profiles of magnitude μ against radius r as a function of effective radius r_e, for various values of Sérsic index n, with μ_e, the magnitude at r_e, set to 20, typical for a giant elliptical galaxy.

The first attempt at parameterising an elliptical galaxy light profile was made by Hubble (1930), shortly after his classification of galaxies. He described their surface brightness I as function of radius r as:

$$I = \frac{I_0}{(\frac{r}{a}+1)^2}\,. \tag{1.1}$$

This uses just two parameters, the central surface brightness I_0, and a scale radius parameter a, and has the disadvantages that it does not approximate the light profiles of ellipticals well at large radii, which decline more quickly than an inverse square, and that it implies an infinite total mass.

These problems were addressed by the de Vaucouleurs (1948) profile:

$$\log I = \log I_0 - 3.25\,[(r/a)^{1/4} - 1]\,, \tag{1.2}$$

which can be written in terms of the half-light radius r_e and the surface brightness at this radius I_e:

$$\log I = \log I_e + 7.67\,[1 - (r/r_e)^{1/4}]\,. \tag{1.3}$$

Although this fitted some ellipticals well (e.g. NGC 3379, de Vaucouleurs & Capaccioli, 1979), it could not adapt to fainter dwarf ellipticals, which have flatter central profiles and faster decline at larger radii (e.g. NGC 185, Hodge, 1963). A better solution was the generalised version of the de Vaucouleurs profile by Sérsic (1963):

$$\log I = \log I_e - b_n \left[(r/r_e)^{1/n} - 1 \right], \tag{1.4}$$

which adopts an index n and a function b_n. The latter obeys $\Gamma(2n) = 2\gamma(2n, b_n)$, where Γ and γ are the Gamma and lower incomplete Gamma functions respectively, but can be approximmated by $2n - 0.324$. The resulting profile is identical to the de Vaucouleurs for $n = 4$. If the value of n is lowered, the profile becomes flatter when $r < r_e$, but steeper when $r > r_e$, to match the profiles of faint ellipticals, with $n = 1$ giving an exponential profile (Figure 1.4).

More luminous ellipticals often have a steeper central rise and more gradual decline at large radii, which is better matched to Sérsic profiles with a higher values of n, typically 4-10 (see e.g. Graham & Driver, 2007). However, when the central arcsecond could be resolved, King (1978) examined the light profiles of 17 of the largest known elliptical galaxies and found that, rather than continuing to increase as a cusp, they were flattened to form a 'core'. These giant galaxies are often found in the densest regions of the Universe, at the centre of galaxy clusters ('cD' galaxies in Morgan's classification, Matthews et al., 1964). The central surface brightness initially appeared to be constant, prompting King to apply his isothermal model of globular clusters (King, 1966). However, as resolution continued to improve, it was found that surface brightness actually continues to increase towards the centre in almost all cases, but that there is a correlation between the size of the core and the galaxy's luminosity (Lauer, 1985; Kormendy, 1985).

With the advent of the Hubble Space Telescope (HST), resolution increased to $\sim 0.05''$, corresponding to a few parsecs for nearby galaxies. Ferrarese et al. (1994) confirmed that it was brighter ellipticals which tended to have cores. Lauer et al. (1995) published an analysis of the profiles of 45 elliptical galaxies using HST images and classified them into two groups: 'core galaxies' which 'break' from a steep outer power law to a shallow inner cusp; and 'power-law galaxies' with profiles steadily rising as a cusp to the resolution limit. They introduced their 5-parameter 'Nuker' profile:

$$I = 2^{(\beta-\gamma)/\alpha} \, I_b \, (r_b/r)^{\gamma} \left[1 + (r/r_b)^{\alpha} \right]^{(\gamma-\beta)/\alpha}, \tag{1.5}$$

which could be fitted to both types. Here, β and γ are the outer and inner logarithmic slopes, respectively, I_b is the intensity at the 'break radius' r_b, which is the point at which the slope is the mean of β and γ, and α controls the sharpness of transition between them (Figure 1.5).

In addition, observations indicated a correlation with galaxy morphology and dynamics. Core galaxies tend to be anisotropic, with box-shaped isophotes and low rotation, whereas cuspy galaxies tend to be isotropic, with disc-shaped isophotes and high rotation (Kormendy & Bender, 1996; Faber et al., 1996). The distribution of central structure was initially thought to be a dichotomy. Indeed, Lauer et al. (1995) defined core galaxies as those with $\gamma < 0.3$ and $r_b > 0.01''$, and power-law galaxies as those with $\gamma > 0.5$, but it now appears to be bimodal (Lauer et al., 2007).

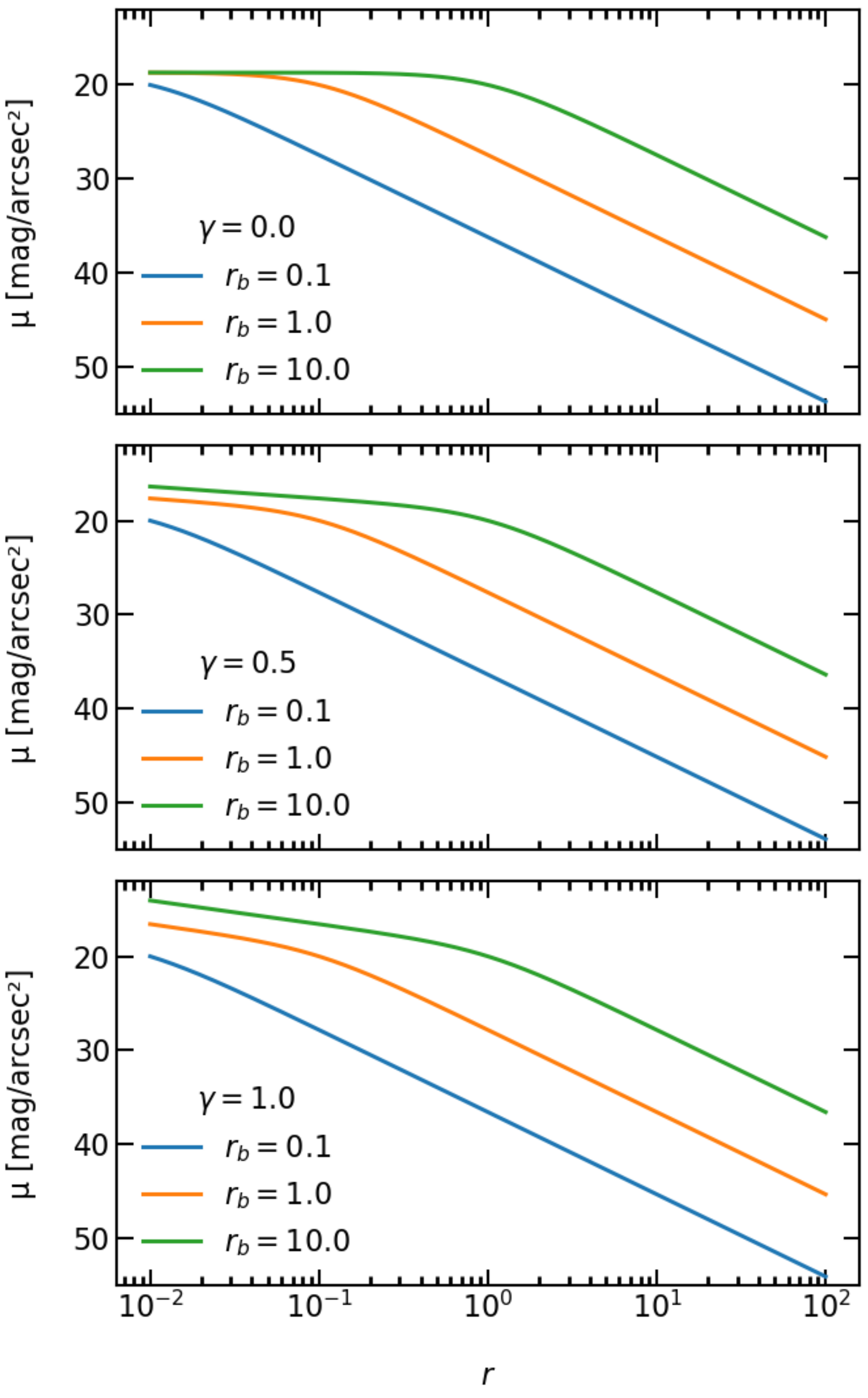

Figure 1.5: Nuker profiles for γ of 0.0 (top), 0.5 (middle) and 1.0 (bottom) with varying core sizes r_b. Here, α is set to 2, β to 3.5, and the magnitude at the break radius μ_b to 20. The outer slope falls as a power law.

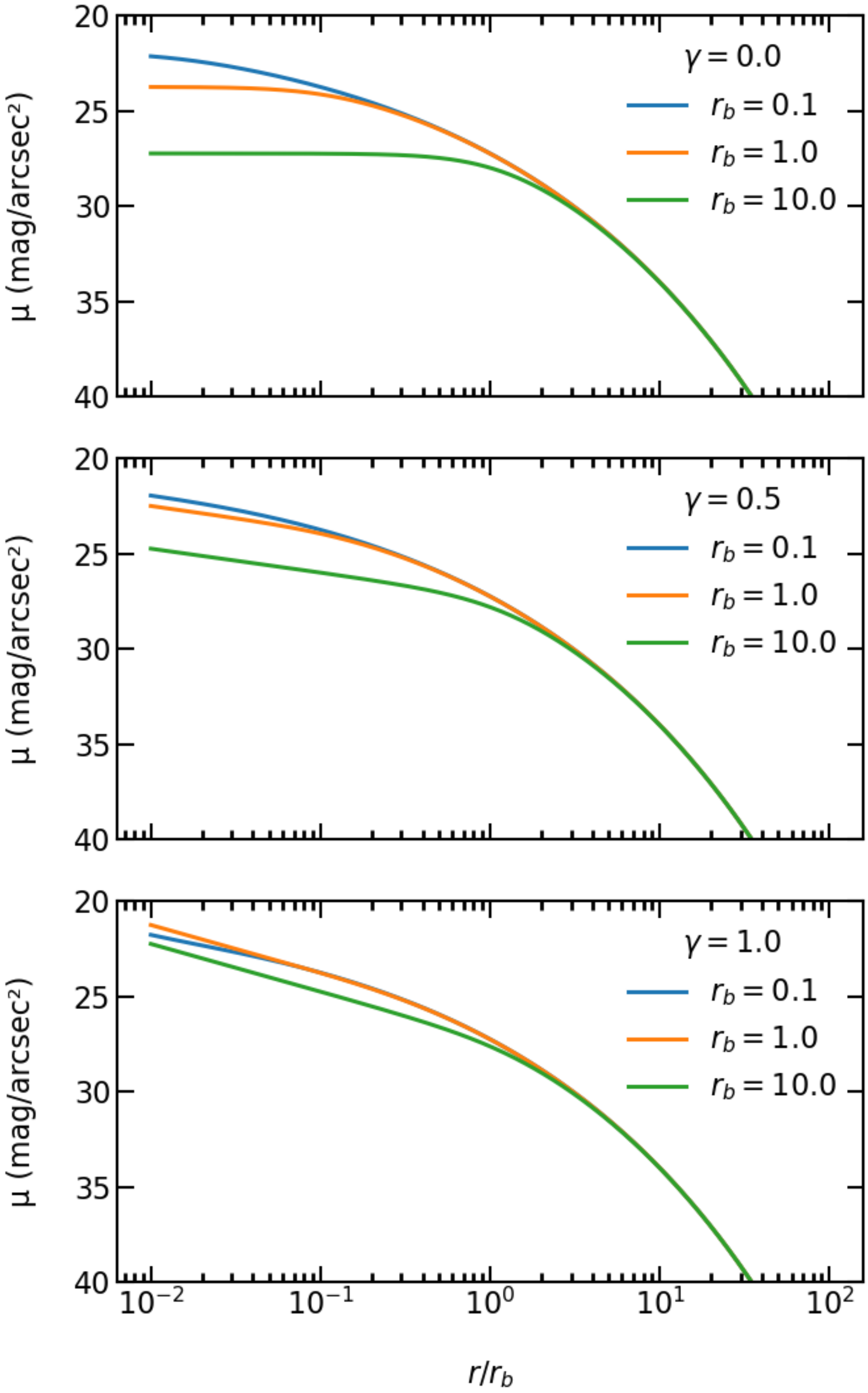

Figure 1.6: As Figure 1.5 but for the core-Sérsic profile, with $n = 3.5$. Here, the outer slope falls as a Sérsic profile.

However, the outer part of the stellar bulge is better fitted by a Sérsic profile than a power law, and so Graham et al. (2003) proposed combining the Nuker and Sérsic models to give a combined 'core-Sérsic profile' (Figure 1.6):

$$I = I' \left[1 + \left(\frac{r_b}{r} \right)^{\alpha} \right]^{\frac{\gamma}{\alpha}} \exp \left(- b_n \left[\frac{r^{\alpha} + r_b^{\alpha}}{r_e^{\alpha}} \right]^{\frac{1}{\alpha n}} \right), \tag{1.6}$$

where now α controls the sharpness between the inner power law and outer Sersic profiles, r_e is the half-light radius of the profile outside the transition region, and I' is related to I_b by:

$$I' = I_b \, 2^{-\gamma/\alpha} \exp \left[b_n \left(\frac{2^{1/\alpha} r_b}{r_e} \right)^{\frac{1}{n}} \right]. \tag{1.7}$$

In both the Nuker and core-Sérsic models, r_b represents the size of the core and γ the inner logarithmic slope. However, Rest et al. (2001) noted that, for small α, the value of γ in the Nuker profile does not correspond to the slope of the profile just below the core radius, but that much further in, potentially below the resolution limit. Hence, they introduced an additional parameter γ', the gradient of the profile at $0.1''$. Clearly, γ' will correspond to different radii at different distances, and can result in the same profile shape having different values at different distances, even to the extent of changing its classification between core and cusp. Graham et al. (2003) also showed that r_b can vary by a factor of three, depending on the radial range used for the fit, which may also be dependent on distance due to the fixed HST aperture. The Core-Sérsic profile attempts to minimise these issues by its use of a curved outer profile and normalisation to r_e.

The presence of cores in giant elliptical galaxies naturally leads to the question of what mechanism leads to their formation. The theories of their formation rely on relations between elliptical galaxy parameters and the presence of black holes (BHs).

1.3 Black holes and their formation

Dense stars from whose gravity light could not escape were first theorised by Michell (1784), but it was Wheeler (1968) who introduced the term 'black hole' for these objects. Schwarzschild (1916) found the simplest solution to the Einstein Field Equations of General Relativity applicable to BHs, assuming a spherical distribution of mass which has neither charge nor angular momentum. The Schwarzchild metric has a true singularity at the origin $r = 0$ and a coordinate singularity at the Schwarzchild radius $r_s = 2GM_\bullet/c^2$, corresponding to the 'event horizon' of the BH. It has an interior solution for $0 < r < r_s$ and an exterior solution for $r > r_s$.

Astrophysical SMBHs do have angular momentum (Kerr, 1963), and are described by the next most simple solution, the Kerr metric. In fact, the no-hair theorem states that they can be completely described by their mass and spin (Robinson, 1975). BH spin is usually represented by the dimensionless spin parameter $a = cJ/GM^2$, ranging from 0 for a non-spinning BH to 1 for maximal spin, and where J and M are the SMBH angular momentum and mass, respectively.

There is now overwhelming evidence for the existence of supermassive black holes (SMBHs), with masses $\gtrsim 10^6 \mathrm{M}_\odot$, at the centre of galaxies (see Section 1.4). There is also good observational evidence of stellar-mass BHs: many X-ray binaries, consisting of a BH or neutron star and a companion star, have been observed (Liu et al., 2006, 2007); mergers of stellar-mass BHs can be detected by their gravitational wave (GW) emission. In fact, the first GW observation was of just such a merger (Abbott et al., 2016).

However, there is a paucity of observational evidence for intermediate-mass BHs between these extremes. There is also a theoretical mass gap for BHs between 50-130 $M_\odot$, as stars in this mass range are predicted to undergo pair-instability supernovae leaving no remnant (Woosley & Heger, 2021). Hence, there is still much uncertainty as to how SMBHs develop.

The theories of SMBH formation are divided into those involving their growth from stellar origin light seeds of mass $\sim 10^2$ $M_\odot$, and those from heavy seeds of 10^3-10^5 $M_\odot$ (Latif & Ferrara, 2016; Regan & Volonteri, 2024). Light seeds would have originated from Population III stars (Kashlinsky & Rees, 1983). Several theories have been proposed for heavy seeds, including direct collapse of gas (Umemura et al., 1993; Begelman et al., 2006), repeated stellar mergers inside dense young star clusters (Portegies Zwart et al., 2004), and infall of BHs by dynamical friction (Boco et al., 2020, see Section 1.5). The seeds would then grow by a combination of accretion and mergers.

The classic model of accretion by Shakura & Sunyaev (1973) describes a geometrically thin but optically thick disc. Accretion is allowed up to the Eddington limit (Eddington, 1926), where there is a balance between the gravitational infall of gas and the radiation pressure of emission from the accretion disc. However, the limit is exceeded in 'super-Eddington' models such as the 'slim disc' (Abramowicz et al., 1988; Sadowski, 2009), where the optical thickness and rapid advection of gas traps photons, reducing the effective radiation pressure.

There are recent observations of higher mass ($\gtrsim 10^9$ $M_\odot$) SMBHs than expected at high redshifts ($z \gtrsim 7$, e.g. Mortlock et al., 2011; Wang et al., 2019, 2021), and giant elliptical galaxies with 10^9-10^{10} $M_\odot$ SMBHs (e.g. McConnell et al., 2011; Dullo et al., 2021) with stars that formed at $z \gtrsim 1$ (e.g. Thomas et al., 2005; Saracco et al., 2020). Such early development of SMBHs favours a heavy seed origin or accelerated growth of light seeds through mergers and/or super-Eddington accretion.

1.4 Scaling relations

Faber & Jackson (1976) discovered the first scaling relation for elliptical galaxies, between luminosity L and velocity dispersion σ:

$$L \propto \sigma^\eta \,. \tag{1.8}$$

with $\eta \sim 4$. However, when a wider range of luminosities was observed, η was found to vary from ~ 2 for faint ellipticals (Davies et al., 1983) to ~ 5 for more luminous galaxies ($M_\mathrm{b} < -20.5$, Schechter, 1980).

Kormendy (1977) found a relation between half-light radius r_e and mean surface brightness (using the magnitude scale) at that radius μ_e:

$$\mu_e \propto \log r_e \,, \tag{1.9}$$

so that smaller ellipticals are brighter at r_e.

In fact, both the dynamical Faber-Jackson and photometric Kormendy relations can be regarded as projections of a fundamental plane which links all three quantities (Dressler et al., 1987; Djorgovski & Davis, 1987):

$$\log r_e = 1.39(\log \sigma + 0.26\mu_e) - 6.71 \,. \tag{1.10}$$

The existence of such empirical relations is unsurprising, since elliptical galaxies are self-gravitating systems in approximate dynamic equilibrium. The properties of such systems are governed by the virial theorem (Clausius, 1870):

$$2T + U = 0 \tag{1.11}$$

where T and U are the total kinetic and potential energies of the system, respectively. For an elliptical galaxy with total mass M, using $T \sim M\sigma^2$ and $U \sim -GM^2/r_e$ gives:

$$M \propto \sigma^2 r_e \tag{1.12}$$

Clearly, the luminosity of the galaxy is related to the amount of stellar mass it contains, and so the virial theorem explains the origin of the relations in fundamental plane. However, the plane is tilted from the prediction of the virial theorem. This appears to be predominantly because the M/L ratio varies with both stellar populations and dark matter (DM) content. Massive elliptical galaxies are likely to have higher metallicities (Tremonti et al., 2004), more bottom-heavy initial mass functions (van Dokkum & Conroy, 2010), and higher DM content (Loewenstein & White III, 1999) than smaller ellipticals, resulting in a higher M/L ratio. However, the lack of homology also plays a role, with smaller galaxies tending to have lower Sérsic index (Caon et al., 1993) and to be more rotationally supported (Kormendy & Bender, 1996).

Although not explicitly mentioned, the presence of a massive BH and its deep potential well would certainly also influence these relations. It had long been suspected that a supermassive black hole (SMBH) may be present in the nucleus of large galaxies. Emission lines from galaxies had been discovered early in the 20th century (Slipher, 1917), and studied systematically by Seyfert (1943). With the development of radio astronomy, a discrete source was discovered in Cygnus (Hey et al., 1946; Bolton & Stanley, 1948), closely followed by optical confirmation of such sources in elliptical galaxies (Bolton et al., 1949). However, Matthews & Sandage (1963) found a radio source that was a stellar object rather than a galaxy. Its emission lines could not be identified until Schmidt (1963) realised that they were highly redshifted. It was postulated that these extremely luminous quasi-stellar objects (QSOs) were observations of accretion onto SMBHs (Salpeter, 1964; Lynden-Bell, 1969), which became known as active galactic nuclei (AGNs).

The search began for other evidence of SMBHs in galactic nuclei, including galaxies without AGNs, where it seemed likely that ‘dormant’ SMBHs would be present. This included the centre of our own galaxy, where Balick & Brown (1974) detected a strong radio source, which became known as Sagittarius A* (SgrA*, Brown, 1982). Young et al. (1978) and Sargent et al. (1978) used stellar velocity measurements to calculate the first dynamical mass of an SMBH. Using more modern techniques, there is now overwhelming dynamical evidence for an SMBH in many galaxies. Stellar kinematics is now performed using integral field spectroscopy and dynamical models with three integrals of motion (e.g. Verolme et al., 2002). Other techniques include gas kinematics (e.g. Macchetto et al., 1997), reverberation mapping (Peterson, 1993) and masers (Miyoshi et al., 1995).

More direct evidence followed, with the first observation of an accretion disc in NGC 4261 (Jaffe et al., 1993) and the detection of extreme proper motions of SgrA* (Eckart & Genzel, 1997). Finally, the Event Horizon Telescope (Akiyama et al., 2019) released images of the SMBH candidate in M87, a giant ellptical galaxy in the Virgo cluster, followed by SgrA* (Akiyama et al., 2022). These images showed a central shadow surrounded by an accretion disc (Figure 1.7).

SMBH masses were initially measured using stellar dynamics. Dressler & Richstone

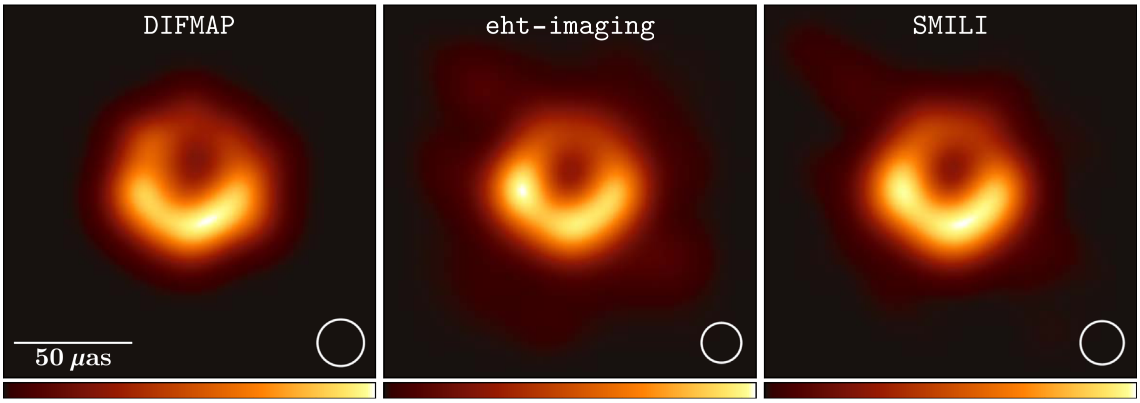

Figure 1.7: Fiducial images from the three pipelines of the Event Horizon telescope. From Akiyama et al. (2019).

(1988) used one such technique to suggest a relation between the mass of the black hole $M_\bullet$ and the spheroid luminosity $L_{\rm sph}$ of galaxies. They used Doppler broadening of spectroscopic Ca II triplet lines, which is strong in old stellar populations, to determine line-of-sight stellar velocities. These were then compared with 'maximum entropy' dynamical models (Richstone & Tremaine, 1988) to find the most likely SMBH mass. Dressler & Richstone (1988) used the relation, together with their $\sim 10^7 M_\odot$ and $\sim 10^8 M_\odot$ masses for the M32 dwarf galaxy and M31 disc galaxy respectively, to predict that the brightest ellipticals would have SMBHs with masses $\sim 10^9 M_\odot$, consistent with QSO models. Later, gas dynamics, in addition to stellar measurements, and HST imaging were used, leading to confirmation of the $M_\bullet$-$L_{\rm sph}$ relation (McLure & Dunlop, 2002).

Similarly, a relation was found between $M_\bullet$ and spheroid mass $M_{\rm sph}$ (Magorrian et al., 1998; Marconi & Hunt, 2003). Interestingly, although both were initally thought to be linear, later studies indicate this is only the case for core galaxies, with power law galaxies having significantly steeper relations for both $L_{\rm sph}$ (Graham & Scott, 2013) and $M_{\rm sph}$ (Scott et al., 2013).

A much tighter relation was found between $M_\bullet$ and σ (Figure 1.8, Ferrarese & Merritt, 2000; Gebhardt et al., 2000), of the form:

$$M_\bullet \propto \sigma^\kappa \,. \tag{1.13}$$

This has been regarded as a fundamental relationship due to its low scatter of $\lesssim 0.3$ dex. The value of κ in the initial studies varied from 3.75 to 5, but Tremaine et al. (2002) found this was due to systematic errors in the velocities used. More recent studies show $\kappa \sim 5$ (McConnell & Ma, 2013; Graham & Scott, 2013). Interestingly, Greene & Ho (2006) found a larger scatter at the low end of the relation, using reverberation mapping of Hα lines in active galaxies. Reverberation mapping uses the time delay between variations in the continuum emission from the geometrically thin accretion disc and broad line[1] region (BLR) outside it to calculate the radius of the latter $r_{\rm BLR}$. By combining this with the velocity dispersion of the gas σ_g, the virial mass of the black hole is estimated as:

$$M_\bullet = \frac{f\sigma_g^2 r_{\rm BLR}}{G} \,, \tag{1.14}$$

---

[1] Broad lines are spectral emission lines such as Hα and Hβ, which are broadened by the action of the Doppler effect on emission from fast-moving gas.

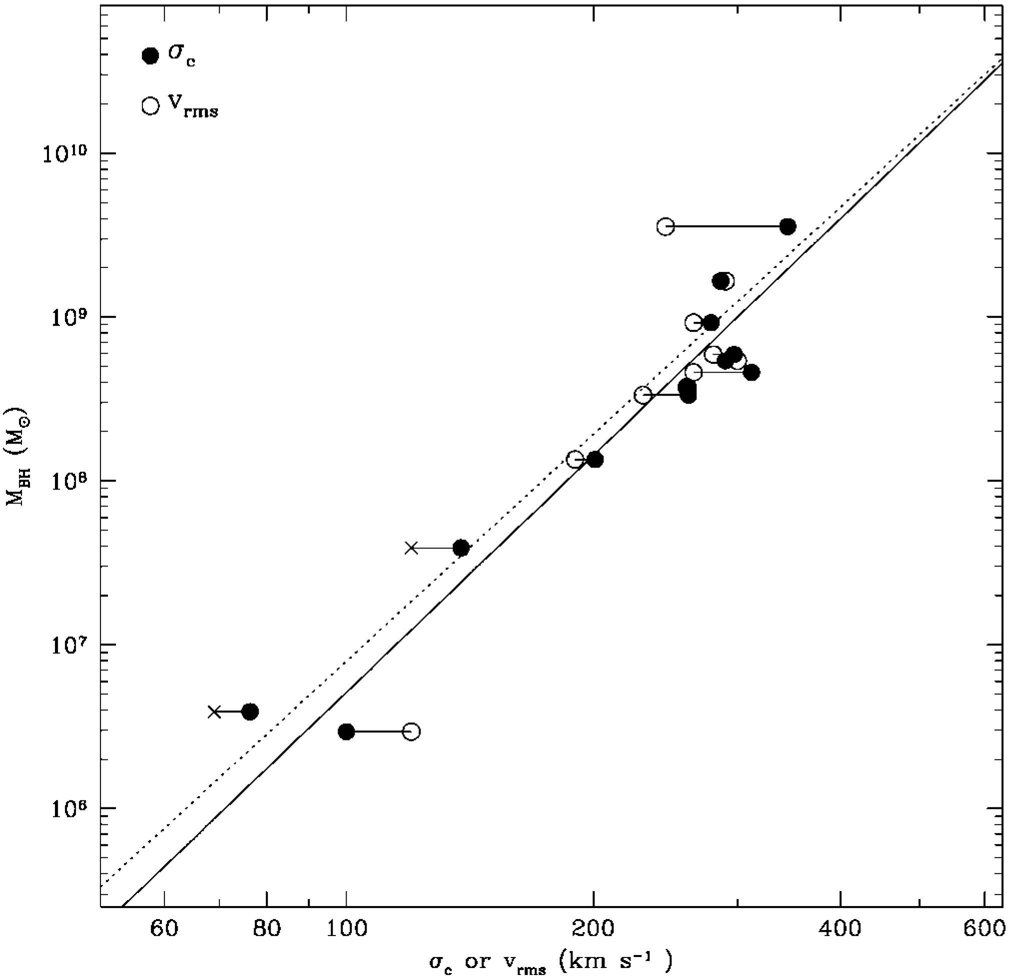

Figure 1.8: Original $M_\bullet$-σ relation from Ferrarese & Merritt (2000).

where f is a scaling factor based on the geometry of the BLR.

This scatter was confirmed by Xiao et al. (2011) in a more recent study (Figure 1.9. The reason for the increased scatter is unclear, but may be related to the lack of bulges or presence of pseudobulges in disc galaxies, the effects of different growth histories, or increased uncertainties in measurements.

Finally, a $M_\bullet$-n relation was found which initially appeared log-linear (Graham et al., 2001). However, further data suggest it may be log-quadratic (Graham & Driver, 2007), with less extreme masses at either end of the scale.

These relations provide strong evidence for the ubiquity of SMBHs and their coevolution with their host galaxies. However, it is important to note that they only apply to spheroidal components, and not discs or pseudobulges (Kormendy et al., 2011). The relations may also be used to predict SMBH masses, but there are limitations here also. Despite the low scatter of the $M_\bullet$-σ relation, σ appears to peak at $\sim$ 300km s^{-1} for $M_\bullet \gtrsim 10^9 M_\odot$, but $L_{\rm sph}$ continues to increase. Hence, the latter appears to be a better predictor of $M_\bullet$ for high-mass galaxies (Lauer et al., 2007). These galaxies are also the most likely to have cores. Dullo (2019) found a correlation of $r = 0.92$ between core size, as fitted using the core-Sérsic profile, and $M_\bullet$ for 11 galaxies with directly measured masses, with $R_b \propto M_\bullet^{0.83\pm0.10}$. In comparison, the $M_\bullet$ calculated by both σ and $L_{\rm sph}$ were systematically lower. This raises the possibility that core size may be the best predictor

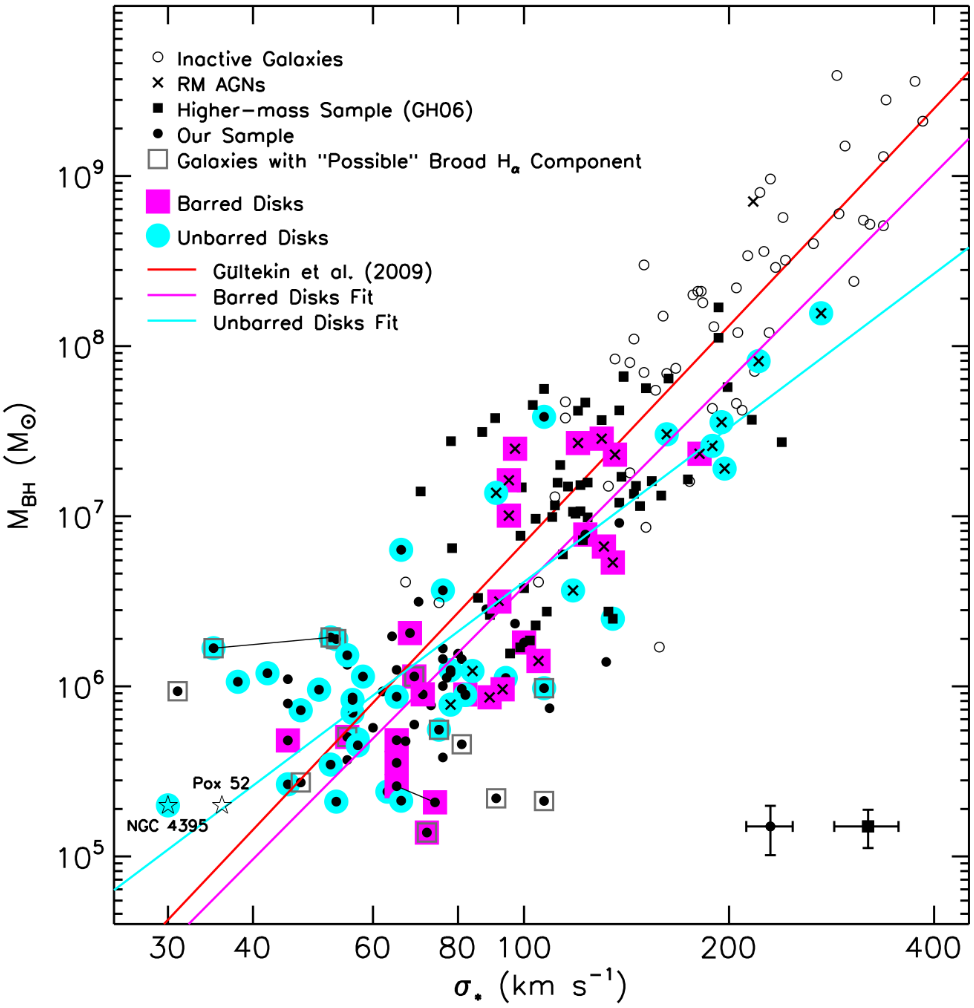

Figure 1.9: More recent $M_\bullet$-σ relation from Xiao et al. (2011). Black squares show the data from Greene & Ho (2006) and the red line is the relation from Gültekin et al. (2009).

of $M_\bullet$ for these largest galaxies.

1.5 Core formation

As explained in Section 1.2.1, giant elliptical galaxies are likely to form during a merger of two galaxies. If the progenitors are galaxies containing large amounts of gas, such as spiral galaxies, star formation will be triggered by the merger and a cuspy profile will inevitably result (Kormendy & Sanders, 1992; Mihos & Hernquist, 1994). Hence, if cores form during mergers, the progenitors would need to be gas-poor ellipticals. However, early simulations using stellar particles only did not form cores (Farouki et al., 1983). This agrees with Dehnen (2005), who showed that when two systems with cuspy profiles are mixed, the steepest cusp is retained in the remnant. However, Section 1.4 shows that each galaxy is likely to contain an SMBH, and this appears to be the key to core formation; simulations of mergers of galaxies with SMBHs develop cores (Ebisuzaki et al., 1991).

Begelman et al. (1980) described the mechanisms involved in three stages: (i) dynamical friction leading to the formation of a black hole binary (BHB); (ii) ejection of stars in

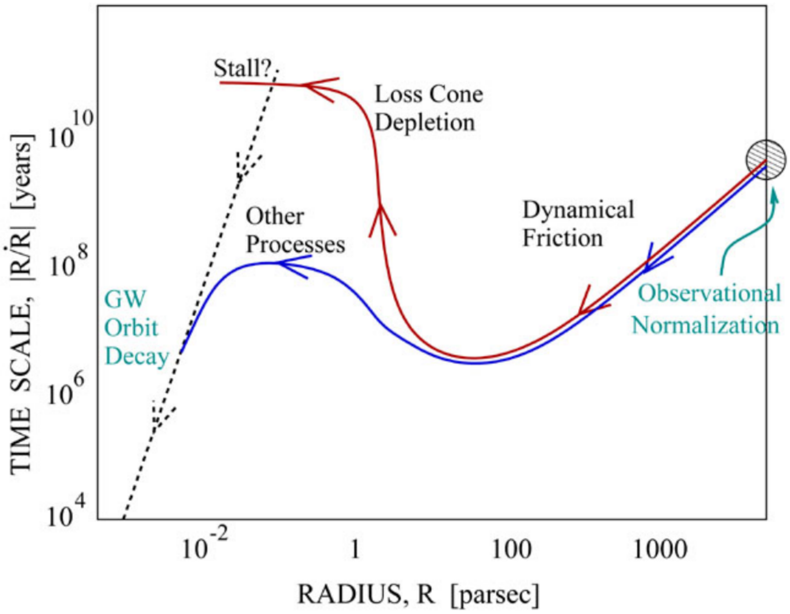

Figure 1.10: The phases of SMBH binary evolution: dynamical friction, binary scouring and loss cone refilling (here labelled 'other processes') and GW emission. From Celoria et al. (2018).

three-body interactions with the BHB binary; and (iii) gravitational wave (GW) emission resulting in coalescence of the binary (Figure 1.10).

Dynamical friction (Chandrasekhar, 1943) is the dominant process at kiloparsec scales, when the SMBHs are widely separated during the initial phase of the merger. As each much more massive SMBH moves through the field of lighter stars and dark matter, they are pulled to form a 'gravitational wake' behind it, with the energy and angular momentum transfer slowing the SMBH, allowing it to sink into the potential well of the remnant (Antonini & Merritt, 2011). Dynamical friction ends when the separation of the SMBHs reaches a_f, the influence radius of the secondary (i.e. lower mass) SMBH, forming a gravitationally bound BHB (Valtaoja et al., 1989). a_f is defined as the separation at which the enclosed stellar mass M_enc is twice the secondary SMBH mass m_2:

$$M_\mathrm{enc}\,(r < a_\mathrm{f}) = 2m_2\,. \tag{1.15}$$

Short range (parsec-scale) three-body interactions between stars and the BHB begin to dominate (Quinlan, 1996; Sesana et al., 2006), leading to the ejection of stars and the increase in binding energy of the BHB (Hills, 1983). This rapid hardening continues until the specific binding energy exceeds the specific kinetic energy (Milosavljević & Merritt, 2001) at the hard binary separation:

$$a_\mathrm{h} = \frac{G\mu}{4\sigma^2}\ , \tag{1.16}$$

where μ is the reduced mass[2] of the BHB and σ is the stellar velocity dispersion. This process, which leads to a central mass deficit (Merritt, 2006), is known as 'binary scouring' and has been shown to occur in simulations (e.g. Quinlan, 1996; Milosavljević & Merritt,

---

[2] $\mu = m_1 m_2/(m_1 + m_2)$ for SMBH masses m_1 and m_2.

2001; Gualandris & Merritt, 2012),

If mergers are to contribute to the coevolution of galaxies and SMBHs described in **??**, the BHB should proceed to coalescence. The final loss of energy and angular momentum required for it to do so can only be achieved by GW emission. GWs are produced by systems with a varying mass quadrupole moment (Flanagan & Hughes, 2005). Hence, a massive astrophysical binary system should produce relatively large amplitude waves, but the power radiated will only become significant when the binary separation reaches milliparsec scales (Peters & Mathews, 1963). Such BHBs should be strong sources of nanohertz GWs, which are detectable using pulsar timing arrays (PTAs; (e.g. Foster III, 1990), Sesana et al. 2018) Recently, the European PTA with the Indian PTA (Antoniadis et al., 2023), the North American Nanohertz Observatory for GWs (NANAOgrav) (Agazie et al., 2023), the Chinese PTA (Xu et al., 2023) and the Parkes PTA (Reardon et al., 2023), released exciting evidence for a stochastic nanohertz GW background (GWB). The signal is consistent with that of a population of BHBs evolving due to GW inspiral (Antoniadis et al., 2023).

There is a potential problem that has to be overcome for the BHB to reach small enough separations. Binary scouring has been shown to preferentially remove stars on low angular momentum orbits (Thomas et al., 2014). These stars populate a region in phase space known as the 'loss-cone' (Figure 1.11, Merritt, 2013). If the loss-cone becomes depleted, the hardening of the binary would stall. Since this would be at around parsec scales, this became known as the 'final parsec problem' (Milosavljević & Merritt, 2003). Stalling would be likely in a spherically symmetric system, since refilling of the loss-cone can only occur by collisional two-body relaxation, which typically takes longer than a Hubble time (Makino & Funato, 2004; Berczik et al., 2005). However, all merger remnants are somewhat triaxial (Bortolas et al., 2018a), and Gualandris et al. (2017) and Vasiliev et al. (2015) showed that if the galaxy was even mildly triaxial (e.g. axis ratios $1 : 0.9 : 0.8$), the loss cone would be refilled efficiently and hardening could continue.

Although binary scouring is the most established mechanism for core formation, other mechanisms have been proposed for their formation and/or enlargement. Most cores are relatively small, from parsecs to a few hundred parsecs in size, but a minority have been observed to have very large core sizes of ~ 0.5-3.8 kpc (Dullo, 2019; Alamo-Martínez & Blakeslee, 2017). Alternative mechanisms may be particularly relevant in these extreme cases.

If a constant density core is already present, Read et al. (2006) showed that a massive infalling object could not continue to transfer energy and angular momentum to the surrounding stars by dynamical friction, and would stall at the edge of a core. This 'stalled perturber' would enlarge the core and could result from a minor merger. Another possible mechanism for large core formation is multiple SMBHs Kulkarni & Loeb (2012), where a further merger occurs before coalescence of the BHB. Finally, GW recoil could result in the formation of large cores. This will be described in detail in the next section.

1.6 Gravitational wave recoil

Directly following the merger, there should be enormous GW emission from the SMBH remnant (Press, 1971), which reduces as it relaxes to an equilibrium state, a process known as 'ringdown' (Berti et al., 2018). Indeed, the recent first detection of GWs was the signal from the merger of a stellar mass black hole binary (Abbott et al., 2016).

In addition to energy and angular momentum, GWs carry linear momentum (Bondi et al., 1962; Sachs, 1962). If the GW emission is asymmetric, momentum conservation

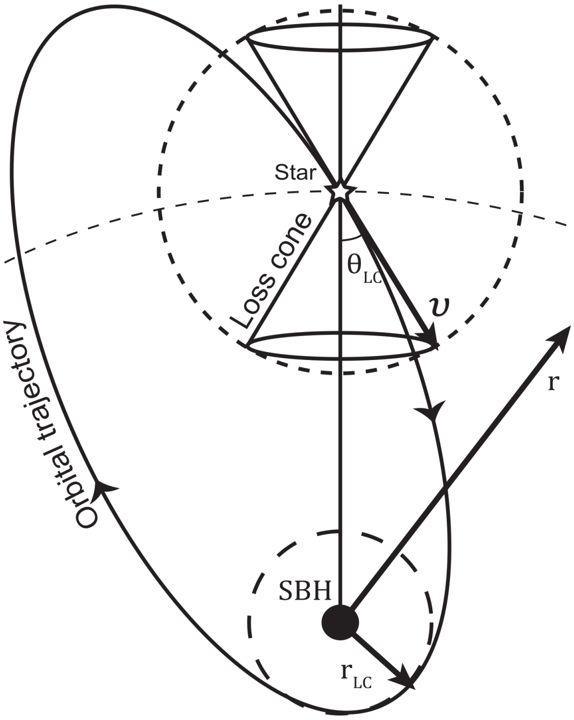

Figure 1.11: The loss-cone: the set of velocity vectors that correspond to orbits that will be captured by the SMBH. From Merritt (2013).

would lead to 'recoil' of the remnant. Bekenstein (1973) used linearised gravitational wave theory to calculate the recoil when a stellar core collapses asymmetrically to a black hole. Fitchett (1983) extended this to calculate the linear momentum flux after the merger of a circular binary system and found a recoil velocity of $\sim 1480\,\mathrm{km\ s^{-1}}$. However, the perturbative approach has significant limitations here, and a strong-field method is necessary for an accurate calculation of recoil.

A breakthrough resulted from the development of 'numerical relativity' techniques, such as the method by Pretorius (2005) using harmonic coordinates. In the non-spinning case, the kick velocity v_k depends solely on the SMBH mass ratio $q = m_2/m_1 \leq 1$. Here, Gonzalez et al. (2007) found the maximum v_k is relatively low at $\sim 175\,\mathrm{km\ s^{-1}}$ at $q \approx 0.36$. Furthermore, v_k drops off either side of this ratio, falling to zero for $q = 1$ (Figure 1.12).

Astrophysical SMBHs which grow from accretion are expected to be spinning Thorne (1974), and this case behaves quite differently, as here v_k scales as q^2 and hence is maximal for $q = 1$. v_k is also very sensitive to the configuration of the spins; if aligned and anti-aligned with the orbital plane, the recoil velocity peaks at $\sim 4000\,\mathrm{km\ s^{-1}}$ (Campanelli et al., 2007b). The most extreme case occurs when the components of the spin in the orbital plane are of equal magnitude but opposite in sign, and the components perpendicular to the plane are equal in both magnitude and sign. Here, they can reach $5000\,\mathrm{km\ s^{-1}}$ (Figure 1.14, Lousto & Zlochower, 2011), clearly exceeding the escape speed v_esc for the galaxy (Merritt et al., 2004).

Ejection of a SMBH remnant could lead to transfer of energy to and ejection of surrounding stars (Redmount & Rees, 1989), and simulations by Boylan-Kolchin et al. (2004) showed that this could be an additional mechanism for core formation. In the more common case that $v_\mathrm{k} < v_\mathrm{esc}$, Gualandris & Merritt (2008) showed that the remnant and core would oscillate back and forth about their common centre of mass, gradually becoming

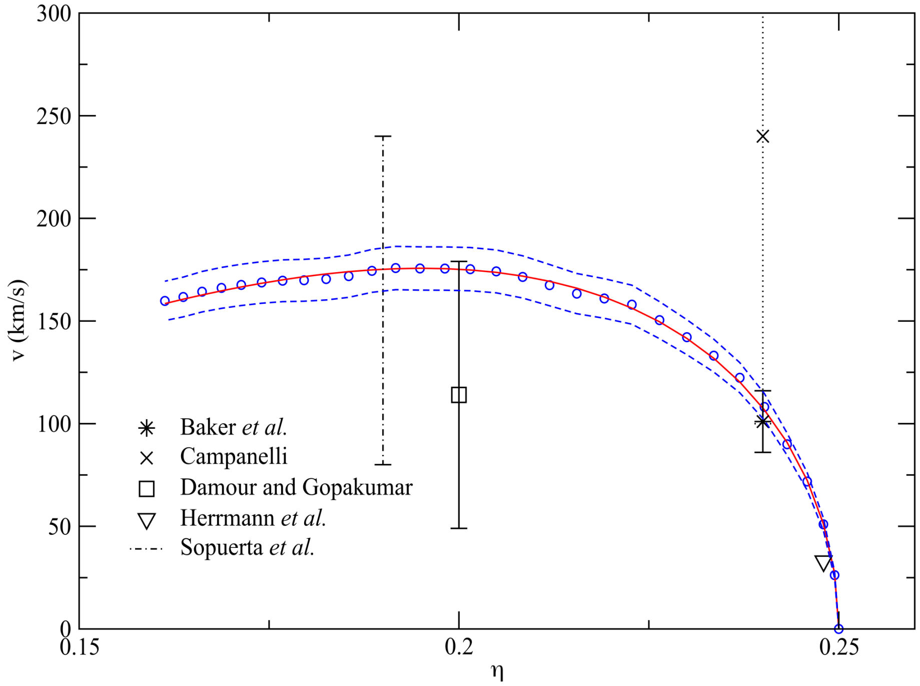

Figure 1.12: Recoil velocity as a function of mass ratio $\eta = q(1+q)^2$ in the non-spinning case. Numerical results from Baker et al. (2006), Campanelli (2005) and Herrmann et al. (2007), and analytic results from Damour & Gopakumar (2006) and Sopuerta et al. (2006) are given for comparison. Figure from Gonzalez et al. (2007).

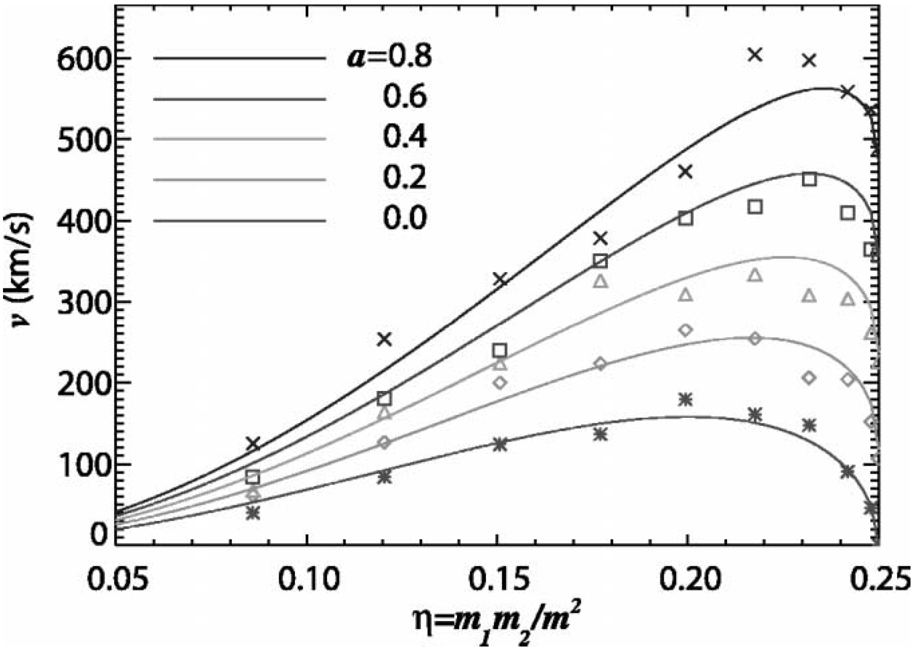

Figure 1.13: Recoil velocity as a function of η for various spin magnitudes a and spins aligned and anti-aligned with the orbital angular momentum. From Schnittman & Buonanno (2007).

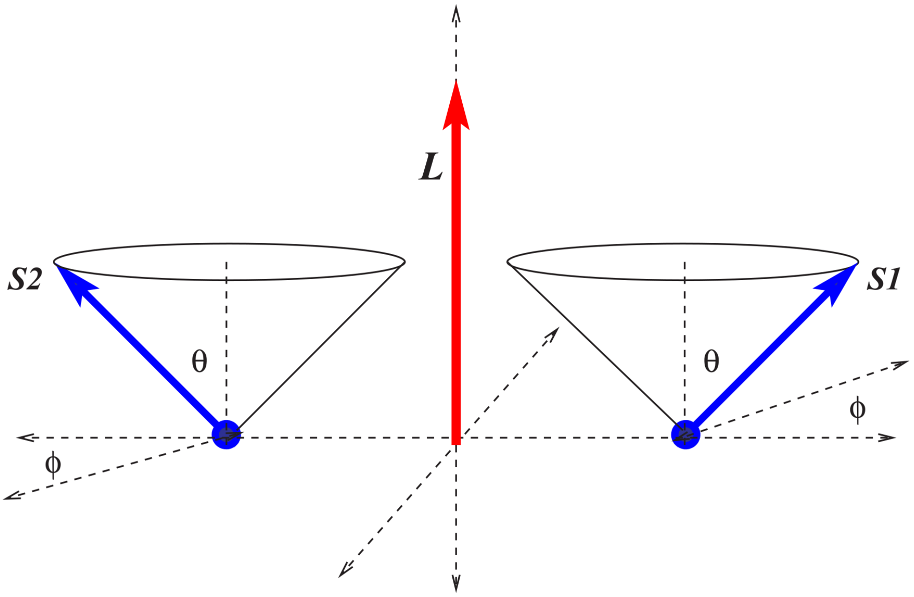

Figure 1.14: The spin configuration for maximum recoil velocity. The components in the orbital plane are equal magnitude but opposite sign, and the components perpendicular to the orbital plane are equal in both magnitude and sign. From Lousto & Zlochower (2011).

damped by dynamical friction, mostly during passages through the centre, until thermal equilibrium is reached. This process could result in a mass deficit in the core of up to five times the mass of the SMBH.

Recently, Nasim et al. (2021) showed in merger simulations that GW recoil in addition to scouring was required to form the 2.71 kpc core in A2261-BCG. Binary scouring alone produced a core size of ~ 1 kpc, but a GW kick of $\sim 0.8\,v_{\rm esc}$ was necessary to reach the observed size. In addition, they found that a mild cusp was retained after scouring, but GW recoil resulted in a flat profile.

1.7 Thesis Outline

In this thesis, the processes which may be involved in producing the observed central light profiles of giant elliptical galaxies are investigated and quantified. These processes provide insight on the likely history of these galaxies and the hierarchical model of galaxy formation, and have implications for GW astronomy and BH spin.

Chapter 2 discusses gravitational stellar systems, the construction of equilibrium models of galaxies, and N-body simulations.

The next two chapters examine the effects of binary scouring and GW recoil after major mergers to form giant elliptical galaxies, using N-body simulations based on the observed parameters of galaxies with some of the largest known cores.

In Chapter 3, the effect of high-velocity kicks is examined to determine if an additional mechanism to binary scouring is required to form the observed sizes of cores in a selection of galaxies, and if there are any unique signatures of GW recoil.

In Chapter 4, the effect of low-velocity kicks is examined and a new mechanism for the formation of extra light or nuclear star clusters in galactic nuclei is proposed.

Chapter 5 is a preliminary assessment of whether the results from Chapters 3 and 4 can be used to predict whether other galaxies are likely to have experienced a GW recoil kick, based on their observed parameters. To do so, the surface brightness profiles of galaxies previously found to have large cores are refitted to obtain a consistent set of data. The relations between SMBH mass, core size and flatness are examined.

Finally, Chapter 6 brings this thesis to a conclusion, and describes key findings and potential future work.

Chapter 2

Galaxy modelling and N-body codes

In this chapter, I discuss the numerical modelling of gravitational systems and their evolution, with an emphasis on giant elliptical galaxies. In 2.1, I begin by considering which forces should be modelled in simulations, before concentrating on gravity, introducing the concept of relaxation time, and categorisation of systems as collisional or collisionless. I go on to explain how 'N-body' systems can be described by distribution functions, and how they can be used to create equilibrium models of stable systems. Then, in 2.2, I review methods for force calculation. I explain that direct summation is accurate but costly, and has a divergence at close separations, which must be avoided using softening or regularisation. I then discuss algorithms which approximate the forces by grouping particles together, in particular the GRIFFIN code, which is used for the simulations in this thesis. In 2.3, I describe how the trajectories of particles can be calculated by time integration, the different methods used, with their advantages and drawbacks. Finally, I discuss variable timesteps, used in almost all contemporary simulations.

2.1 Modelling giant elliptical galaxies

Large galaxies are far too complex to computationally model in their entirety. The required computational resources to do this, in an acceptable timescale, would greatly exceed those available from current technology. Therefore, in each set of circumstances, choices must be made to capture the relevant physics whilst avoiding unnecessary complications, in order to answer the questions being investigated for the lowest computational cost.

In astrophysical systems, gravity must be always be modelled. Gravity is by far the weakest fundamental force but is unique in having only one type of charge (mass). Hence, it dominates at large distances, whereas the charges of the other forces become shielded. However, other physics is required in certain situations. For example, in systems with high gas or plasma content, such as some galaxies and accretion discs and stellar interiors, hydrodynamics is used to model their fluid behaviour (Springel, 2010). Where there are strong magnetic fields, such as in solar flares or jets from BHs, magnetohydrodynamics is important for accurate modelling (Davidson, 2017). Giant elliptical galaxies have low cold gas content (Wiklind et al., 1995). Hence, their current star formation rate is low, and they contain predominantly old stars, likely to have formed between $z \sim$ 3-6 (Thomas et al., 2005). Their gas was probably consumed, after previous mergers, in a burst of star formation (Georgakakis et al., 2001). Such gas-poor systems can be modelled using gravity alone.

Astrophysical systems are 'self-gravitating': their formation and evolution are determined by the mutual gravitational attraction of their components. In any such system, close encounters will transfer kinetic energy between bodies, so that the system tends towards equipartition of kinetic energy over time. If this process, known as 'relaxation', is important over the time the system is being modelled, the system is called 'collisional'. Otherwise, it is a 'collisionless' system.

To determine which regime is appropriate, the cumulative effect of multiple short-range encounters on the velocity of a typical star in a stellar system can be quantified by the 'two-body relaxation time', which estimates the timescale for the velocity to change significantly due to these interactions.

In a close encounter between two bodies, the closest separation between them is defined the 'impact parameter' b. In a self-gravitating system of size R, with typical particle mass m and velocity v, its minimum value is normally taken to be $b_{\mathrm{min}} = 2Gm/v^2$, the value that would lead to a 90° deflection after the encounter, and its maximum value is $b_{\mathrm{max}} = R$. These in turn define the 'Coulomb logarithm' $\Lambda = \log\left(b_{\mathrm{max}}/b_{\mathrm{min}}\right)$. The number of crossings for the v to change by the order of itself is given by (Binney & Tremaine, 2011):

$$n_{\mathrm{relax}} \approx \frac{N}{8\log\Lambda} \,. \tag{2.1}$$

The time taken for a particle to cross the system is $t_{\mathrm{cross}} = R/v$. Finally, the relaxation time is:

$$t_{\mathrm{relax}} = n_{\mathrm{relax}}\, t_{\mathrm{cross}} \,. \tag{2.2}$$

On timescales $\lesssim t_{\mathrm{relax}}$ the dynamics of the system is collisionless. Hence, if t_{relax} is much greater than the time being modelled, two-body encounters are unimportant over the timescale of the simulation and a collisionless simulation is appropriate. Binney & Tremaine (2011) show that Λ is approximately the total particle number N. Thus, substituting Equation 2.1 into Equation 2.2 gives:

$$t_{\mathrm{relax}} \approx \frac{N \cdot t_{\mathrm{cross}}}{8\log N} \,. \tag{2.3}$$

The largest elliptical galaxies have effective radii R_e, within which half their light emanates, of tens to hundreds of kpc. With a typical central velocity dispersion σ of hundreds of km s^{-1}, this gives t_{cross} of ~ 0.3 Gyr. Their total stellar masses $M_* \sim 10^{12} M_\odot$ and the typical stellar mass is $\approx 0.5\, M_\odot$, giving $N \sim 10^{12}$. This gives $t_{\mathrm{relax}} \sim 10^{18}$ years for the centre of the galaxy. This is $\sim 10^8$ times the Hubble time (t_H). Clearly, giant elliptical galaxies are collisionless systems.

Of greater interest for the nucleus is whether the collisionless regime remains appropriate within the radius of influence of the SMBH (Peebles, 1972):

$$r_{\mathrm{i}} = \frac{GM_\bullet}{\sigma^2} \,, \tag{2.4}$$

where its potential dominates that of the rest of the galaxy. The r_{i} for a giant elliptical galaxy with $M_\bullet \sim 10^{10}\mathrm{M}_\odot$ is $\sim 0.5\,$kpc. This gives $t_{\mathrm{cross}} \sim 1$ Myr, and $t_{\mathrm{relax}} \sim 100$ Gyrs, still around 10 times t_H.

In a gravitational system, the force on each particle is clearly the sum of the forces between it and all others in the system, but in a collisionless system, close encounters are unimportant and the rest of the system can be well approximated by a smooth density distribution. In a numerical simulation, particles are still required to calculate forces, but they no longer need represent actual stars or DM particles. Instead, they may represent the smooth density distribution. This is extremely useful, as it allows a system with many stars ($\sim 10^{12}$ for a giant elliptical galaxy) to be represented by much fewer particles ($\sim 10^6 - 10^7$ for a typical simulation), but still capture the gravitational interactions accurately.

Such an ('N-body') system of N particles can be completely specified by its distribution function (f). This is a function of the six-dimensional phase space of positions ($\boldsymbol{x}$) and velocities ($\boldsymbol{v}$). Its evolution is governed by the collisionless Boltzman equation (CBE):

$$\frac{df}{dt} = \frac{\partial f}{\partial t} + \boldsymbol{v} \cdot \frac{\partial f}{\partial \boldsymbol{x}} - \frac{\partial \Phi}{\partial \boldsymbol{x}} \cdot \frac{\partial f}{\partial \boldsymbol{v}} \, . \tag{2.5}$$

To model a stable collisionless system like an isolated elliptical galaxy, the particles must be in equilibrium, with $df/dt = 0$. This avoids violent relaxation: rapid redistribution of energy and energy, which is unwanted and unphysical in a quiescent system.

There are several methods to obtain a suitable f, two of which will be described here. Jeans's theorem (Jeans, 1915) states that "Any steady-state solution of the CBE depends on the phase-space coordinates only through integrals of motion in the given potential, and any function of the integrals yields a steady-state solution of the CBE." An integral of motion I is a function of phase space that remains constant throughout an orbit, for example energy and angular momentum. This can be used to choose an f based on actions (Vasiliev, 2019). Alternatively, a density profile and potential can be used to determine the f which produces them by an inversion technique. The best known is that of Eddington (1916): for a spherically symmetric, isotropic system, it gives f as a function of relative energy ($\mathcal{E}$):

$$f(\mathcal{E}) = \frac{1}{\sqrt{8}\pi^2} \frac{d}{d\mathcal{E}} \int_0^{\mathcal{E}} \frac{d\rho}{d\Psi} \frac{d\Psi}{\sqrt{\mathcal{E} - \Psi}} \, , \tag{2.6}$$

where ρ is the density, and Φ the potential, but more general forms also exist (e.g. de Zeeuw, 1985).

Once f has been determined, it can be sampled to produce the equilibrium model.

2.2 N-body codes

Having obtained the initial conditions for a simulation, the system needs to be evolved in time, accurately modelling the relevant physics. For an N-body system, this means modelling the effect of gravitational interactions between the particles. Determining the trajectory of the bodies is known as the 'N-body problem'. Perhaps surprisingly, given the simplicity of Newtons law of universal gravitation, the problem has an analytic solution only for $N = 2$ and a few special cases of $N = 3$ (Euler, 1767; Lagrange, 1772). Otherwise, for $N \geq 3$, numerical methods are required.

2.2.1 Direct summation

The simplest method of calculating the force on each particle i by 'brute force' direct summation of the forces due to each of the other particles j:

$$\boldsymbol{F}_i = -G m_i \sum_{j \neq i} m_j \frac{\boldsymbol{x}_i - \boldsymbol{x}_j}{\mid \boldsymbol{x}_i - \boldsymbol{x}_j \mid^3} \, . \tag{2.7}$$

$N-1$ calculations are required for each particle, so for N particles this requires $N(N-1) = \mathcal{O}(N^2)$ calculations at each timestep.

Although this is an exact calculation of the force, there are two main drawbacks to direct summation. Firstly, there is clearly a divergence as particle separation approaches zero. This is especially a problem for collisionless simulations, where the particles represent the mass distribution rather than actual objects. Secondly, the $\mathcal{O}(N^2)$ scaling quickly becomes computationally expensive for increasing N.

There are two main ways to avoid the divergence: (i) softening; and (ii) regularisation.

Softening modifies the force calculation at small separations. A commonly used method is Plummer softening (Aarseth & Hoyle, 1963), which uses the potential of a Plummer sphere (Plummer, 1911), with the scale radius replaced by a softening parameter ϵ:

$$\Phi(r) = -\frac{Gm}{\sqrt{r^2+\varepsilon^2}} \,. \tag{2.8}$$

This tends to the normal Newtonian potential for large r, but to a fixed potential as $r \to 0$. ϵ must be carefully chosen for each simulation, to ensure that the gravitational interactions being modelled are not softened, but unphysical interactions are removed. The value of $b_{\rm min}$, using the particle mass and velocity dispersion, provides a useful minimum softening value to avoid large deflections. Adaptive softening can also be used: for example keeping $\epsilon_i \rho_i$ constant results in smaller softening in higher density areas (Saitoh & Makino, 2012).

Regularisation uses a change of co-ordinates to avoid the singularity. The forces can be accurately calculated in the new co-ordinate system, even for small separations, before being transformed back to the original co-ordinate system. The Kustaanheimo-Stiefel (K-S) transformation (Kustaanheimo et al., 1965) is commonly used, which tranforms the two-body problem to a four-dimensional harmonic oscillator. This both removes the singularity and allows easy calculation of forces. The K-S transformation can be generalised to work with higher N (Aarseth & Zare, 1974; Heggie, 1974), but each additional particle adds another singularity so that N coupled transformations are required. For large N, chain regularisation (Mikkola & Aarseth, 1989), which uses regularisation at short distances only, is a better alternative.

To reduce the scaling of the calculations with N, various methods have been introduced, the most important of which are described below.

2.2.2 Grouping particles

Direct summation can be approximated by grouping particles to reduce the number of force calculations. Barnes & Hut (1986) presented a 'tree code' algorithm which divides the simulation volume into a hierarchical system of cubic cells. Whenever more than one particle is present in a cell, it is subdivided into eight subcells, each with half the length of the parent cell, forming an 'oct-tree'. The total mass and centre of mass of each cell is calculated at all levels in the hierarchy. Then the force on each particle p is calculated only for the largest cells where $l/d < \theta$, where l is the length of the cell, d is the distance from the centre of mass of the cell to p, and θ is an accuracy parameter ~ 1. This allows calculation of forces between p and individual particles at short distances, but increasingly combines the particles at longer distances, where their exact location becomes less important. The number of steps to divide the tree into $\sim N$ leaves is the tree depth D, given by $8^D \approx N$. Hence, D scales as $\mathcal{O}(\log N)$, and the number of calculations for N particles is much reduced (Figure 2.1 at $\mathcal{O}(N \log N)$.

The tree code equates to a multipole expansion of the 'source' potential due to the

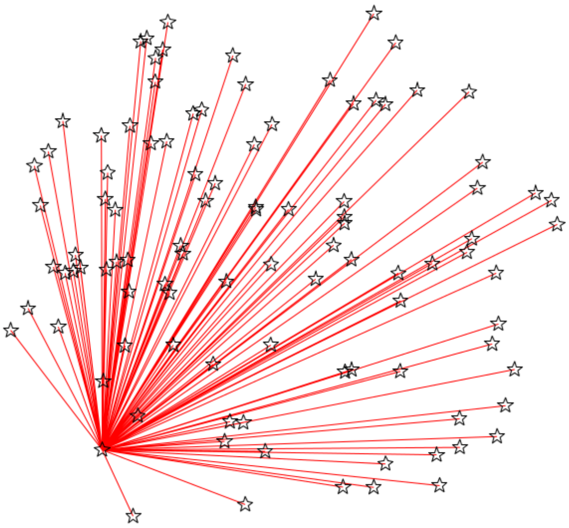

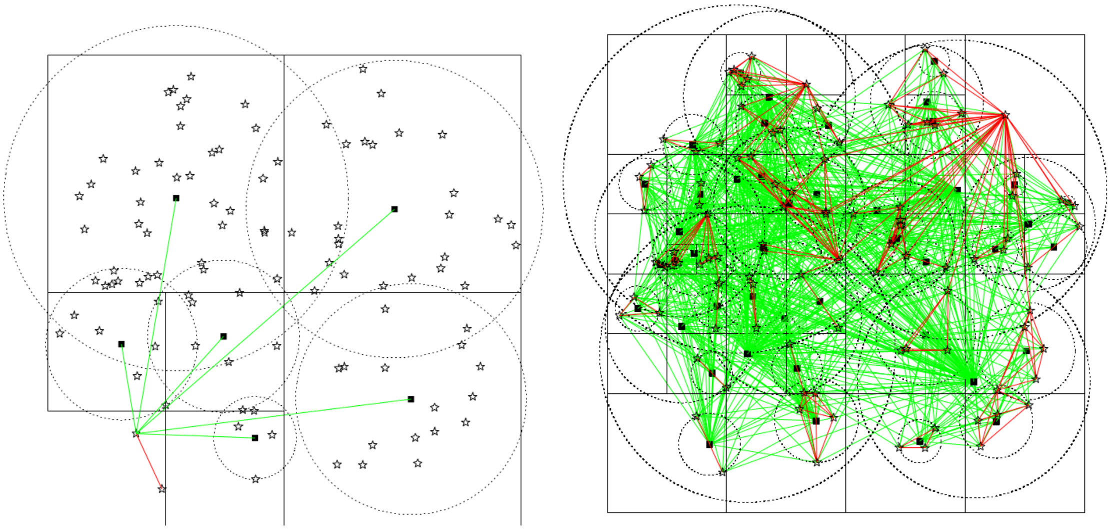

Figure 2.1: A diagrammatic comparison of the calculation algorithms for force calculations using direct summation and tree code. Direct summation (top) calculates the force on each particle as the sum if individual contributions of each of the other particles. (Tree codes find the force on a particle as sum the contribution of a branching hierarchy of cells (bottom left), so that the total number of calculations is much reduced (bottom right). From Dehnen & Read (2011).

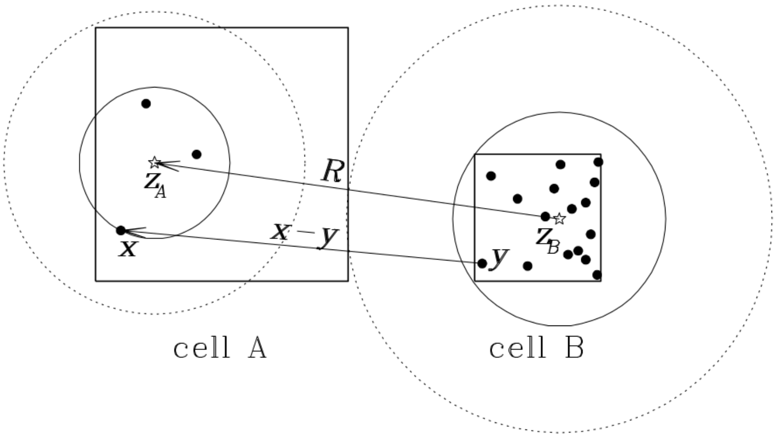

Figure 2.2: Two interacting cells in GRIFFIN. Particles are solid dots and stars indicate the centre of mass of each cell. From Dehnen (2002).

mass distribution in the cells. This concept is extended by the 'Fast Multipole Method' (FMM, Greengard & Rokhlin, 1987; Dehnen, 2000), which also expands the potential for the 'particle side' or 'sink' of the tree algorithm, so that force calculations are cell-cell rather than particle-cell. The symmetry of this algorithm means that the force between each pair of cells need only be calculated once, and so the computational time is greatly reduced, scaling at just $\mathcal{O}(N)$. Dehnen (2014) developed GRIFFIN, an FMM code which is used for the simulations in Chapters 3 and 4, and so will be described in more detail in the next subsection.

2.2.3 GRIFFIN

The original FMM code by Greengard & Rokhlin (1987) is a generic algorithm for modelling the evolution of a system of particles. It can be used in disciplines as varied as plasma physics and molecular dynamics, as well as celestial mechanics, and is a mesh technique with nested grids. Dehnen (2002) combined the cell-cell force calculations of FMM with the branching structure of tree codes, to develop an algorithm for stellar dynamics in particular, and used this in his GRIFFIN code.

In the first step, a hierarchical tree of cubic cells is created and the multipole moment of each cell is calculated. For two interacting cells (Figure 2.2), $\Phi_{B\to A}(\boldsymbol{x})$, the potential at point $\boldsymbol{x}$ in cell A due to sources in cell B is given by the expansion:

$$\Phi_{B\to A}(\mathbf{x}) = -\sum_{m=0}^{p} \frac{1}{m!}(\mathbf{x}-\mathbf{z}_A)^{(m)} \odot \mathbf{C}^{m,p}_{B\to A} + R_p(\Phi_{B\to A})\,, \tag{2.9}$$

where the field tensors $\mathbf{C}^{m,p}_{B\to A}$ are:

$$\mathbf{C}^{m,p}_{B\to A} = \sum_{n=0}^{p-m} \frac{(-1)^n}{n!}\nabla^{(n+m)} g(\mathbf{R}) \odot \mathbf{M}^n_B\,, \tag{2.10}$$

and the multipole moments $\mathbf{M}^n_B$ of cell B are defined as:

Figure 2.3: Comparison of tree code (left) and FMM (right) algorithms. From Dehnen (2014).

$$\mathbf{M}_B^n = \sum_{\mathbf{y}_i \in B} \mu_i (\mathbf{y}_i - \mathbf{z}_B)^{(n)} , \tag{2.11}$$

where $\boldsymbol{z}_A$ and $\boldsymbol{z}_B$ are the centres of cells A and B, μ_i is the mass of the ith particle, $\odot$ is the tensor inner product[1], R_p is the truncation error beyond order p, and $g(\mathbf{R})$ is the Green's function with $\mathbf{R} = \mathbf{z}_A - \mathbf{z}_B$.

For Equation 2.9 to converge, it must meet the multipole acceptance criterion (MAC) $|\boldsymbol{x} - \boldsymbol{y} - \mathbf{R}| < \mathbf{R}$. The algorithm proceeds by a 'dual tree walk', calculating the interaction between pairs of cells according to the MAC. Figure 2.3 shows the differences between this and the single walk of the traditional tree code. In the tree code, the force approximation between cells and each particle uses particle to multipole (P2M), multipole to multipole (M2M) and finally multipole to particle (M2M) kernels. However, FMM uses additional local to local (L2L) and local to particle (L2P) kernels in the 'sink' cells and approximates according to the multipole to local expansion (M2L).

In collisionless simulations, there are two types of errors: estimation error due to the positions of the N bodies sampled from the smooth density distribution being modelled; and approximation error due to the approximate nature of the force calculations. Estimation is reduced by increasing N and optimising the softening. Approximation error can be almost arbitrarily improved, but with a concomitant increase in computational cost. In practice, the best balance between accuracy and use of computational resources is achieved by keeping this error just below the estimation error. GRIFFIN also uses a novel method for estimation errors, and uses them to set the cell sizes and MAC. This achieves comparable force errors to direct summation for $N \gtrsim 10^5$, whilst computational cost scales as just $\sim N^{0.87}$ for relative force errors of $\sim 10^{-7}$.

2.2.4 Grid-based methods

These methods discretise mass onto a grid, solve the differential form of Poisson's equation:

$$\nabla^2 \Phi = 4\pi G \rho , \tag{2.12}$$

and use interpolation to find the forces at the positions of the particles. There are three methods commonly used to distribute the mass. The least accurate is the 'nearest grid point' method, which assigns the whole particle mass to the closest point on the grid. The 'cloud in cell' method linearly divides mass amongst 2^d points, where d is the number of dimensions. The most accurate is the 'triangular shaped cloud', which quadratically interpolates between 3^d points.

---

[1] $\mathbf{P} \odot \mathbf{Q} = \sum_{i_1=1}^{d} \cdots \sum_{i_n=1}^{d} P_{i_1 \ldots i_n} Q_{i_1 \ldots i_n}$

Poisson's equation is often solved using the fast Fourier transform method, which solves the equation in Fourier space:

$$k^2\tilde{\Phi}(\mathbf{k}) = 4\pi G\tilde{\rho}(\mathbf{k}). \tag{2.13}$$

2.3 Time integration

2.3.1 Integration methods

Once the forces have been calculated, the trajectories of the particles can then integrated in time. The simplest scheme is the 'Euler method', which uses a first-order Taylor expansion in position ($\boldsymbol{x}$) and velocity ($\boldsymbol{v}$):

$$\boldsymbol{x}_i = \boldsymbol{x}_{i-1} + \boldsymbol{v}_{i-1}\,\Delta t\,, \tag{2.14}$$

$$\boldsymbol{v}_i = \boldsymbol{v}_{i-1} + \boldsymbol{a}_{i-1}\,\Delta t\,, \tag{2.15}$$

for the ith timestep of length Δt, where $\boldsymbol{a}$ is the acceleration. This has relatively large errors $\propto \Delta t^2$. Therefore, it requires small timesteps, increasing computational cost. It is also not time-symmetric or symplectic[2], so is prone to instability and does not conserve energy.

Much better is the second-order 'Leapfrog' integrator:

$$\boldsymbol{x}_i = \boldsymbol{x}_{i-1} + \boldsymbol{v}_{i-1}\Delta t + \frac{1}{2}\boldsymbol{a}_{i-1}\Delta t^2\,, \tag{2.16}$$

$$\boldsymbol{v}_i = \boldsymbol{v}_{i-1} + \frac{1}{2}(\boldsymbol{a}_{i-1} + \boldsymbol{a}_i)\Delta t\,. \tag{2.17}$$

Despite also requiring only 2 calculations per timestep, it is both time-symmetric and symplectic, and so is much more stable and much better at conserving energy, with smaller errors $\propto \Delta t^3$. Combined with its low computational cost, these characteristics generally make Leapfrog codes suitable for collisionless simulations, but it may be too inaccurate to model the close encounters in collisional simulations. In these cases, the fourth-order 'Hermite' is often used:

$$\boldsymbol{x}_i = \boldsymbol{x}_{i-1} + \boldsymbol{v}_{i-1}\Delta t + \frac{1}{2}\boldsymbol{a}_{i-1}\Delta t^2 + \frac{1}{6}\boldsymbol{j}_{i-1}\Delta t^3 + \frac{1}{24}\boldsymbol{s}_{i-1}\Delta t^4\,, \tag{2.18}$$

$$\boldsymbol{v}_i = \boldsymbol{v}_{i-1} + \boldsymbol{a}_{i-1}\Delta t + \frac{1}{2}\boldsymbol{j}_{i-1}\Delta t^2 + \frac{1}{6}\boldsymbol{s}_{i-1}\Delta t^3 + \frac{1}{24}\boldsymbol{c}_{i-1}\Delta t^4\,, \tag{2.19}$$

$$\boldsymbol{a}_i = \boldsymbol{a}_{i-1} + \boldsymbol{j}_{i-1}\Delta t + \frac{1}{2}\boldsymbol{s}_{i-1}\Delta t^2 + \frac{1}{6}\boldsymbol{c}_{i-1}\Delta t^3\,, \tag{2.20}$$

$$\boldsymbol{j}_i = \boldsymbol{j}_{i-1} + \boldsymbol{s}_{i-1}\Delta t + \frac{1}{2}\boldsymbol{c}_{i-1}\Delta t^2\,. \tag{2.21}$$

which also uses jerk $\boldsymbol{j} = \dot{\boldsymbol{a}}$, snap $\boldsymbol{s} = \ddot{\boldsymbol{a}}$, and crackle $\boldsymbol{c} = \dddot{\boldsymbol{a}}$. To calculate all these derivatives would be computationally expensive. Thankfully, $\boldsymbol{s}$ and $\boldsymbol{c}$ can be eliminated to give:

$$\boldsymbol{x}_i = \boldsymbol{x}_{i-1} + \frac{1}{2}(\boldsymbol{v}_i + \boldsymbol{v}_{i-1})\Delta t + \frac{1}{12}(\boldsymbol{a}_{i-1} - \boldsymbol{a}_i)\Delta t^2 + \mathcal{O}(\Delta t^5)\,, \tag{2.22}$$

$$\boldsymbol{v}_i = \boldsymbol{v}_{i-1} + \frac{1}{2}(\boldsymbol{a}_i + \boldsymbol{a}_{i-1})\Delta t + \frac{1}{12}(\boldsymbol{j}_{i-1} - \boldsymbol{j}_i)\Delta t^2 + \mathcal{O}(\Delta t^5)\,, \tag{2.23}$$

---

[2] A symplectic integrator preserves the symplectic form of a Hamiltonian system.

but this is now an implicit scheme. This can be resolved by predicting the position and velocity using:

$$\boldsymbol{x}_p = \boldsymbol{x}_{i-1} + \boldsymbol{v}_{i-1}\Delta t + \frac{1}{2}\boldsymbol{a}_{i-1}\Delta t^2 + \frac{1}{6}\boldsymbol{j}_{i-1}\Delta t^3 \,, \tag{2.24}$$

$$\boldsymbol{v}_p = \boldsymbol{v}_{i-1} + \boldsymbol{a}_{i-1}\Delta t + \frac{1}{2}\boldsymbol{j}_{i-1}\Delta t^2 \,, \tag{2.25}$$

then computing the $\boldsymbol{a}$ and $\boldsymbol{j}$ of particle k using:

$$\boldsymbol{a}_k = G\sum_{l\neq k} m_l \frac{\boldsymbol{x}_{lk}}{|\boldsymbol{x}_{kl}|^3} \,, \tag{2.26}$$

$$\boldsymbol{j}_k = -G\sum_{l\neq k} m_l \left[\frac{\boldsymbol{v}_{lk}}{|\boldsymbol{x}_{lk}|^3} - 3\frac{(\boldsymbol{x}_{lk}\cdot\boldsymbol{v}_{lk})\boldsymbol{x}_{lk}}{|\boldsymbol{x}_{lk}|^5}\right] . \tag{2.27}$$

where for a vector $\boldsymbol{z}$, we define $\boldsymbol{z}_{cd} \equiv \boldsymbol{z}_c - \boldsymbol{z}_d$, and finally calculating corrected values for $\boldsymbol{x}_i$ and $\boldsymbol{v}_i$ using Equations 2.22 and 2.23. However, despite its high accuracy, with errors $\propto \Delta t^5$, the Hermite algorithm is not symplectic, so it is not suitable where long-term energy conservation is important.

2.3.2 Variable timesteps

Although the above schemes have different levels of accuracy, they all have errors based on the timestep Δt. Reducing Δt reduces error but increases computational cost, so the choice of timestep must balance these two competing factors. In practice, simulations use variable timesteps, reducing Δt when particles are closer together and more accuracy is required. Typically, the 'block-step' scheme is used (Figure 2.4, Makino, 1991), which assigns timesteps to particles using a hierarchy of factors of 2 in relation to a 'base step' Δt_b, so that:

$$\Delta t_i = \frac{\Delta t_b}{2^i} \tag{2.28}$$

for the ith level in the hierarchy. The allocation is fluid, so that particles can move between levels whenever their timesteps are aligned. The use of factors of 2 between levels maximises this flexibility.

GRIFFIN allocates individual timesteps to particles and uses the block-step scheme. However, the timestep threshold below which a particle is regarded as 'active' is altered for each force calculation, such that accuracy is maintained whilst only considering interactions between cells with at least one active particle (Dehnen, 2014).

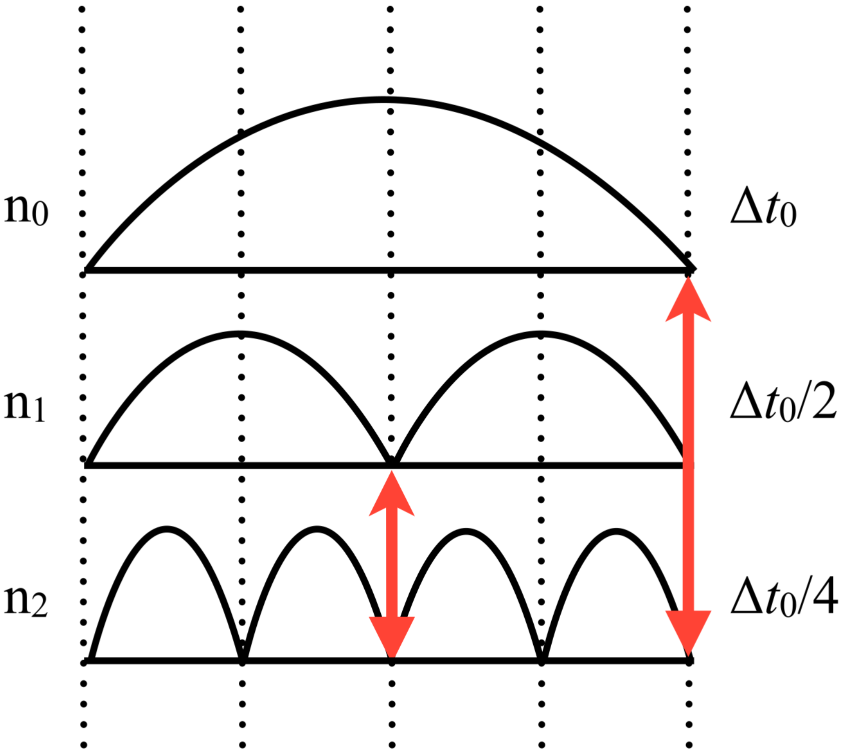

Figure 2.4: The ‘block-step’ timing scheme uses levels n_i, where i is the level in the hierarchy, with timesteps differing by a factor of 2 between neighbouring levels. Particle can move between levels where they are synchronised (red arrows). From Dehnen & Read (2011).

Chapter 3

Core formation by binary scouring and gravitational wave recoil in massive elliptical galaxies

In this chapter, I examine core formation in giant elliptical galaxies. In particular, I model equal mass dry mergers of elliptical galaxies, binary scouring by SMBHs, and GW recoil after merger of the SMBHs. I confirm that an additional mechanism, such as GW recoil, is necessary to form the largest observed cores. I also find that a unique signature of recoil is a flat 3D density profile. The work for this chapter has been published in The Astrophysical Journal, Volume 974, Issue 4, 2024 October 20, Pages 204-219: Nader Khonji, Alessia Gualandris, Justin I. Read, and Walter Dehnen.

Abstract

Scouring by supermassive black hole (SMBH) binaries is the most accepted mechanism for the formation of the cores seen in giant elliptical galaxies. However, an additional mechanism is required to explain the largest observed cores. Gravitational wave (GW) recoil is expected to trigger further growth of the core, as subsequent heating from dynamical friction of the merged SMBH removes stars from the central regions. We model core formation in massive elliptical galaxies from both binary scouring and heating by GW recoil and examine their unique signatures. We aim to determine if the nature of cores in 3D space density can be attributed uniquely to either process and if the magnitude of the kick can be inferred. We perform N-body simulations of galactic mergers of multi-component galaxies, based on the observed parameters of four massive elliptical galaxies with cores $> 0.5\,\mathrm{kpc}$. After binary scouring and hardening, the merged SMBH remnant is given a range of GW recoil kicks with 0.5-0.9 of the escape speed of the galaxy. We find that binary scouring alone can form the cores of NGC 1600 and A2147-BCG, which are $< 1.3\,\mathrm{kpc}$ in size. However, the $> 2\,\mathrm{kpc}$ cores in NGC 6166 and A2261-BCG require heating from GW recoil kicks of < 0.5 of the galaxy escape speed. A unique feature of GW recoil heating is flatter cores in surface brightness, corresponding to truly flat cores in 3D space density. It also preferentially removes stars on low angular momentum orbits from the galactic nucleus.

3.1 Introduction

The detection of gravitational waves (GWs) from the merger of a stellar mass black hole binary in 2015 (Abbott et al., 2016) heralded a paradigm shift in observational astronomy. Considerable resources are now focused on the detection of lower frequency GWs from supermassive black hole (SMBH) binaries. SMBHs are likely to reside at the centres of all massive galactic nuclei, with evidence for this ranging from dynamical studies of maser emission (e.g. Miyoshi et al., 1995; Kuo et al., 2010), to the dynamics of AGN accretion discs (Macchetto et al., 1997), to the direct observation by the Event Horizon Telescope collaboration (Event Horizon Telescope Collaboration et al., 2019, 2022).

Cold dark matter (DM) cosmologies such as ΛCDM predict the hierarchical growth of structure by formation and then mergers of DM halos and galaxies (Blumenthal et al., 1984). Given the presence of SMBHs, such mergers will inevitably lead to the formation of SMBH binaries (BHBs) (Begelman et al., 1980). If BHBs form and evolve due to interactions with the background stellar population, they will become strong sources of nanohertz GWs, which are detectable using pulsar timing arrays (PTAs; Foster III e.g. 1990, Sesana et al. 2018). Recently, the European PTA with the Indian PTA (Antoniadis et al., 2023), the North American Nanohertz Observatory for GWs (NANOgrav) (Agazie et al., 2023), the Chinese PTA (Xu et al., 2023) and the Parkes PTA (Reardon et al., 2023), released analysis of their latest datasets showing exciting evidence for a stochastic nanohertz GW background (GWB). The background signal is consistent with that of a population of BHBs evolving due to GW inspiral in a stellar/gaseous environment (Antoniadis et al., 2023).

Elliptical galaxies contain more than half the total stellar mass of the Universe (Bell et al., 2003; Read & Trentham, 2005). The most massive are found in the centres of galaxy clusters and host the most massive SMBHs. Their inner surface brightness profiles show a range of behaviours, with some rising as steep "cusps" and others asymptoting towards flat inner "cores" (Ferrarese et al., 1994; Lauer et al., 1995). The cored ellipticals are systematically brighter ($M_{\rm VT} < -21$) and tend to be anisotropic in velocity, with box-shaped isophotes and low rotation. By contrast, the cusped ellipticals are fainter ($M_{\rm VT} > -21$), isotropic in velocity, with disc-shaped isophotes and higher rotation (Kormendy & Bender, 1996; Kormendy et al., 2009). Although this was initially thought to be a dichotomy, there is now known to be some overlap between the two types (Rest et al., 2001). Most cores are relatively small, from tens to a few hundred parsecs in size (Byun et al., 1996; Dullo & Graham, 2014; Rusli et al., 2013), but a few are greater than 0.5 kpc (Dullo, 2019).

It had long been postulated that elliptical galaxies are formed by mergers (Holmberg, 1941; Toomre & Toomre, 1972). However, initial simulations (without SMBHs) could not replicate the larger cores seen in the most massive galaxies (Farouki et al., 1983). Indeed, Dehnen (2005) showed that the steepest cusp is retained in mergers of such systems. The likely solution arose from the theory that active galactic nuclei (AGNs) were the result of accretion by a massive black hole (Lynden-Bell, 1969; Begelman & Rees, 1978). Begelman et al. (1980) were the first to argue that mergers would lead to BHBs in AGNs. With the addition of central black holes to the precursor galaxies in their simulations, Ebisuzaki et al. (1991) found an increase in core size of the remnant.

Observational evidence indicates that quiescent elliptical galaxies were already formed at $z \sim 2$, but were much more compact than at $z = 0$, with a typical size ~ 1 kpc (Van Dokkum et al., 2008). Hence, their current size is likely due to major (Naab et al., 2006) and/or minor (Naab et al., 2009) dry mergers.

In summary, there is a high probability that giant elliptical galaxies are the end product of mergers of galaxies containing SMBHs. Begelman et al. (1980) first described the likely processes in such mergers which, for gas-poor mergers, can be divided into three stages: (i) dynamical friction against the stellar population and dark matter, which brings the galaxies and SMBHs together, leading to the formation of a BHB; (ii) three-body interactions between stars/dark matter and the binary, often resulting in stellar ejections; and (iii) GW inspiral and coalescence of the binary, with the potential for GW recoil that can push the merged BHB out of the centre of the galaxy and, in extreme cases, even unbind it.

Dynamical friction (Chandrasekhar, 1943) is dominated by long range (kiloparsec-scale) encounters between each SMBH and the surrounding matter. As a SMBH moves through a field of stars and dark matter, they are pulled to form a 'gravitational wake' behind it, slowing the SMBH with the transfer of energy and angular momentum. In a major merger, this causes the SMBHs to sink into the potential well of the remnant (Antonini & Merritt, 2011). Eventually, they become gravitationally bound and form a binary (Valtaoja et al., 1989). From around this time, there is rapid hardening of the binary as dynamical friction wanes and short range (parsec-scale) three-body interactions between the SMBH binary and stars on low angular momentum orbits dominate (Quinlan, 1996; Sesana et al., 2006). Simulations of a binary system with low mass intruders show that the vast majority of intruders undergo slingshot ejection from the system, with a concomitant increase in binding energy of the binary (Hills, 1983). Since this process leads to a central mass deficit (Merritt, 2006) and reduced central density, it is known as 'binary scouring'. It is the most established mechanism for core formation and has been shown to occur in simulations (e.g. Quinlan & Hernquist, 1997; Milosavljević & Merritt, 2001; Gualandris & Merritt, 2012) and has been shown to preferentially remove stars on low angular momentum orbits (Thomas et al., 2014).

Low angular momentum stars and gas populate a region in phase space known as the 'loss-cone'. In order for binary hardening to continue past the initial rapid phase and until GW emission becomes significant, the loss-cone must be continually replenished. For an idealised spherically symmetric galaxy, this can only occur by collisional two-body relaxation, a process typically occurring on timescales longer than a Hubble time (Makino & Funato, 2004; Berczik et al., 2005). This has led to the 'final parsec problem', an envisioned stalling of the hardening of the binary at roughly parsec-scale separations due to the lack of loss-cone refilling in spherical galaxies. However, simulations of galactic mergers from early times show that collisionless loss-cone refilling due to torques and angular momentum diffusion in non-spherical systems lead to efficient hardening of the binary to the GW phase (Khan et al., 2011; Gualandris & Merritt, 2011; Vasiliev et al., 2014). All merger remnants are somewhat triaxial (Bortolas et al., 2018a), and even a modest triaxiality (e.g. axis ratios 1:0.9:0.8) is sufficient for collisionless loss-cone refilling and coalescence within a Hubble time (Vasiliev et al., 2015; Gualandris et al., 2017).

GWs also provide an alternative method for core formation. Asymmetric emission of linear momentum leads to a 'recoil kick' on the newly formed SMBH merger remnant. In the non-spinning case, the kick velocity depends solely on the mass ratio:

$$q = \frac{m_2}{m_1} \leq 1\,, \tag{3.1}$$

where m_1 and m_2 are the larger and smaller SMBH masses respectively. Numerical simulations by Gonzalez et al. (2007) showed the maximum recoil kick in these circumstances is relatively slow at $\sim 175\,\mathrm{km\ s^{-1}}$ for $q \approx 0.36$. However, in the spinning case, the recoil depends on both q and the configuration of the spins. Campanelli et al. (2007b) found the combination of $q = 1$ and spins aligned and anti-aligned with the orbital plane gives a maximum recoil velocity of $\sim 4000\,\mathrm{km\ s^{-1}}$. In the most extreme cases, where the components of the spin in the orbital plane are of equal magnitude but opposite in sign, and the components out of the plane are equal in magnitude and sign, they can reach $5000\,\mathrm{km\ s^{-1}}$ (Lousto & Zlochower, 2011), clearly exceeding the escape speed for the galaxy.

It is expected that in most cases kicks will be modest and the newly formed SMBH and core will oscillate back and forth about their common centre of mass. The oscillations are gradually damped as energy is transferred to the stars and dark matter, mostly during passages through the centre, until thermal equilibrium is reached. These interactions result in displacement or even ejection of stars, similar to that in binary scouring, enlarging any pre-existing core formed by the binary and potentially leading to very large cores (Gualandris & Merritt, 2008).

Stalling is another potential mechanism for enlargement of a core (Goerdt et al., 2010). Read et al. (2006) show that dynamical friction would fail at the edge of a constant density core, leading to stalling of an infalling object such as a SMBH. This implies that if a galaxy with a flat core undergoes a further merger, the infalling SMBH may stall and not achieve coalescence. Such 'stalled perturbers' could be responsible for the 'knots' seen in A2261-BCG (Bonfini & Graham, 2016; Nasim et al., 2021). Subsequent infalls into a galaxy with a stalled SMBH could also lead to multiple SMBH systems (Lousto & Zlochower, 2008; Liu et al., 2011; Kulkarni & Loeb, 2012), with the potential for slingshot ejection of a SMBH (Iwasawa et al., 2006). Hence, the size and flatness of a core has important implications. Even if the core is not completely flat, the time for the binary to proceed to coalescence could be significantly increased. This is likely to affect the SMBH GWB signal which PTAs are endeavouring to measure (Sesana, 2013a; Ravi et al., 2014; Sampson et al., 2015).

For the reasons given above, it is important to be able to accurately determine core size and flatness of the central density profile. This can be achieved by fitting observed luminosity profiles to an appropriate model. There are two models in common use. The Nuker profile (Lauer et al., 1995) uses inner and outer logarithmic slopes separated at the break radius (r_b), which is taken as the size of the core. The inner logarithmic slope (γ) indicates the flatness of the core. The Nuker profile was designed to fit the central part of the light profile. Graham et al. (2003) showed that the Nuker parameters are dependent on the radial extent of the galaxy used for fitting and may overestimate r_b. They introduced the core-Sérsic profile, which replaces the outer power law with a Sérsic function (Sérsic, 1963).

To a large extent, recent simulations support core formation by binary scouring as the main mechanism to explain observed cores in large elliptical galaxies (Rantala et al., 2018; Frigo et al., 2021; Dosopoulou et al., 2021). However, it remains unclear whether scouring alone can explain core formation in all cases (Nasim et al., 2021). Dullo (2019) published core-Sérsic fits to observations of 12 galaxies with cores larger than 0.5 kpc, with only two of these having a central slope $\gamma > 0.15$. Cores such as these are found in the most massive and luminous elliptical galaxies, usually brightest cluster galaxies (BCGs), which contain the most massive SMBHs. Given the processes described above, galaxies with larger SMBHs might be expected to have larger cores. It is important to test whether binary scouring alone can produce cores of this size and flatness. If not, GW recoil, stalling infallers and multiple SMBH systems are all potential additional mechanisms for the formation of these large, flat cores, as already noted in Nasim et al. (2021).

First discovered by Postman et al. (2012), the largest core in Dullo (2019), and the largest known core to date, is that of A2261-BCG. Using core-Sérsic fitting, they obtain $r_{\mathrm{b}} \sim 3\,\mathrm{kpc}$, with a flat surface brightness profile ($\gamma = 0.0$). Simulations of core formation based on this galaxy were performed by Nasim et al. (2021), finding that a core of 0.5-1 kpc could be explained by binary scouring alone. Although it was previously thought that the mass deficit after multiple mergers is proportional to the number of mergers (Merritt, 2006), i.e. that cores are enlarged by each merger, Nasim et al. (2021) found that there is minimal increase in both core size and mass deficit with subsequent major or minor mergers. It becomes progressively harder to carve a core once one is already present and the central density has been lowered. This implies that an additional mechanism is required to explain the largest observed cores. They explored GW recoil following binary coalescence as the most likely mechanism, and showed that it can be very efficient at enlarging a pre-existing core. Furthermore, Nasim et al. (2021) showed that cores retain shallow cusps after scouring, especially spatial density, even after sequential dry mergers, and GW recoil is required to form truly flat cores.

In this paper we study the physical processes involved in core formation in a range of galaxies, to understand how large cores are formed and what density profiles they produce, i.e. shallow cusps or flat profiles. We test whether binary scouring and GW recoil have unique observational signatures that can predict if GW recoil has occurred in a given galaxy. If recoil is required, the signatures could also provide an indication of the strength of the required kick. To this end, we simulate major mergers with parameters based on four galaxies from Dullo (2019), including A2261-BCG, with a range of core sizes above 0.5 kpc. We investigate whether and how much GW recoil is required to achieve the observed core sizes, and if GW recoil produces fully flat cores in spatial density. We compare our results to observations of a sample of cored galaxies. For the first time, we attempt to explain differences in the phase space density of stars as a result of dynamical friction/stellar hardening and GW recoil by analysing the energy and angular momentum transfer in the two processes. We find that, similarly to Nasim et al. (2021), the two galaxies with cores greater than 2 kpc require GW recoil to achieve their observed size. Furthermore, recoil produces flatter cores than binary scouring alone, and needs to be invoked to explain the observed flatness in the profiles of all the four galaxies. We find that the required GW kicks are modest at less than half the escape velocity of the galaxies. Finally, we show that both binary scouring and recoil preferentially remove low energy stars, but that GW recoil in particular ejects low angular momentum stars from the core. This is why GW recoil produces truly flat, constant density, cores in 3D. Core formation by the stalled perturber and multiple SMBH scenarios are not considered further here, but may be revisited in future work.

This paper is organised as follows. The selection of galaxies, merger and GW recoil simulation methodology and density profile fitting procedure are described in Section 3.2. The formation and evolution of BHBs, core-fitting and study of the energy and angular momentum exchanges are presented in Section 3.3. Finally, discussion and conclusions of the comparison between binary scouring and GW recoil are presented in Section 3.4.

3.2 Methods

We performed equal-mass simulations of galactic mergers to study the formation of large cores in giant elliptical galaxies and to compare the processes of binary scouring and GW recoil. Four galaxies with observed large cores were selected for modelling. These were chosen to have a range of core sizes ($\sim$ 0.5-3 kpc) and SMBH masses, as well as variation in other parameters such as effective radius, Sérsic index and bulge mass (M_*).

Observational data was taken from Dullo (2019), who performed core-Sérsic fits to their surface brightness profiles from both Hubble Space Telescope and ground-based images. SMBH mass estimations were available from their r_b-$M_\bullet$ relation, with the exception of NGC 1600, which has a direct measurement. Dullo (2019) also provided M_* estimations using the M_*-luminosity relation from Worthey (1994). Although there is significant scatter in core-SMBH relations, Dullo (2019) found that the r_b-$M_\bullet$ relation was the most reliable for the most massive galaxies, compared to luminosity and velocity dispersion. The galaxy parameters are summarised in Table 3.1.

Table 3.1: Parameters of the selected galaxies.

Galaxy	Type	r_b [kpc]	γ	α	n	r_e [kpc]	$M_\bullet$ [a] $[10^{10} M_\odot]$	M_* [b] $[10^{12} M_\odot]$
NGC 1600	Isolated	0.65	0.04	2	6.3	22.8	1.70	1.51
A2147-BCG	BCG	1.28	0.14	2	6.4	31.8	2.63	1.34
NGC 6166	BCG	2.11	0.14	2	9.0	83.1	4.79	3.39
A2261-BCG	BCG	2.71	0.00	5	2.1	17.6	6.45	4.07

Notes: First five parameters are from core-Sérsic fits

[a] Black hole masses from the $M_\bullet$-r_b relation except NGC 1600 (directly measured).

[b] Bulge mass from spheroid luminosity.

Multicomponent equilibrium models of precursor galaxies were realised using the AGAMA action-based modelling library (Vasiliev, 2019). Potential models for all three components (SMBH, stellar bulge and DM halo) and density models for the bulge and halo were made. For the stellar bulge, a Sérsic profile (Sérsic, 1963) was used, which can be represented as:

$$I(r) = I(0)\, e^{-b_n (r/r_\mathrm{e})^{1/n}} \; . \tag{3.2}$$

This has three free parameters: the central surface brightness $I(0)$, the effective radius r_e, and the Sérsic index n. Here, b_n is a function of n that ensures r_e is the half-light radius ($b_n \approx 2n - 1/3$). AGAMA uses a deprojected profile in which the bulge mass can be used as a proxy for luminosity.

For the DM halo, we used the Navarro-Frenk-White profile (Navarro et al., 1997):

$$\rho(r) = \frac{\rho_\mathrm{s}}{(r/r_\mathrm{s})\,(1 + r/r_\mathrm{s})^2} \; , \tag{3.3}$$

where ρ_s is the characteristic density and r_s is the scale radius. The latter is defined by r_s=r_{200}/c, where r_{200} is the radius at which the mean enclosed density is 200 times the critical density, and c is the halo concentration. The concentration parameter c is calculated using the concentration-mass relation at redshift $z = 0$ from Dutton & Maccio (2014):

$$\log c = 0.905 - 0.101 \log\left(\frac{M_{200}\, h}{10^{12}\, M_\odot}\right) \; , \tag{3.4}$$

where h has the usual relation to the Hubble constant ($H_0 = 100\, h\,\mathrm{km\ s^{-1}\ Mpc^{-1}}$). M_{200} is the enclosed mass at r_{200} given by:

$$M_{200} = 200\, \rho_\mathrm{crit}\, \frac{4}{3}\pi\, R_{200}^3 \; , \tag{3.5}$$

where ρ_0 is a characteristic density which is dependent only on c and ρ_crit. Clearly, once M_{200} is chosen, all other halo parameters can be calculated.

Spherical distribution functions were created using the potential and density models. These were then sampled to provide ergodic N-body galaxy models.

We simulated the formation of each chosen galaxy by a major merger of two precursor galaxies, identified by the name of the observed galaxy with the suffix 'P', with parameters (Table 3.2), based on the observed values (Table 3.1). The precursor SMBH and stellar bulge masses were assumed to be half that of those of the merger remnant. The value of r_e used for the bulge was half that of the core-Sérsic fit by Dullo (2019), since the virial theorem predicts r_e should double in an equal-mass dissipationless merger (Naab et al., 2009). Since three of the galaxies are BCGs, their halos are indistinct from the neighbouring galaxies in their clusters. Hence M_{200} was estimated at $\sim 10^{14} M_\odot$ using the M_*-M_{200} relation from Correa & Schaye (2020). NGC 1600 is unusual in that it is an isolated galaxy, and hence an observed value $M_{200} = 1.58\text{x}10^{14} M_\odot$ is available (Goulding et al., 2016), of which half was used for the precursors.

Table 3.2: Parameters of precursor galaxies.

Precursor	$M_\bullet$ [$10^{10} M_\odot$]	M_* [$10^{12} M_\odot$]	M_{200} [$10^{14} M_\odot$]	n	r_e [kpc]	N_*	N_DM	N	Res_* [$10^6 M_\odot$]
NGC 1600 P	0.85	0.76	0.79	6.3	11.4	94902	959532	1054434	0.84
A2147-BCG P	1.32	0.67	1.00	6.4	15.9	68065	986478	1054543	1.04
NGC 6166 P	2.40	1.69	1.00	9.0	41.7	153422	901543	1054965	1.17
A2261-BCG P	3.23	2.04	1.00	2.1	8.8	176091	830565	1054436	1.20

The total particle number was $N \sim 10^6$ for each precursor, to optimally balance overall resolution and computational resources. The numbers of bulge and halo particles were then chosen to give a halo-to-bulge particle mass ratio (PMR) of ~10. This was to balance the need for sufficient resolution of the core with that to avoid significant dynamical segregation of the halo particles, which may result from a PMR that is too high. Core resolution was further increased by the use of the 'mass-refinement' scheme of Attard et al. (2024). This works by oversampling the particle distribution by a factor of ten and dividing each particle type into four concentric zones. The inner zone containing 1% of particles is left untouched. The outer zones containing 11.5%, 38.5% and 49% of particles are increased in particle mass by factors of $\sim$ 2.53, 10 and 40 respectively. Then the particle numbers are correspondingly reduced to restore N to its initial value and to ensure that the density profile is unaffected. The technique allows to increase central resolution at the same overall N, and has been shown to reduce stochastic effects in simulations of galactic mergers (Attard et al., 2024). The maximum (central) mass resolution (Res_*) for each galaxy is shown in Table 3.2.

Table 3.3: Orbital parameters at the end of scouring.

Remnant	t_k [Myrs]	a_h [pc]	e
NGC 1600 M	310	23	0.18
A2147-BCG M	385	38	0.09
NGC 6166 M	285	30	0.27
A2261-BCG M	470	30	0.21

For the mergers, denoted by the name of the galaxy being modelled with the suffix 'M', the precursor galaxies were placed on a highly elliptical orbit ($e = 0.95$). This was to replicate the almost radial mergers seen in cosmological simulations (e.g. Khochfar & Burkert, 2006). The initial separation between the two galaxies was set to $d = 80\,\mathrm{kpc}$ to ensure that stellar bulges are still well separated.

All N-body simulations were performed with GRIFFIN (Dehnen, 2014), a fast multipole method N-body code optmised to achieve force errors comparable to direct summation while requiring only $\mathcal{O}(N)$ operations. All interactions were softened with a Plummer-type softening parameter of 3 pc for any interaction involving the SMBHs and 30 pc for all other bulge and halo particle interactions.

The SMBHs were followed through the galactic merger and the phase of dynamical friction to formation of a binary and further hardening by encounters with stars. Once the binary had hardened, the SMBHs were assumed to have merged due to GW emission, and the SMBH remnant was placed at the centre of mass of the binary prior to coalescence. They were then given a 'GW kick', arbitrarily in the x-direction, of 0.5, 0.7 or 0.9 as a proportion of the escape speed v_e from that galaxy. This was calculated numerically as $v_\mathrm{e} = \sqrt{-2\Phi}$, where Φ is the total potential of the bulge and halo. The simulation was then continued until the oscillatory motion of the SMBH remnant had settled to the level of Brownian motion. The 'Brownian velocity' v_B can be determined simply from equipartition of energy and can be written as (Smoluchowski, 1906; Merritt, 2001; Bortolas et al., 2018a)

$$v_\mathrm{B}^2 = \frac{m}{M_\bullet}\sigma_*^2 \,, \tag{3.6}$$

where m is the mass of a stellar particle and σ_* is the stellar velocity dispersion.

3.3 Results

The formation and evolution of the BHB during the mergers is shown in Figure 3.1, with $t = 0$ at the start of the merger simulation. The first phase, dominated by dynamical friction, ends when the separation reaches a_f, the influence radius of each SMBH (or the secondary SMBH in the case of unequal-mass mergers). It is defined as the separation at which the enclosed stellar mass is twice the (secondary) SMBH mass:

$$M_* \left(r < a_\mathrm{f}\right) = 2m_2 \,. \tag{3.7}$$

A2261-BCG M has a significantly larger a_f at 1.85 kpc, compared to 0.58 kpc for NGC 6166 M. This is likely due to the combination of a higher $M_\bullet$ and a flatter inner Sérsic profile in A2261-BCG M.

After this, there is rapid hardening of the binary due to three-body encounters with stars and binary scouring. The specific binding energy exceeds the specific kinetic energy (Milosavljević & Merritt, 2001) at the hard binary separation:

$$a_\mathrm{h} = \frac{GM_\bullet}{4\sigma^2} \,, \tag{3.8}$$

where σ is the stellar velocity dispersion. In the case of an unequal-mass merger, the reduced mass of the binary would be used. The simulations were paused once they had reached this point for the GW kick to be applied. The time at which the SMBH binary was merged (t_k), the value of a_h and the eccentricity (e) of the binary at the time of merger are shown for each remnant in Table 3.3. We note that the circularisation of the binary is consistent with the findings of Fastidio et al. (2024) for mergers with initial high eccentricity.

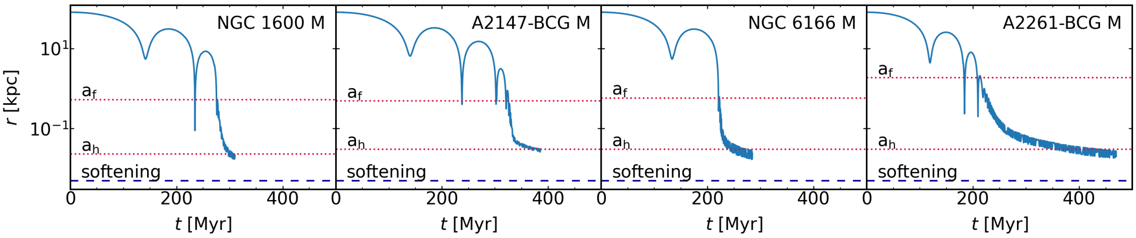

Figure 3.1: Separation between the SMBHs as a function of time in models NGC 1600 M, A2147-BCG M, NGC 6166 M and A2261-BCG M, showing the three characteristic phases of binary evolution. The dotted lines indicate the critical separations corresponding to a_{f}, the influence radius of each SMBH, and a_{h}, the hard binary separation (see Equations 3.7 and 3.8) ; the dashed line indicates the SMBH softening length.

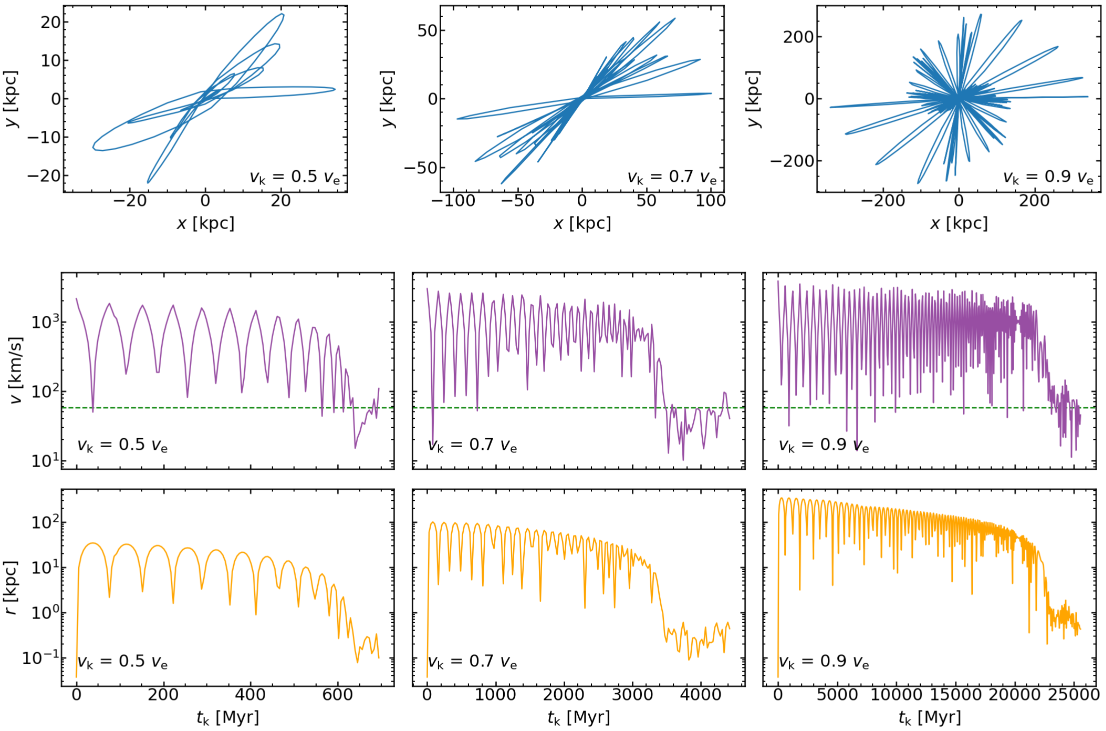

Figure 3.2: Trajectory (top row), speed (middle row) and distance from the COM of the SMBH remnant (recentred on the COM) in NGC 1600 M simulations from the time the GW kick recoil is applied. Columns (from left to right) show results for $v_{\mathrm{k}}/v_{\mathrm{e}}$ of 0.5, 0.7 and 0.9 respectively. The time t_{k} is time since the GW kick. The green dashed line indicates the estimated Brownian velocity for each SMBH, computed according to Equation 3.6. Once the SMBH reaches this velocity, we can consider it settled and in thermal equilibrium in the core of the galactic remnant.

The top row of Figure 3.2 shows the trajectory of the NGC 1600 M SMBH remnant after the GW kick, relative to the centre of mass (COM) of stars and DM. The middle and bottom rows show the speed of the remnant and distance from the COM with respect to the time of the GW kick at $t = t_\mathrm{k}$. The columns show the results for kicks of $v_\mathrm{k}/v_\mathrm{e} = 0.5$, 0.7 and 0.9, respectively. Clearly, as $v_\mathrm{k}/v_\mathrm{e}$ increases, the distance to the first apocentre, the number of passages through the centre of the core, and the time taken for the remnant to settle into Brownian motion, increase dramatically. For $v_\mathrm{k}/v_\mathrm{e} = 0.9$, the remnant makes 103 passages and takes more than a Hubble time to settle. We note that the age of NGC 1600 has been estimated at 7.3 ± 1.5 Gyr (Terlevich & Forbes, 2002), which would exclude this largest kick. However, the findings remain relevant for other galaxies with similar parameters.

The surface and volume density profiles of all four galaxies up to the first apocentre of the GW kicks are shown in Figure 3.3. The profiles show no significant change from the initial conditions (‘ICs’) of the merger until t_f, the time at which the SMBH binary separation reaches a_f. However, as the binary hardens between t_f and t_h, the time the separation reaches a_h, core formation due to binary scouring is evident as a flattening of the central profiles. Although the cores appear flatter in the surface density (2D) profiles than in the 3D density profiles, they still retain some cuspiness after scouring alone. There is, on the other hand, rapid flattening of the profiles after the GW kicks, largely complete by the time the SMBH remnant reaches its first apocentre. The surface density profiles already appear flat in 2D, corresponding to shallow cusps in 3D. With further passages, the central density gradually reduces whilst the degree of flattening is similar or mildly increased. We observe no significant difference in the profiles at these times between the different kick values and the cores do not appear to be larger than they were after scouring.

Figure 3.4 shows the profiles for NGC 1600 M during binary scouring and for the entirety of each GW kick. As the kick velocity increases and passages through the core increase in number, the profiles indicate progressive enlargement of the core. For the largest kick ($v_\mathrm{k}/v_\mathrm{e} = 0.9$) the core continues to grow even after 50 passages and becomes extremely large. The corresponding profiles for A2261-BCG M are shown in Figure 3.5. Although increasing $v_\mathrm{k}/v_\mathrm{e}$ leads to a larger final core size, the increase is much less dramatic than for NGC 1600 M. This can be attributed to the much flatter original profile of this BCG. Once a core is present, it is much more difficult to scour and eject stars.

The profiles for A2147-BCG M and NGC 6166 M are shown in Figure 3.10 and Figure 3.11 respectively. Unfortunately, due to their extremely long computational time, the kick simulations with $v_\mathrm{k}/v_\mathrm{e}$ of 0.9 for both galaxies are unfinished. However, in the case of the completed kicks, there is evidence of progressive core enlargement similar to NGC 1600 M. Interestingly, for the kick with $v_\mathrm{k}/v_\mathrm{e} = 0.5$ in NGC 6166 M, a central cusp develops inside the flattened core as the SMBH reaches Brownian motion. We interpret this as the formation of a nuclear cluster around the SMBH. This phenomenon will be examined in detail in a separate paper (Chapter 4).

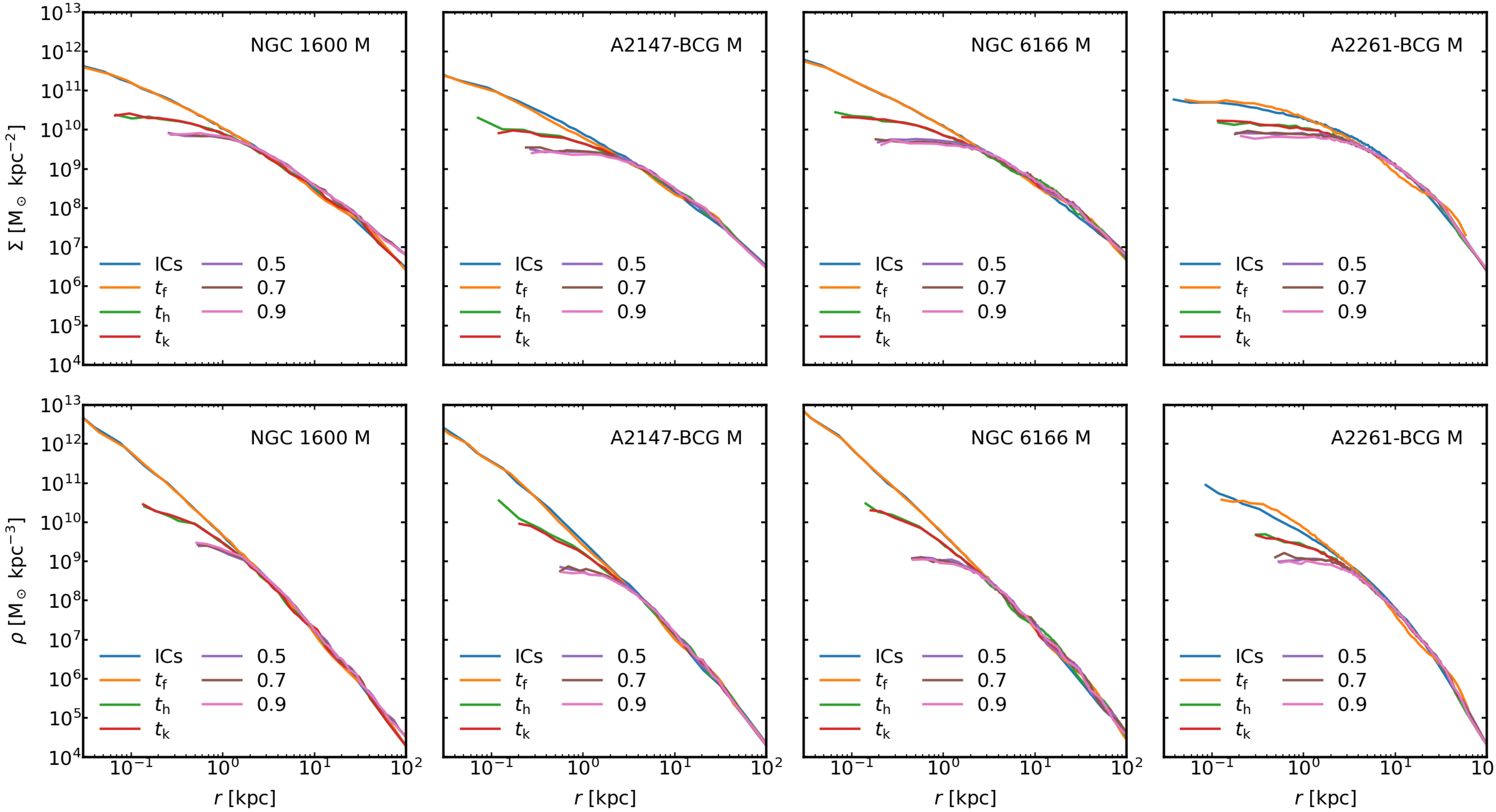

Figure 3.3: Surface density (top row) and volume density (bottom row) profiles of the stellar component of the four galaxies at different times during the evolution: at the start of the simulations (marked as ICs); at the time t_{f} when separation a_{f} is reached; at the time t_{h} when separation a_{h} is reached; at the time t_k when the GW recoil kick is applied; and at the time the first apocentre after the kick is reached, for each kick velocity (labelled by its value of $v_{\mathrm{k}}/v_{\mathrm{e}}$).

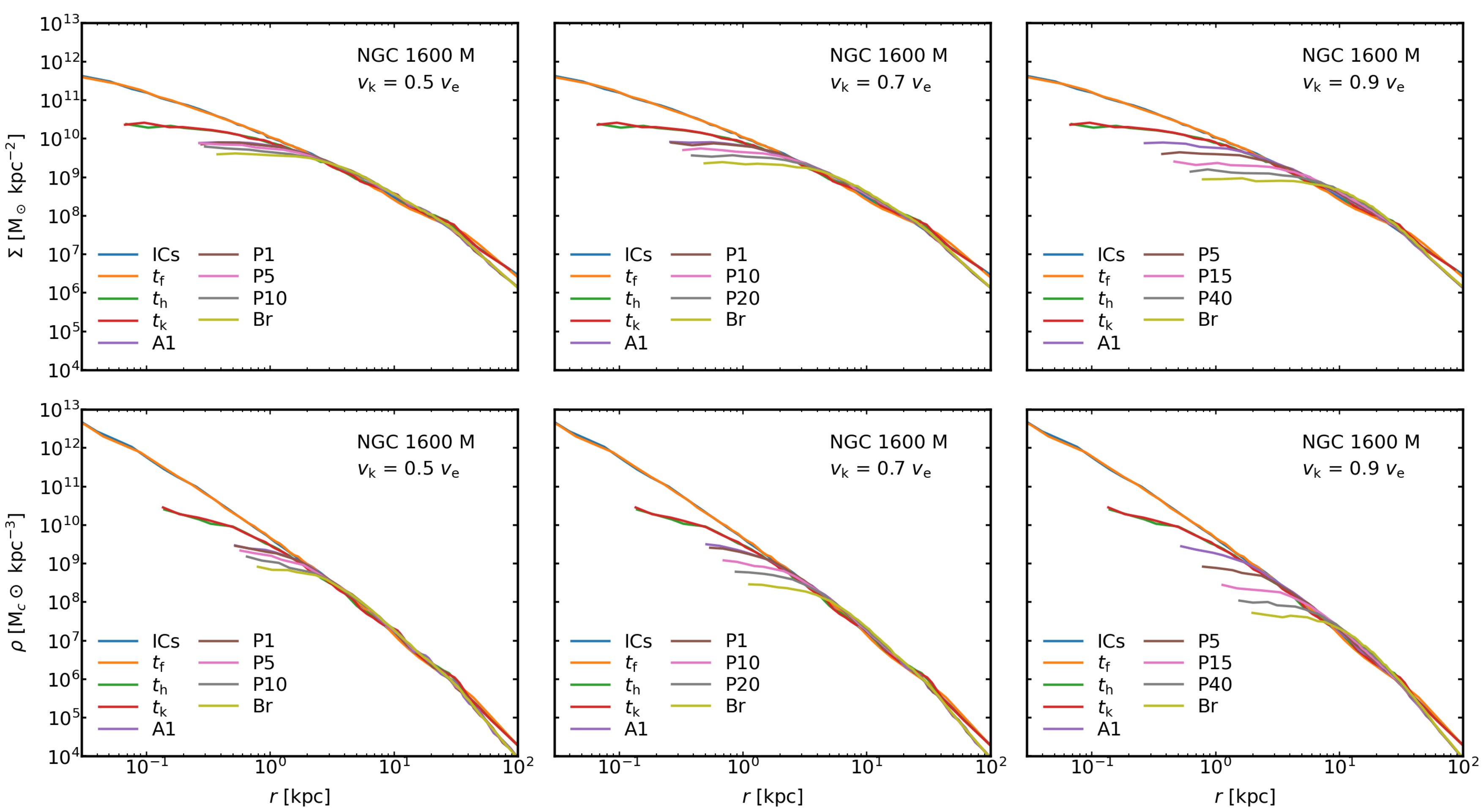

Figure 3.4: Surface density (top row) and volume density (bottom row) profiles of the stellar component during the merger (from the start of the simulation to GW recoil) and after the GW kick (here ‘A’ and ‘P’ indicate apocentre and pericentre passages, followed by the number of passages; ‘Br’ indicates the SMBH remnant has settled into Brownian motion) for galaxy NGC 1600 with $v_k/v_e = 0.5, 0.7, 0.9$, from left to right.

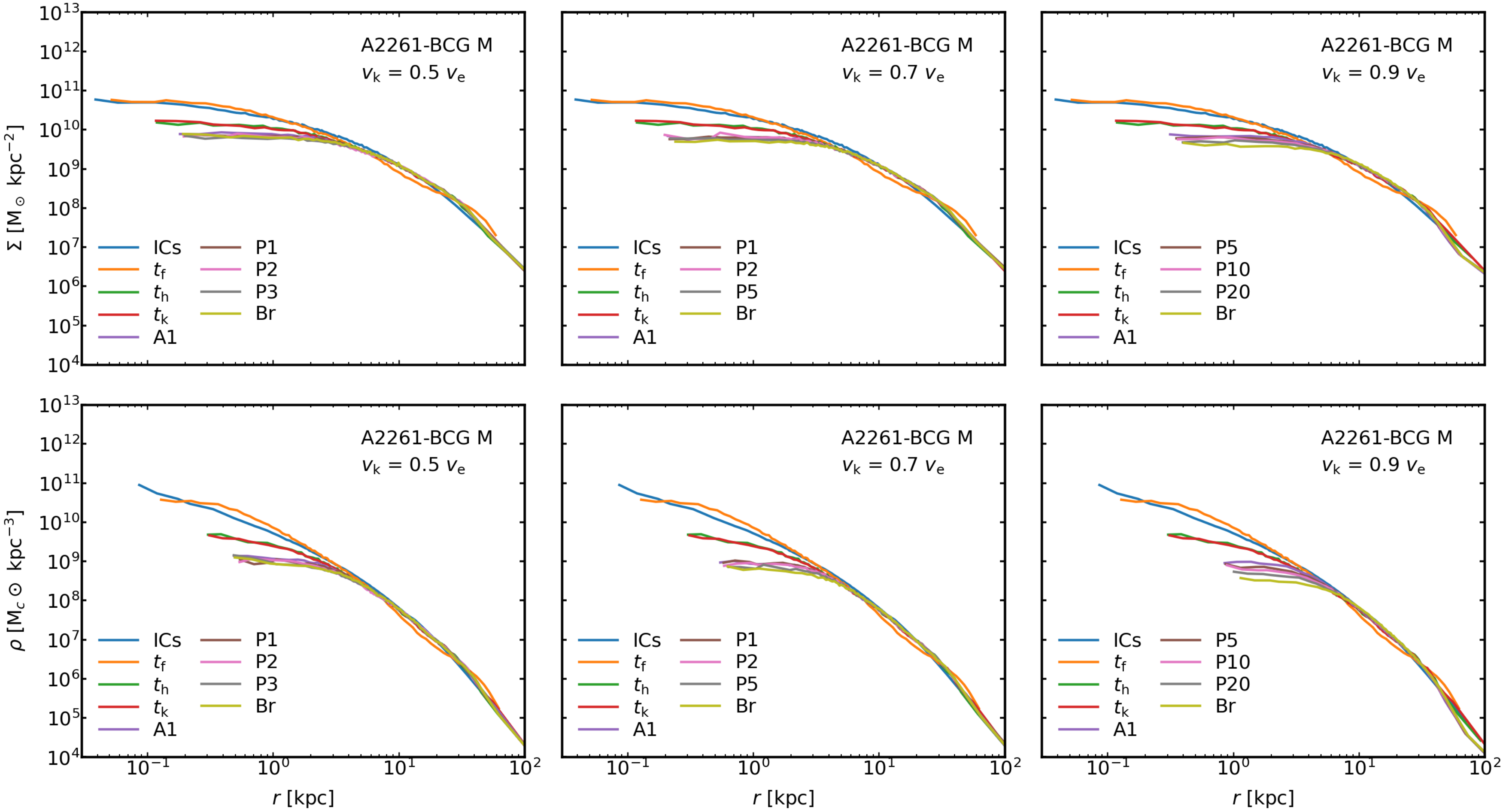

Figure 3.5: As Figure 3.4, but for galaxy A2261-BCG M.

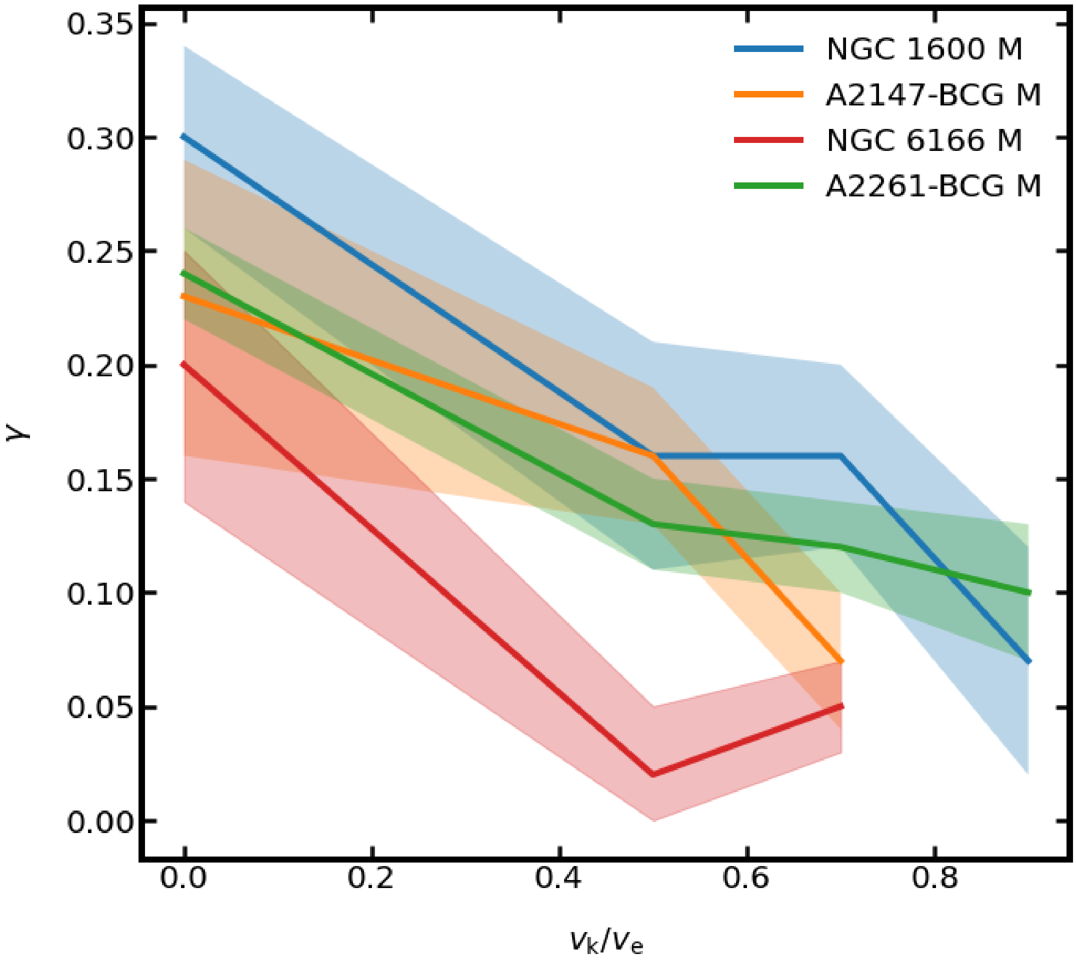

Figure 3.6: Inner logarithmic slope (γ) as a function of the ratio of kick velocity (v_k) to escape velocity (v_e) for all four galaxy remnants. A $v_\mathrm{k}/v_\mathrm{esc}$ of zero indicates scouring only. The shaded bands indicate 68% confidence intervals.

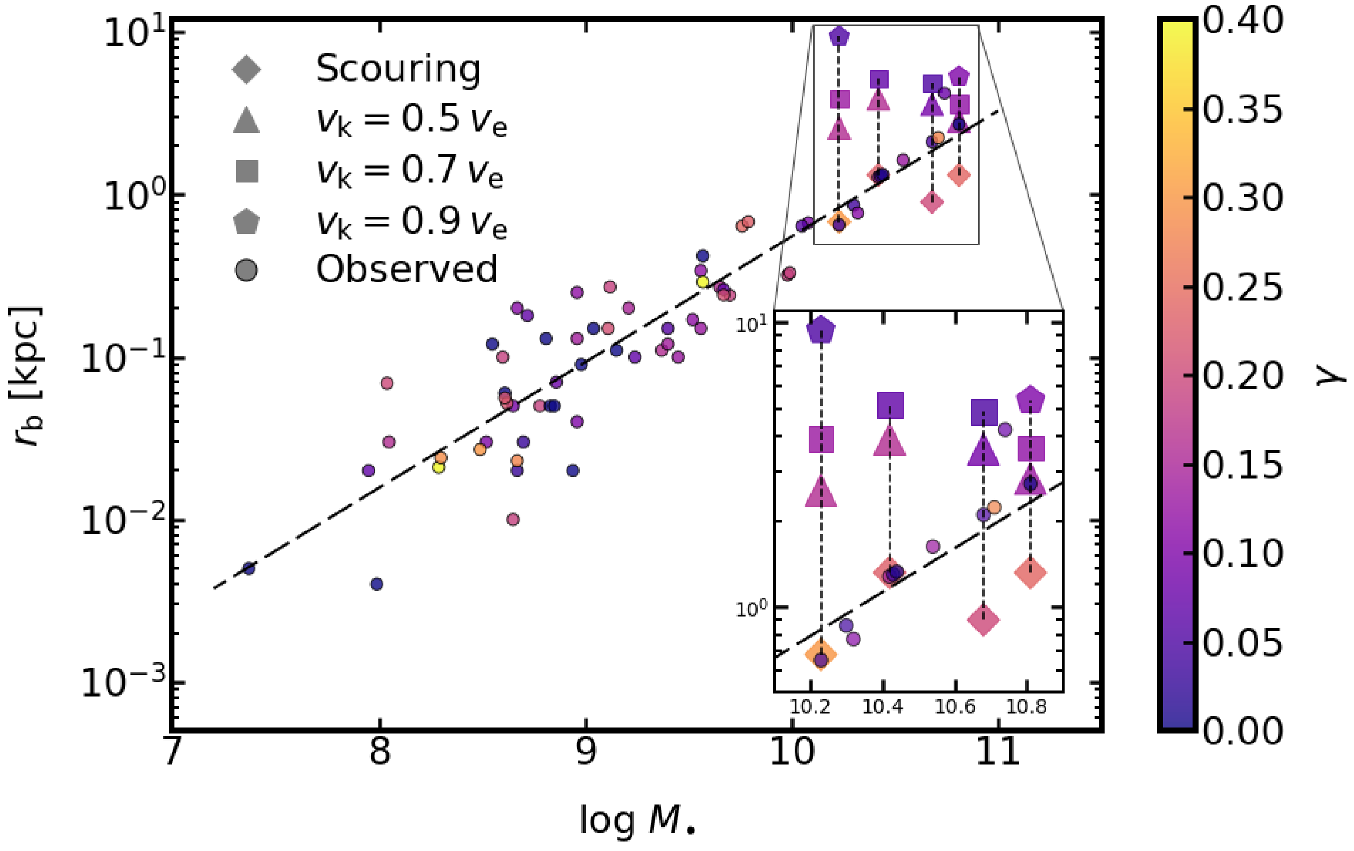

Figure 3.7: Core size and black hole mass scaling relation. Simulation results after scouring are plotted as diamonds and after GW kicks as triangles, squares and pentagons indicating a kick magnitude of 0.5, 0.7 and 0.9 of $v_\mathrm{k}/v_\mathrm{e}$ respectively. The scouring and kick results for each merger remnant are joined by a dashed line. The remnants are (from left to right) NGC 1600 M, A2147-BCG M, NGC 6166 M and A2261-BCG M. The circles are observational fits from Dullo (2019), Dullo & Graham (2014) and Rusli et al. (2013).

Markov chain Monte Carlo (MCMC) fitting of the surface density profiles are shown in Tables 3.4 and 3.5, for scouring and GW kicks, respectively. Using surface density as a proxy for luminosity, fitting was performed to the core-Sérsic profile (Graham et al., 2003):

$$I = I' \left[1 + \left(\frac{r_\mathrm{b}}{r} \right)^{\alpha} \right]^{\frac{\gamma}{\alpha}} \exp \left(- b_n \left[\frac{r^\alpha + r_\mathrm{b}^\alpha}{r_\mathrm{e}^\alpha} \right]^{1/\alpha n} \right) , \tag{3.9}$$

where I is the luminosity, γ is the inner logarithmic slope, n is the Sérsic index and α controls the sharpness of the transition between the inner power law and outer Sérsic profiles. Here, r_e is the half-light radius of the profile outside the transition region, and I' is related to I_b, the intensity at r_b, by:

$$I' = I_\mathrm{b}\, 2^{-\gamma/\alpha} \exp \left[b_n \left(\frac{2^{1/\alpha} r_\mathrm{b}}{r_\mathrm{e}} \right)^{1/n} \right] . \tag{3.10}$$

After the binary scouring phase (Table 3.4), the simulation of NGC 1600 achieved a core size of 0.68 kpc, almost equal to the observational fit of 0.65 kpc (Dullo 2019, Table 3.1). The corner plot for this fit is shown in Figure 3.12, together with an overplot of the surface density profile using the fitted parameters, which shows a very good fit to the simulation data. For A2147-BCG, the simulated size of 1.32 kpc was also very close to that observed (1.28 kpc). However, for the larger core galaxies, NGC 6166 or A2261-BCG, the simulated cores sizes after scouring were considerably smaller than the observed ones, suggesting that an additional process is required to explain their core size. We note that all galaxies retain significant cuspiness, with slopes in the range 0.20 - 0.30.

After the GW kicks (Table 3.5), the core sizes increase in all cases, and increase with increasing kick velocity for the galaxies with varying kick data available. Furthermore, γ values reduce with increasing kick velocity for all galaxies as shown in Figure 3.6. The slopes are also reduced in comparison to those after scouring. For the $v_\mathrm{k}/v_\mathrm{e} = 0.5$ kick in NGC 6166 M, the central cusp, consistent with a nuclear cluster, was excluded from the fitting. A2261-BCG M achieves a size of 2.83 kpc after a kick of $v_\mathrm{k}/v_\mathrm{e} = 0.5$, which is slightly larger than the observed size of 2.71 kpc. The corner plot and overplot for this are shown in Figure 3.13, with good fit to the data. The core size reaches a value of 3.62 kpc for a kick with $v_\mathrm{k}/v_\mathrm{e} = 0.7$, but NGC 1600 M shows an even greater increase to 3.92 kpc for this kick velocity, increasing to an enormous 9.21 kpc for $v_\mathrm{k}/v_\mathrm{e} = 0.9$.

Figure 3.7 shows the relation between core size and black hole mass for the simulation results, in comparison to observational fits from Dullo (2019), Dullo & Graham (2014) and Rusli et al. (2013). The simulation core sizes are consistent with the observational data and most simulated galaxies achieve a core size similar to the observational one with scouring alone. Interestingly, however, NGC 6166 M and A2261-BCG M require a GW kick in order to obtain a core size as large as the observed one. Furthermore, while our simulations show clearly that GW kicks produce flatter density profiles than scouring, we do not observe any clear relation between core size or black hole mass and the central slope γ in the observed samples. These results are consistent with the expectation that GW kicks, though common, should be generally modest, and configurations leading to large recoil speeds should be rare. In the non-spinning case, the maximum GW recoil speed is $< 175\,\mathrm{km\ s}^{-1}$ for all q (Gonzalez et al., 2007). Even with spin magnitudes as high as 0.8, aligned and anti-aligned with the orbital angular momentum, Schnittman & Buonanno (2007) found recoil speeds would be $< 400\,\mathrm{km\ s}^{-1}$ for $q < 4$.

In order to investigate the physical reason for the flattening of the density profiles after

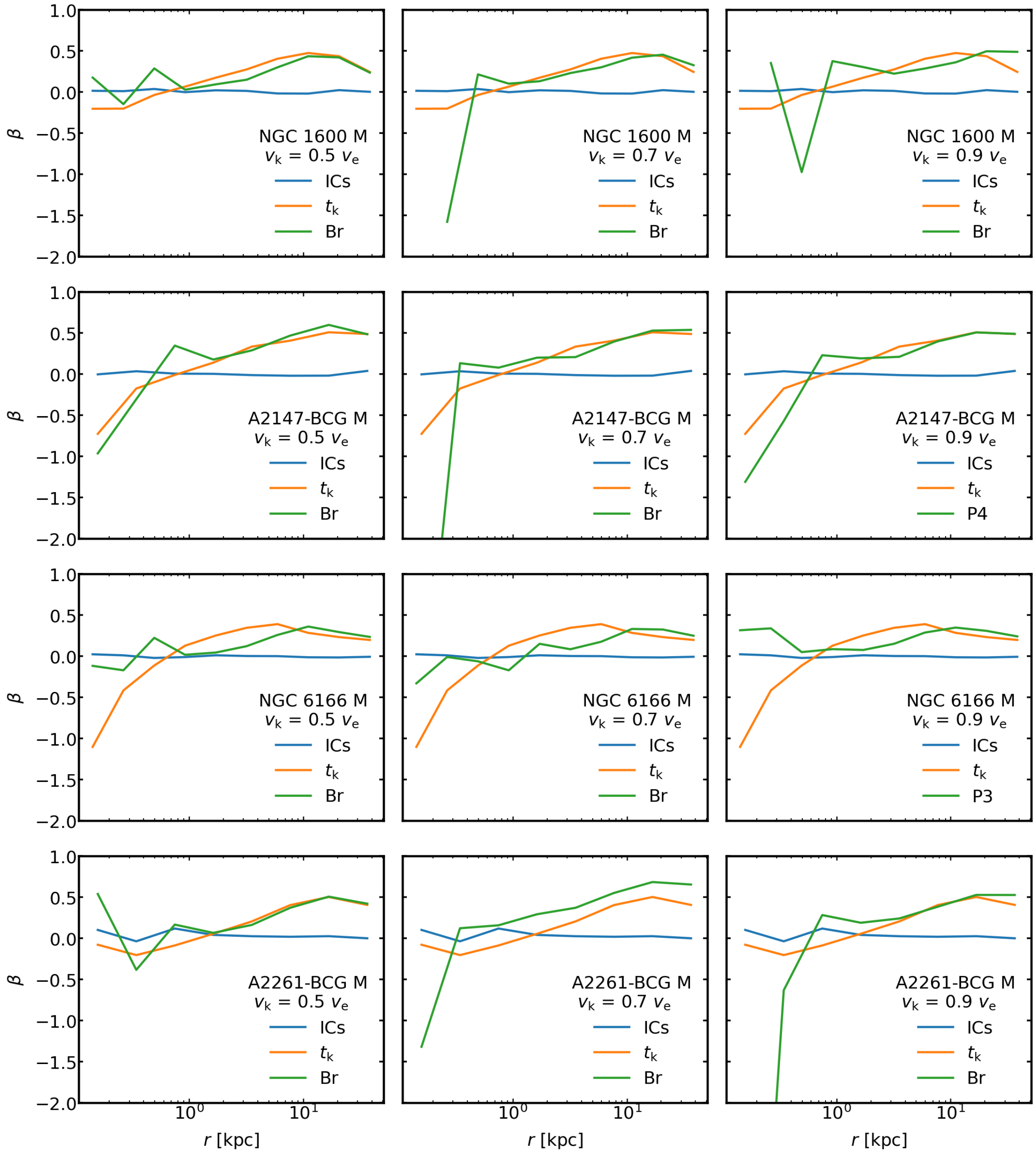

Figure 3.8: Velocity anisotropy parameter (β) as a function of radius. The rows (from top to bottom) correspond to NGC 1600 M, A2147-BCG M, NGC 6166 M and A2261-BCG M, and the columns (from left to right) to kick magnitudes of 0.5, 0.7 and 0.9 $v_\mathrm{k}/v_\mathrm{e}$ respectively. β is shown at the start of the merger ('ICs'), at the end of scouring (t_k) and the end of recoil, where the SMBH has reached Brownian motion (Br) or the most recent pericentre if the simulation is unfinished. For the latter, 'P' is followed by the number of passages.

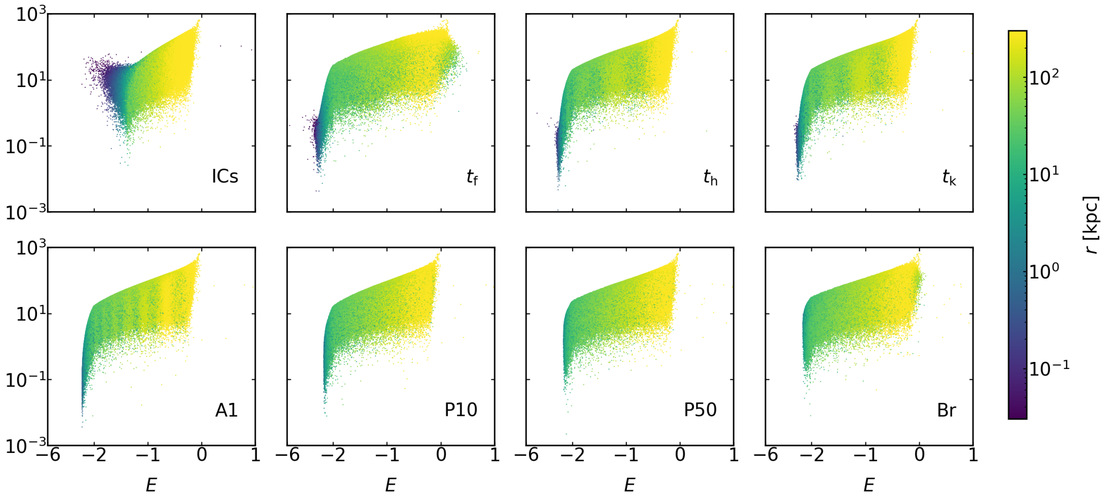

Figure 3.9: Energy - angular momentum maps for NGC 1600 M during: Initial merger and binary scouring phase (top row); after application of a GW kick velocity $v_\mathrm{k} = 0.9\, v_\mathrm{e}$ (bottom row). 'ICs' are the initial conditions at the start of the merger, t_f and t_h are the times when the SMBH separation reaches a_f, the influence radius of each SMBH, and a_h, the hard binary separation, respectively (see Equations 3.7 and 3.8), and t_k is the time when the N-body simulation is paused for the SMBH merger and GW recoil; 'A' and 'P' indicate apocentre and pericentre respectively, and are followed by the number of passages. 'Br' indicates the SMBH remnant has settled into Brownian motion. The colourmap shows the radial distance from the centre of mass of the merger remnant.

GW recoil, we analyse the evolution of the stellar velocity anisotropy and populations in energy and angular momentum space. The velocity anisotropy parameter β is given by:

$$\beta = 1 - \frac{\sigma_\theta^2 + \sigma_\phi^2}{2\sigma_\mathrm{r}^2}\,, \tag{3.11}$$

where σ_θ, σ_ϕ and σ_r are the components of the stellar velocity dispersion in spherical coordinates. Hence, $\beta = 0$ indicates isotropy, $\beta = 1$ that all orbits are radial, and $\beta = -\infty$ that they are circular. In Figure 3.8, β is plotted as a function of radius at three timepoints: the start of the merger (ICs), the end of the scouring phase (t_k), and where the SMBH has reached Brownian motion (Br) at the end of the kick (or the most recent pericentre where the simulation is unfinished). This confirms that scouring does preferentially remove stars on radial orbits, but the effect of GW kicks appears dependent on their strength: kicks of $v_\mathrm{k}/v_\mathrm{e} = 0.5$ appear to have the same degree of anisotropy or less than after scouring but, in general, kicks with $v_\mathrm{k}/v_\mathrm{e}$ of 0.7 or 0.9 preferentially remove additional stars on radial orbits centrally, increasing the anisotropy.

The total energy E of stellar particles in NGC 1600 M is plotted against their angular momentum J in Figure 3.9 from the start of the simulation to the time of application of the GW kick (top row), and at various times following the GW kick of $v_\mathrm{k}/v_\mathrm{e} = 0.9$ (bottom row). A significant change in the $E - J$ plane can be seen between the start of the simulation and time t_f in the initial phase of the merger. By this time, the most central particles have the lowest energy and angular momentum. The latter is consistent with results from Lagos et al. (2018). Some of the low energy central particles are no longer present after hardening, a sign that close interactions with the BHB have ejected stars to larger radii through the slingshot process. This process slows down around the time the binary becomes hard, as most stars initially on low angular momentum orbits have been ejected, and we see little change from time t_{h} and the application of the GW kick. In this phase, only stars that are scattered to lower angular momentum orbits, typically from larger distances, interact with the binary. A further loss of low energy central particles can be seen in the bottom row of Figure 3.9 after the GW recoil kick. In this phase, the SMBH makes repeated excursions to large radii and then back to the centre, displacing stars and causing a further reduction in central density. Typically, low angular momentum stars are removed from the core of the galaxy over time.

Particle tracking shows that higher energy particles have been ejected to larger radii during the initial merger, consistent with the expected increase in the effective radius. During hardening of the binary, there is outward movement of particles at most energies. This is even more pronounced during the GW kick, with central and low angular momentum particles moving to higher radii and gaining angular momentum.

Table 3.4: MCMC core-Sérsic fits after binary scouring.

Remnant	r_{b} [kpc]	γ	α	n	r_{e} [kpc]	$\log(\Sigma_{\mathrm{b}}$ $/10^9\,M_\odot\,\mathrm{kpc}^{-2})$
NGC 1600 M	$0.68^{+0.04}_{-0.05}$	$0.30^{+0.04}_{-0.04}$	$3.0^{+0.5}_{-0.4}$	$6.0^{+0.1}_{-0.2}$	$22.3^{+0.4}_{-0.7}$	$23.07^{+0.05}_{-0.05}$
A2147-BCG M	$1.32^{+0.15}_{-0.16}$	$0.23^{+0.06}_{-0.07}$	$1.4^{+0.2}_{-0.1}$	$6.3^{+0.1}_{-0.1}$	$24.7^{+2.5}_{-1.4}$	$21.95^{+0.10}_{-0.09}$
NGC 6166 M	$0.90^{+0.09}_{-0.09}$	$0.20^{+0.05}_{-0.06}$	$1.15^{+0.05}_{-0.05}$	$9.0^{+0.1}_{-0.1}$	$60.1^{+0.2}_{-0.1}$	$22.79^{+0.08}_{-0.08}$
A2261-BCG M	$1.32^{+0.04}_{-0.05}$	$0.24^{+0.02}_{-0.02}$	$62.4^{+25.8}_{-28.7}$	$2.15^{+0.02}_{-0.02}$	$13.1^{+0.1}_{-0.1}$	$22.98^{+0.02}_{-0.02}$

Table 3.5: MCMC Core-Sérsic fits after GW kicks.

Galaxy	$v_\mathrm{k}/v_\mathrm{e}$	v_k [km s^{-1}]	r_b [kpc]	γ	α	n	r_e [kpc]	log (Σ_b /10^9 M$_\odot$ kpc^{-2})
NGC 1600 M	0.5	2121	$2.48^{+0.09}_{-0.10}$	$0.16^{+0.05}_{-0.05}$	$5.4^{+0.8}_{-0.7}$	$6.2^{+0.1}_{-0.1}$	$22.5^{+0.2}_{-0.1}$	$21.71^{+0.03}_{-0.03}$
	0.7	2969	$3.92^{+0.12}_{-0.13}$	$0.16^{+0.04}_{-0.04}$	$4.7^{+0.7}_{-0.6}$	$6.1^{+0.1}_{-0.1}$	$22.6^{+0.2}_{-0.2}$	$21.11^{+0.03}_{-0.03}$
	0.9	3818	$9.21^{+0.89}_{-0.61}$	$0.07^{+0.05}_{-0.05}$	$2.5^{+0.7}_{-0.5}$	$6.1^{+0.1}_{-0.1}$	$22.5^{+0.2}_{-0.2}$	$20.02^{+0.06}_{-0.07}$
A2147-BCG M	0.5	1619	$3.89^{+0.11}_{-0.11}$	$0.16^{+0.03}_{-0.03}$	$3.8^{+0.5}_{-0.4}$	$6.3^{+0.1}_{-0.1}$	$26.3^{+2.5}_{-2.4}$	$20.81^{+0.02}_{-0.02}$
	0.7	2267	$5.15^{+0.13}_{-0.13}$	$0.07^{+0.03}_{-0.03}$	$3.6^{+0.4}_{-0.4}$	$6.3^{+0.1}_{-0.1}$	$25.8^{+2.7}_{-2.1}$	$20.43^{+0.02}_{-0.02}$
NGC 6166 M	0.5	2284	$2.98^{+0.05}_{-0.04}$	$0.02^{+0.03}_{-0.02}$	$6.9^{+0.6}_{-0.5}$	$9.07^{+0.02}_{-0.05}$	$60.5^{+0.8}_{-0.4}$	$21.09^{+0.01}_{-0.01}$
	0.7	3198	$4.86^{+0.10}_{-0.10}$	$0.05^{+0.02}_{-0.02}$	$3.2^{+0.3}_{-0.2}$	$9.0^{+0.1}_{-0.1}$	$68.7^{+7.4}_{-6.1}$	$20.98^{+0.02}_{-0.02}$
A2261-BCG M	0.5	1772	$2.83^{+0.09}_{-0.09}$	$0.13^{+0.02}_{-0.02}$	$5.4^{+1.0}_{-0.8}$	$1.94^{+0.06}_{-0.03}$	$13.1^{+0.1}_{-0.1}$	$22.32^{+0.02}_{-0.02}$
	0.7	2498	$3.62^{+0.12}_{-0.13}$	$0.12^{+0.02}_{-0.02}$	$3.7^{+0.4}_{-0.3}$	$2.1^{+0.1}_{-0.1}$	$13.0^{+0.1}_{-0.1}$	$22.02^{+0.02}_{-0.02}$
	0.9	3212	$5.32^{+0.17}_{-0.17}$	$0.10^{+0.03}_{-0.03}$	$3.3^{+0.4}_{-0.4}$	$2.05^{+0.10}_{-0.10}$	$13.0^{+0.1}_{-0.1}$	$21.01^{+0.02}_{-0.02}$

3.4 Discussion and Conclusions

We have studied the physical processes of black hole binary scouring and gravitational wave (GW) recoil, which together may result in the formation of very large cores, as observed in a few of the most massive elliptical galaxies.

We find that binary scouring alone can form large cores of up to $\sim 1.3\,\mathrm{kpc}$, such as those observed in NGC 1600 and A2147-BCG. However, an additional process is required to form the largest cores, greater than 2 kpc, observed in galaxies such as NGC 6166 and A2261-BCG. We have shown that GW recoil can form these very large cores with kicks of less than half of the escape speed v_e for the 2.11 kpc core of NGC 6166 and the 2.71 kpc core of A2261-BCG. This corresponds to kick velocities of less than $\sim 2300\,\mathrm{km\ s^{-1}}$ and $\sim 1800\,\mathrm{km\ s^{-1}}$, respectively, well below the theoretical maximum recoil for spin-dominated kicks from numerical relativity simulations, found by Campanelli et al. (2007b) to be $\sim 4000\,\mathrm{km\ s^{-1}}$ and by Lousto & Healy (2019) to be $\sim 5000\,\mathrm{km\ s^{-1}}$. Indeed, the latter found the probability of a recoil kick in the range 1000-2000 $\mathrm{km\ s^{-1}}$ to be $\sim 5\%$. We note that, in the case of such spin-dominated kicks, equal-mass mergers have higher recoil velocities than smaller mass ratio mergers. If we define the mass ratio as $q \leq 1$, the expected scaling is $v_\mathrm{k} \propto q^2$ (Campanelli et al., 2007a).

We also find that GW recoil leads to flatter inner density profiles than binary scouring alone. This occurs rapidly after the kick and is apparent by the first apocentre. In general, the values of the inner slope γ found after GW kicks are much closer to those of the observed profiles than those with binary scouring alone. This might imply that all the studied galaxies have experienced some GW recoil in addition to scouring. However, the degeneracies involved in fitting a six-parameter model such as the core-Sérsic profile with an MCMC procedure make this hard to claim definitively.

Nasim et al. (2021) performed multiple simulations of core formation in A2261-BCG. However, only one used the same parameters including $M_\bullet$ used in this study. In that simulation, they found a core radius of 0.9 kpc at the end of scouring, 2.64 kpc after a GW kick with $v_\mathrm{k}/v_\mathrm{e} = 0.3$, and 2.96 kpc after a $v_\mathrm{k}/v_\mathrm{e} = 0.8$ kick. We found a slightly larger core after scouring (1.32 kpc), a core size between their $v_\mathrm{k}/v_\mathrm{e} = 0.3$ and $v_\mathrm{k}/v_\mathrm{e} = 0.8$ kicks for our $v_\mathrm{k}/v_\mathrm{e} = 0.5$ kick (2.98 kpc), and a larger core after our $v_\mathrm{k}/v_\mathrm{e} = 0.7$ kick (3.62 kpc) than their $v_\mathrm{k}/v_\mathrm{e} = 0.8$ kick. The differences are likely due to differences in the fitting procedure.

Our results fit the r_b-$M_\bullet$ relation of observed core galaxies well (Figure 3.7). One might expect GW recoil heating to scale with the mass of the SMBH remnant, so that galaxies with more massive SMBHs display flatter cores. However, we find no clear relation between $M_\bullet$ and γ in the observed data. This might be due to the rarity of large recoils, which require both large SMBH masses and particular spin configurations, or due to the fitting procedure being unable to robustly measure gamma over the region of interest. We will examine this in more detail in forthcoming work.

Finally, we find that high GW kicks preferentially remove low angular momentum stars from cores. Although this is already known to occur in binary scouring, kicks with $v_\mathrm{k}/v_\mathrm{e}$ of 0.7 or higher can further remove these stars, leading even greater central anisotropy.

Overall, we find GW kicks are a very plausible cause for the formation of the largest cores. Since two of the modelled SMBHs are insufficient to form the observed core sizes by scouring alone, without an additional mechanism the SMBH masses would have to lie well above the r_b-$M_\bullet$ relation, potentially $\gtrsim 10^{11}\mathrm{M}_\odot$. GW recoil avoids invoking such hypermassive black holes. Indeed, core sizes greater than $\sim 2\,\mathrm{kpc}$ may indicate that significant GW recoil has occurred, and flat cores may be a marker for some degree of recoil.

However, other mechanisms of large core formation have been proposed: stalling infallers could form very large cores as additional nuclear components rather than by central deficits (Goerdt et al., 2010; Bonfini & Graham, 2016); resonant interactions between SMBHs and multiple recoil events could form large cores in multiple SMBH systems (Kulkarni & Loeb, 2012). We will consider such processes in future work.

3.5 Appendices

3.5.1 Density profiles for A2147-BCG and NGC 6166

Figure 3.10 shows the surface density (top row) and volume density (bottom row) profiles for A2147-BCG M during both binary scouring and for the entirety of each GW kick. Figure 3.11 shows the corresponding profiles for NGC 6166 M.

Due to their long computational time, the $v_\mathrm{k}/v_\mathrm{e}$ of 0.9 runs are unfinished. However, where completed, there is progressive core enlargement similar to NGC 1600 M (Figure 3.4). Furthermore, for the $v_\mathrm{k}/v_\mathrm{e}$ of 0.3 runs, there is increased flattening at the first apocentre for both galaxies, and the second for A2147-BCG M, compared to later times. We attribute this to the higher bound mass at low $v_\mathrm{k}/v_\mathrm{e}$ removing stars from the centre in the initial phases, some of which is subsequently returned.

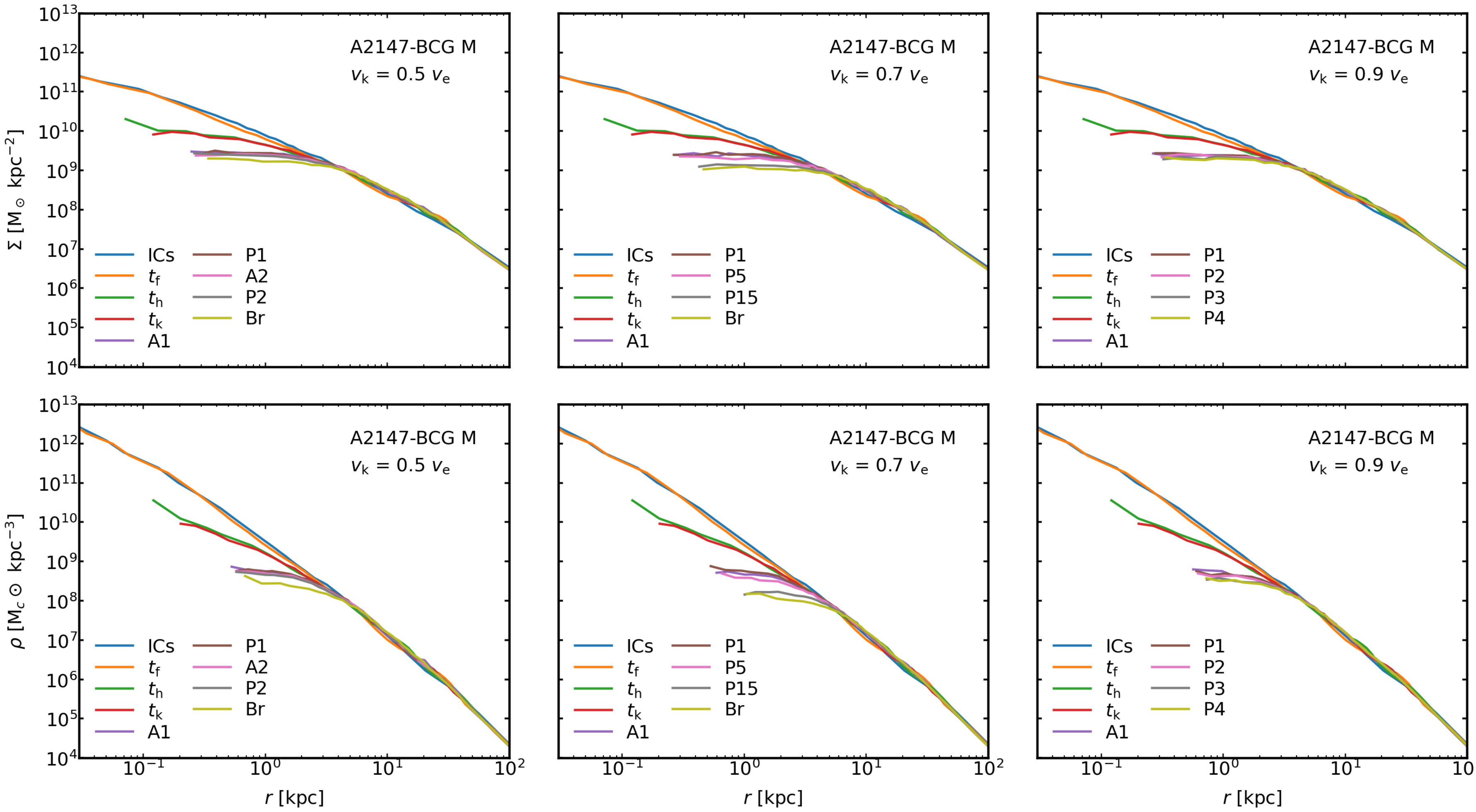

Figure 3.10: Surface density (top row) and spatial density (bottom row) profiles during merger and after GW kick for A2147-BCG. v_k/v_e 0.5 (1st col.), 0.7 (2nd col.) and 0.9 (3rd col.). ICs indicates start of galaxy merger, $t_k = 0$ is time of SMBH merger. 'A' and 'P' indicate apocentre and pericentre respectively, and are followed by the number of passages. 'Br' indicates the SMBH remnant has settled into Brownian motion.

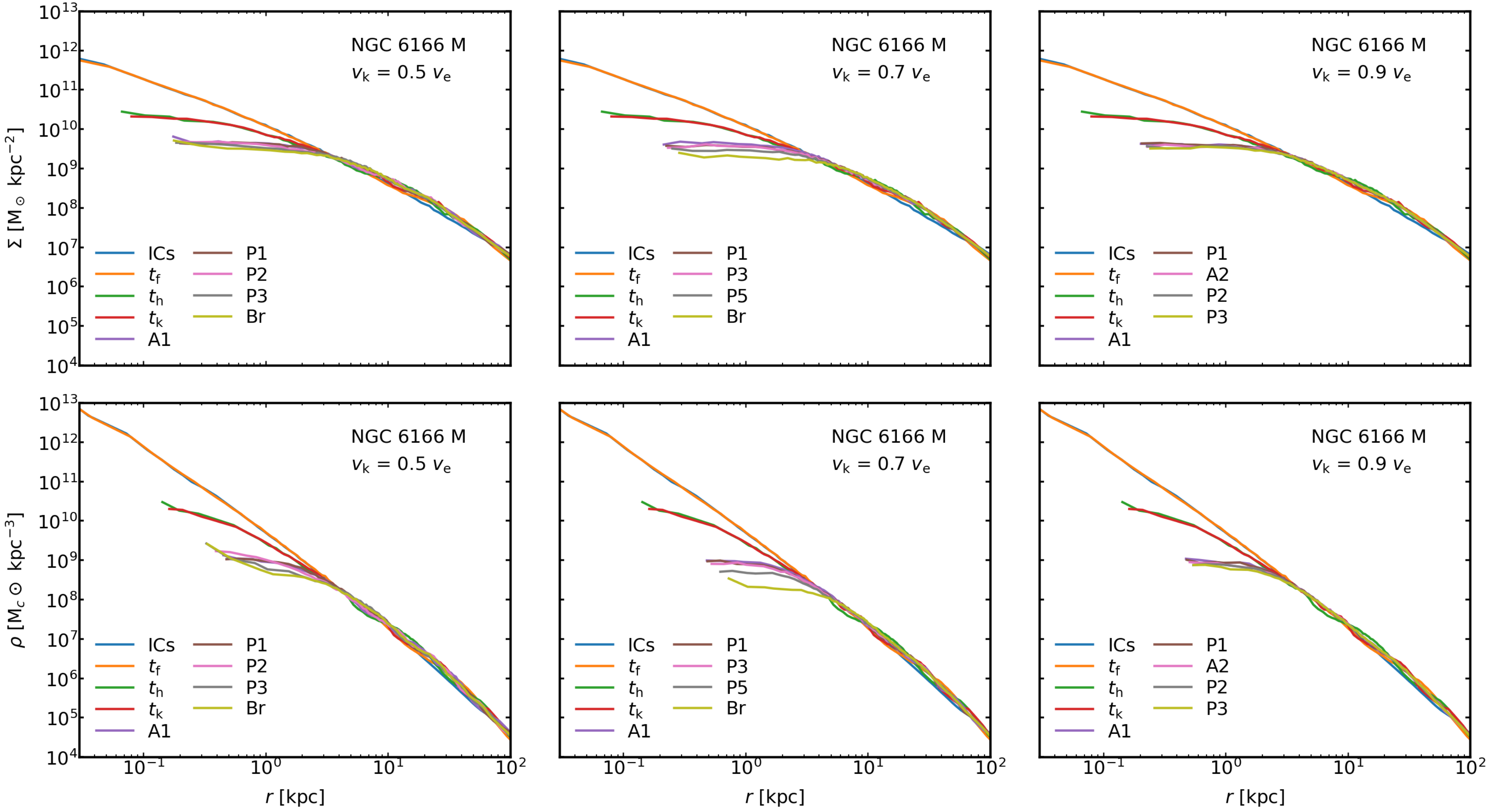

Figure 3.11: As for Figure 3.10, but for NGC 6166 M.

3.5.2 Corner plots for MCMC fits

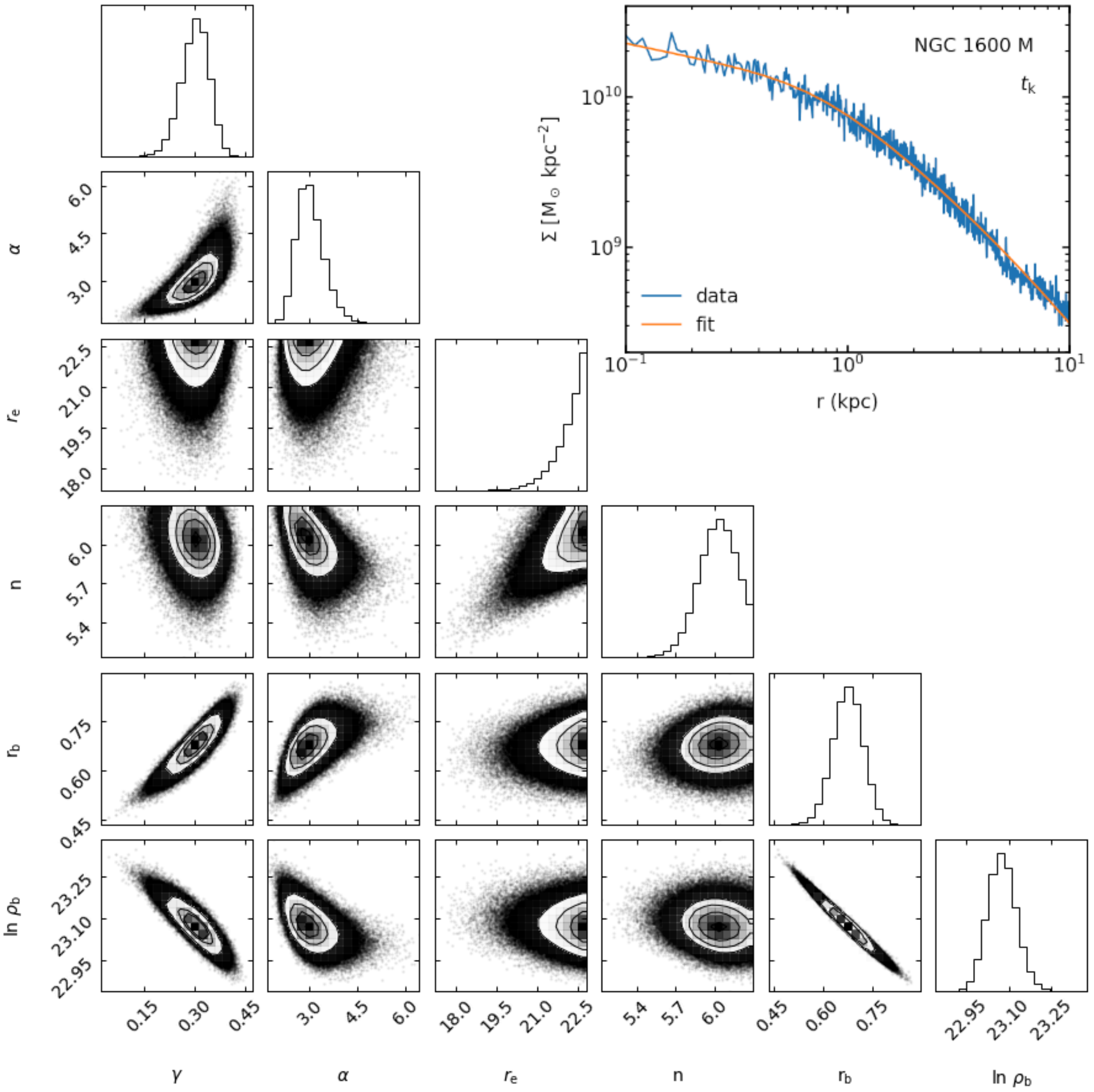

Figure 3.12: Corner plot resulting from the MCMC core-Sérsic fit to NGC 1600 M after binary scouring. The inset panel shows the surface density profile obtained from the N-body data compared with the analytic fitted profile.

Figure 3.12 shows the corner plot for the MCMC core-Sérsic fit to the surface density profile of the NGC 1600 M remnant after the binary scouring phase. The core size of 0.68 kpc is almost equal to the observational fit of 0.65 kpc (Dullo 2019, Table 3.1). The inset shows an overplot of the surface density profile using the fitted parameters, which shows a very good fit to the simulation data.

Figure 3.13 shows the corner plot for the MCMC core-Sérsic fit to the surface density profile of A2261-BCG M remnant after a kick of $v_\mathrm{k}/v_\mathrm{e} = 0.5$. The core achieves a size of 2.83 kpc, which is slightly larger than the observed size of 2.71 kpc. The overplot again fits the data well.

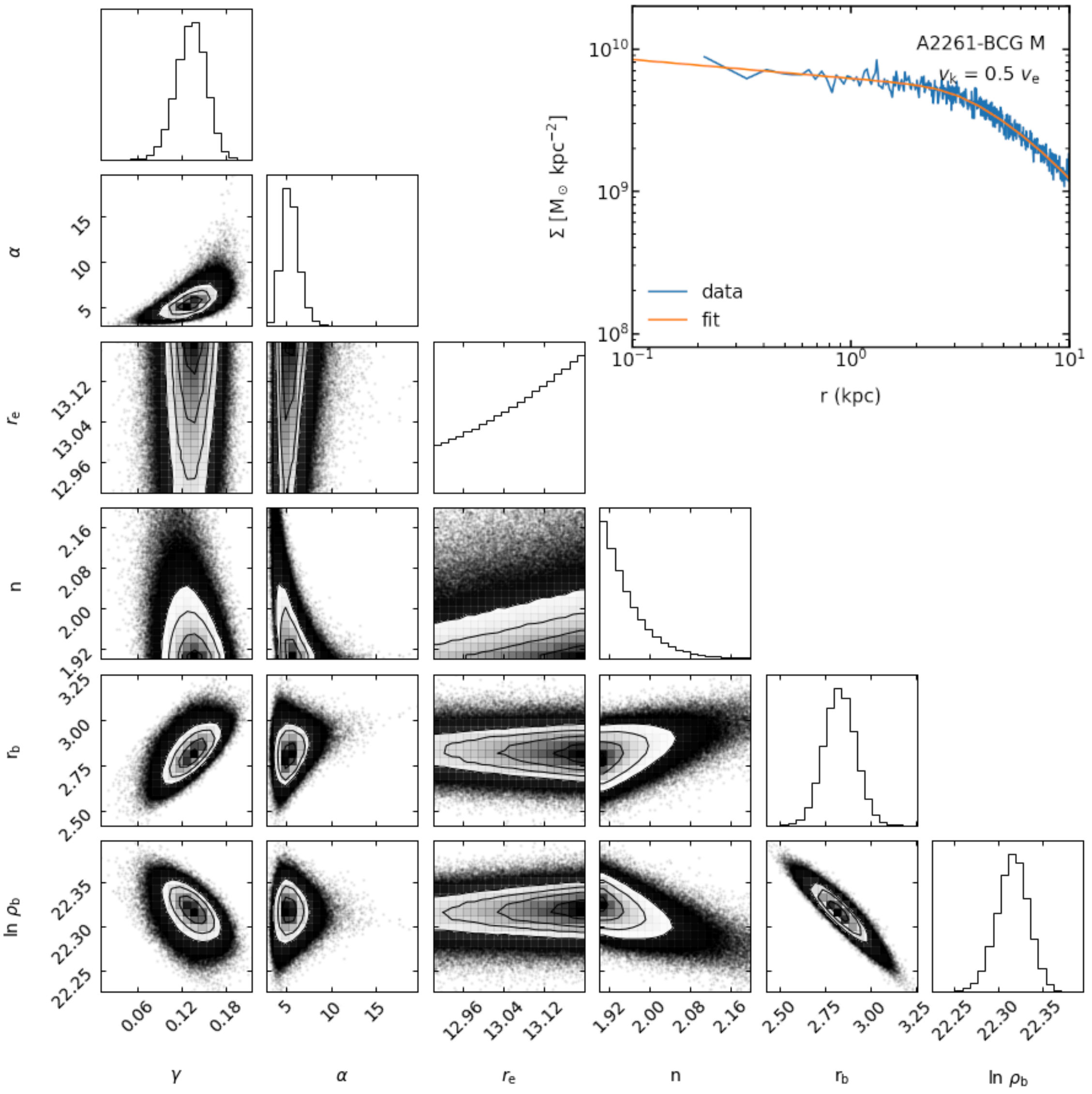

Figure 3.13: Corner plot resulting from the MCMC core-Sérsic fit to A2261-BCG M after the GW kick $v_{\rm k}/v_{\rm e} = 0.5$ is applied. The inset panel shows the surface density profile obtained from the N-body data compared with the analytic fitted profile.

Chapter 4

Black hole dragging: a new mechanism for forming nuclear star clusters

In this chapter, I examine the effects of smaller GW recoil kicks, when the kicked SMBH has higher bound mass. I find that, whilst dynamical friction of the SMBH can form a flattened core, the bound mass dragged back to the centre of mass with the SMBH can result in a central density within it. I propose this new 'black hole dragging' mechanism as a potential explanation for the nuclear star clusters observed at the centres of some galaxies with large cores. The work for this chapter has been submitted for publication in The Astrophysical Journal: Nader Khonji, Alessia Gualandris, Justin I. Read, Walter Dehnen. It will be resubmitted shortly following favourable reviewer comments.

Abstract

Many galaxies contain bright, compact central clusters known as nuclear star clusters (NSCs). Two main formation mechanisms have been proposed: infall of globular clusters and/or in situ star formation. We present a new mechanism for forming NSCs in giant elliptical galaxies: black hole dragging. After a major merger of galaxies and merger of their supermassive black holes (SMBHs), the newly-merged SMBH can receive a gravitational wave recoil kick. We show that recoiling SMBHs induce two effects on the galaxy's background stars. Firstly, some central stars become bound to the SMBH and co-move with it. Secondly, as the SMBH falls back by dynamical friction, it ejects background stars forming a central stellar core. For very low recoil velocity (v $\lesssim$ 500 km s^{-1}), the mass of co-moving stars is maximised, but the scouring effect is minimised. Here, the background stellar density is higher than the density of co-moving stars, yielding no observable effect on the galaxy's surface brightness profile. For very high recoil velocity (v $\gtrsim$ 1000 km s^{-1}), few stars co-move, but the scouring effect is now maximised. However, for intermediate recoil velocities (500 km s^{-1} $\lesssim$ v $\lesssim$ 1000 km s^{-1}), the scouring effect lowers the central density of stars below the density of co-moving stars, producing a nucleus reminiscent of an NSC, clearly visible in the galaxy's surface brightness profile. Our mechanism provides a route for even giant ellipticals that contain SMBHs to host an NSC. Such NSCs should have indistinguishable colours, ages and chemistry from non-NSC central stars.

4.1 Introduction

Nuclear star clusters (NSCs) are dense, bright stellar clusters, located in the central regions of galaxies. They have been defined as 'stellar light above the inward extrapolation of the host galaxy's surface brightness profile on scales of $\lesssim 50\,\mathrm{pc}$' (Neumayer et al., 2020), and usually coincide with the photometric (Böker et al., 2002) and dynamical (Neumayer et al., 2011) center of their host galaxy. However, there is a lack of clarity in the terminology, and the same objects are often referred to as nuclei. (e.g. Lauer et al., 2005).

Most NSCs are small, with a median effective radius (r_e) of 3 pc (Neumayer et al., 2020), similar to globular clusters (GCs, Harris, 2010), but the distribution has a significant tail towards large r_e, with NSCs in some spiral and elliptical galaxies reaching 40 pc (Georgiev et al., 2016; Côté et al., 2006). NSC stellar masses (M_N) are much larger than those of GCs and scale with galaxy stellar mass (M_*), approximately as $M_\mathrm{N} \propto M_*^{1/2}$ (Balcells et al., 2002; Scott & Graham, 2013), though the relation appears almost linear for high mass NSCs in spiral galaxies (Neumayer et al., 2020). Many NSCs are non-spherical, with ellipticities of up to 0.6 (Neumayer et al., 2020). In elliptical galaxies there is a correlation between the ellipticity and mass of their NSCs (Spengler et al., 2017).

The determination of stellar ages and metallicities is extremely difficult for all but the nearest galaxies, so population fitting of integrated light must be used (Tinsley, 1978) to determine the most likely age-metallicity combination. For elliptical galaxies, this indicates that metallicities are generally lower in low-mass galaxies than in those of higher mass, both in absolute terms and relative to that of their host galaxies (Neumayer et al., 2020). However, there is significant stochasticity for individual galaxies. In spiral galaxies, spectroscopic studies indicate a mixture of stellar populations. Although old stars dominate in terms of mass, there is a significant young population.

There are two main theories for the formation of NSCs: (i) dynamical friction followed by merging of GCs; and (ii) in-situ star formation after infall of gas.

Dynamical friction (Chandrasekhar, 1943) of GCs was first proposed by Tremaine et al. (1975), shortly after the detection of a NSC in M31. Their calculations show that a NSC of $M_\mathrm{N} \sim 10^7\,\mathrm{M}_\odot$ could form in $\sim 10^{10}$ years. Observational evidence for this mechanism includes a deficit of GCs in the central regions (Lotz et al., 2001; Capuzzo-Dolcetta & Mastrobuono-Battisti, 2009), and a correlation between the fraction of galaxies with NSCs and those with GCs in low-mass cluster ellipticals observed in the Virgo cluster (Sánchez-Janssen et al., 2019). Furthermore, semi-analytic simulations have formed NSCs with density profiles (Antonini, 2013), and mass and radius (Gnedin et al., 2014), that are largely consistent with observations. In addition, N-body simulations have matched their shape (Capuzzo-Dolcetta & Miocchi, 2008; Hartmann et al., 2011; Antonini et al., 2012). They also show that, if sufficient GCs are formed early enough, NSCs could be produced from dynamical friction of GC systems within a Hubble time. However, this mechanism does not explain the significant proportion of young stars seen in NSCs of spiral galaxies.

Infall of gas to the nucleus generally leads to star formation, a process that may occur more than once if interrupted by gas dispersion through supernova feedback and stellar winds followed by later gas infall (Loose et al., 1982). Wet mergers are likely to lead to gas infall and starbursts (Mihos & Hernquist, 1996; Gray et al., 2024). However, since spiral galaxies which show no signs of previous mergers also have NSCs, other mechanisms have been proposed. These include bar-driven inspiral (Shlosman et al., 1990; Schinnerer et al., 2006) and mergers of gaseous spiral arms (Bekki, 2007).

Neumayer et al. (2020) argue that GC dynamical friction and gas infall are more important in lower and higher mass galaxies respectively, with the transition occurring at

$M_* \sim 10^9$ M$_\odot$, but with significant scatter. Their evidence for this includes the metallicity differences described above and the finding that the fraction f_N of galaxies with NSCs tracks the fraction of galaxies with GCs (Sánchez-Janssen et al., 2019).

The fraction f_N of galaxies hosting a NSC has been found from imaging via the Hubble Space Telescope to be $\sim 50\%$ for spiral galaxies (Carollo et al., 1997, 2002), increasing to $\sim 80\%$ for late-type spirals (Böker et al., 2002). Surveys of galaxy clusters show that most elliptical galaxies also have detectable NSCs: $f_\mathrm{N} = 66$-82% for elliptical galaxies in the Virgo cluster (Côté et al., 2006) and $f_\mathrm{N} \sim 80\%$ for dwarf elliptical galaxies in the Coma cluster (Den Brok et al., 2014).

In general, f_N varies with M_* (or galaxy luminosity). Overall, there are nuclei in the vast majority of galaxies of intermediate stellar mass ($M_* = 10^{8\text{-}10}\,\mathrm{M}_\odot$). There is relatively little data available for spiral galaxies, but what there is suggests that f_N drops at low brightness, to around 0.1 at $M_V > -17$ (Georgiev et al., 2009).

For elliptical galaxies, f_N peaks at > 0.9 for galaxies with $M_* \sim 10^9\,\mathrm{M}_\odot$ (Sánchez-Janssen et al., 2019) or $M_I \sim -18$ (Den Brok et al., 2014). At the low mass / brightness end it falls to around zero for $M_* \sim 10^5\,\mathrm{M}_\odot$ (Sánchez-Janssen et al., 2019) or $M_I \sim -10$ (Muñoz et al., 2015), which could be partly owed to the difficulty of detecting faint nuclei. There is also a drop in f_N above $10^9\mathrm{M}_\odot$. Côté et al. (2006) found $f_\mathrm{N} \sim 0$ for $M_B \lesssim -20.5$ and related it to the transition from "cusp" to "core" galaxies; the surface brightness profiles of these brighter elliptical galaxies tends to be flattened, forming a central core, whereas those of dimmer galaxies tend to continue to rise steeply as a cusp.

Cores are thought to be the result of dry mergers between galaxies containing supermassive black holes (SMBHs). Since NSCs were found to have similar relations with their host galaxies to SMBHs (Rossa et al., 2006), it was initially thought that NSCs were the low-mass counterparts of SMBHs. It also seemed likely that if a SMBH binary formed after a merger, the transfer of energy and angular momentum from the binary would destroy the NSC (Quinlan & Hernquist, 1997; Milosavljević & Merritt, 2001). It is now clear that SMBHs and NSCs can coexist, not least in the case of the Milky Way (Schödel et al., 2009), and there is evidence that NSCs do exist in giant elliptical galaxies. Lauer et al. (2005) found nuclei in more than a third in their survey of 77 massive ellipticals, and 20% of the 40 galaxies with available colours have nuclei with similar absorption line spectra to the main galaxy (Neumayer et al., 2020).

Similarly, Dullo (2019) found "additional nuclear light components" in 3/12 galaxies with some of the largest known cores, and stated that they could be "nuclear star clusters". The surface brightness profile of one of these galaxies (NGC 6166) is shown in Figure 4.1. Although the typical central velocity dispersion (σ) of a lower mass galaxies with NSCs such as the Milky Way is relatively low at $\sim 60\,\mathrm{km\ s}^{-1}$, it is much higher in NGC 6166 ($\sim 300\,\mathrm{km\ s}^{-1}$; Bender et al., 2015). The profile also starts to rise at $\sim 120\,\mathrm{pc}$. Hence, it appears that central light excesses in giant cored elliptical galaxies exist, which could be due to atypically large NSCs with high central velocity dispersion. In this paper, we show how these could be the result of a new mechanism, which we call 'black hole (BH) dragging.'

Mergers leading to core formation can be divided into three stages (Begelman et al., 1980). First, dynamical friction of the SMBHs against stars and dark matter (DM) slows the SMBHs until they form a gravitationally bound binary (Antonini & Merritt, 2011; Valtaoja et al., 1989). Second, three-body interactions between the binary and stars (or dark matter) leads to stellar ejections and hardening of the binary (Quinlan, 1996; Sesana et al., 2006). This second phase is known as binary scouring, and its dynamical heating is both the most accepted mechanism for core formation (Quinlan, 1996) and the proposed

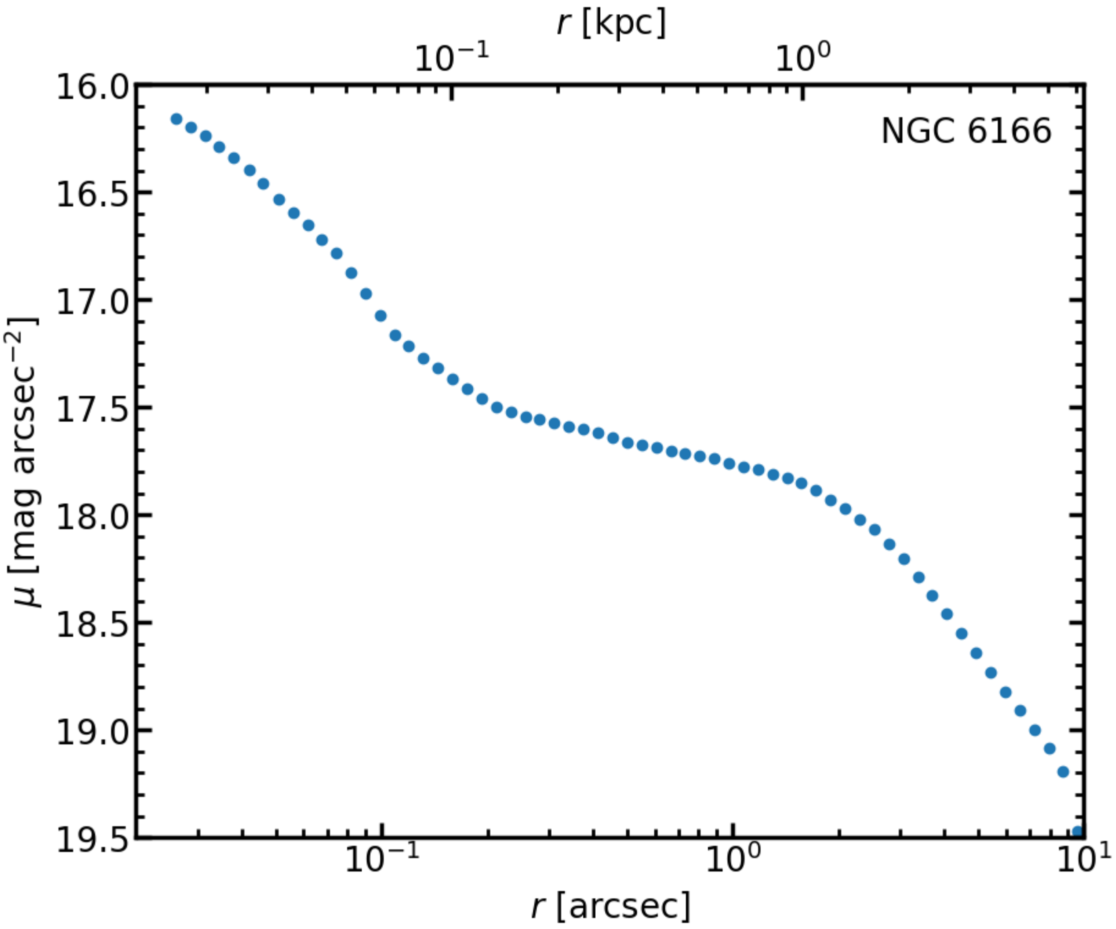

Figure 4.1: Surface brightness profile of NGC 6166. Data obtained from Dullo (2019).

cause of erasure of NSCs from high mass ellipticals (Bekki & Graham, 2010; Antonini et al., 2015). In the final merger phase, gravitational wave (GW) emission leads to inspiral and coalescence of the SMBH binary (Enoki et al., 2004; Sesana, 2013b).

At the time of SMBH coalescence, depending on their mass ratio and spins (both magnitude and orientation), asymmetric emission of GWs may occur. Since GWs carry linear momentum, the SMBH remnant receives a 'recoil kick'. Most kicks are small: for non-spinning SMBHs, Gonzalez et al. (2007) find a maximum kick speed of $v_\mathrm{k} = 175\,\mathrm{km\ s^{-1}}$, while for spinning SMBHs $v_\mathrm{k} \lesssim 600\,\mathrm{km\ s^{-1}}$ (Schnittman & Buonanno, 2007). However, certain configurations of the spins can lead to very high recoil speeds. Using numerical relativity, Campanelli et al. (2007b) show that for spins aligned and anti-aligned with the orbital angular momentum, recoil speeds of $\sim 4000\,\mathrm{km\ s^{-1}}$ can be achieved. Kicks of this size would eject the SMBH remnant from the galaxy but, after more modest kicks, the remnant and core are expected to oscillate about their common center of mass (COM) until they reach thermal equilibrium (Gualandris & Merritt, 2008).

Although most cores are relatively small at tens to a few hundreds of pc in size, a few are $> 0.5\,\mathrm{kpc}$ (Dullo, 2019). Nasim et al. (2021) performed equal mass merger simulations based on the observed parameters of A2261-BCG, followed by GW recoil kicks, and found that scouring alone produced a core size of ~ 1 kpc, but that a GW kick of $\sim 0.8\,v_\mathrm{esc}$ could reach the observed size. In addition, they found that a mild cusp was retained after scouring, but GW recoil resulted in a flat profile. We performed a similar study with a range of initial conditions, based on four galaxies from Dullo (2019) with observed core sizes ranging from 0.65-2.71 kpc, including A2261-BCG, in Khonji et al. 2024 (hereafter paper 1). In these simulations, after hardening of the SMBH binary, we merged the SMBHs and gave the remnant recoil kicks of between $0.5 - 0.9$ of the escape speed ($v_{\rm esc}$) of the galaxy remnant. We showed that binary scouring alone could form cores $< 1.3\,$kpc in size, but that GW recoil speeds of $\lesssim 0.5\,v_{\rm esc}$ are required to form cores $> 2\,$kpc. We also found that a unique signature of GW recoil heating is a truly flat core in the spatial density, which appears as core in the surface brightness. NGC 1600 was one of the galaxies which did not require recoil, which is consistent with previous modeling by Rantala et al. (2018). Recently, (Rawlings et al., 2025) studied GW recoil in a scaled-down version of this model, and found the core after scouring could be enlarged by a factor of 2-3.

In this paper, we study the effect of the likely more common smaller GW recoil kicks on the nuclei in six galaxies, four of which were those in paper 1. We examine whether the effect of recoil heating is the same, resulting in cores that are larger and flatter than after scouring alone. Somewhat unexpectedly, we find that smaller kicks can result in central cusps in surface brightness, steeper than the profiles after binary scouring. These cusps sometimes appear within a larger flattened core, and, as such, would be classified observationally as NSCs. For this reason, we refer to these central cusps throughout this paper as "NSCs". We show that NSCs formation in our simulations owes to two competing effects. Firstly, some stars become bound to the SMBH and co-move with it, an effect that is maximised at low recoil velocity. Secondly, background stars are ejected from the galaxy centre as the recoiling SMBH falls back due to dynamical friction. This effect is maximised at high recoil velocity. At intermediate recoil velocities, both effects become important and the density of bound stars can exceed that of the background stellar core. This yields a central dense NSC that forms via a new mechanism: black hole dragging.

This paper is organised as follows. The merger and GW recoil simulation methodology are described in Section 4.2. The evolution of the density profiles, core fitting, bound masses of the SMBH remnant, and density contour maps of the galaxy nuclei are in Section 3. Finally, discussion and conclusions of the formation of NSCs and cores are presented in Section 4.

4.2 Methods

To study the effects of binary scouring and GW recoil on the nuclei of giant elliptical galaxies, we performed N-body simulations of equal-mass mergers, modelled on six such galaxies selected for their large core sizes of $> 0.5\,$kpc. Five of the chosen galaxies were taken from Dullo (2019), four of which were also used in paper 1 studying the effects of GW recoil kicks with $v_{\rm k} \geq 0.5\,v_{\rm esc}$. The remaining galaxy (IC 1101) was taken from Dullo et al. (2017), and is notable for its extremely large core size of 4.2 kpc. NGC 1600 is the only galaxy in the sample with a dynamical measurement of the SMBH mass $M_\bullet$ (Thomas et al., 2016); for the other galaxies, we therefore used the relation provided by Dullo (2019) between the SMBH mass and the core radius $r_{\rm b}$, obtained by fitting a core-Sérsic profile. This combines an outer Sérsic profile (Sérsic, 1963) with an inner logarithmic slope γ. The CS profile gives intensity (I) by

$$I = I' \left[1 + \left(\frac{r_{\rm b}}{r} \right)^{\alpha} \right]^{\frac{\gamma}{\alpha}} \exp \left(- b_n \left[\frac{r^{\alpha} + r_{\rm b}^{\alpha}}{r_{\rm e}^{\alpha}} \right]^{1/\alpha n} \right) , \tag{4.1}$$

where r_b is the core radius, α is the sharpness of transition between the inner and outer parts of the profile, n is the Sérsic index, and $b_n \approx 2n - 1/3$ ensures that r_e is the effective radius of the galaxy (Sérsic, 1963). Finally, I' is defined as

$$I' = I_\mathrm{b}\, 2^{-\gamma/\alpha} \exp\left[b_n \left(\frac{2^{1/\alpha} r_\mathrm{b}}{r_\mathrm{e}} \right)^{1/n} \right] . \tag{4.2}$$

see equation 4.1) and $M_\bullet$.

The bulge masses were calculated by Dullo et al. (2017) and Dullo (2019), assuming an age of 12 Gyr, from their observed colors and metallicities, using the M_*−Luminosity relation from Worthey (1994). The relevant parameters for all six galaxies are given in Table 4.1. The setup of the galaxy models and the properties of the N-body simulations are described in paper 1, but the key elements are summarized here.

Table 4.1: Parameters of the selected galaxies.

Galaxy	Type	r_b [kpc]	γ	α	n	r_e [kpc]	$M_\bullet$ [a] $[10^{10} M_\odot]$	M_* [b] $[10^{12} M_\odot]$
NGC 1600	Isolated	0.65	0.04	2	6.3	22.8	1.70	1.51
A2147-BCG	BCG	1.28	0.14	2	6.4	31.8	2.63	1.34
NGC 6166	BCG	2.11	0.14	2	9.0	83.1	4.79	3.39
4C +74.13	BCG	2.24	0.28	2	3.7	20.9	5.13	2.39
A2261-BCG	BCG	2.71	0.00	5	2.1	17.6	6.45	4.07
IC 1101	BCG	4.2	0.08	2	5.6	11.6	11.0	1.10

[a] Black hole masses from the $M_\bullet$-r_b relation by Dullo (2019), except NGC 1600 (directly measured).

[b] Bulge mass from the M_*-L_* relation by Worthey (1994).

We simulated each galaxy as the remnant of an equal-mass merger of two identical precursor galaxies. The model parameters for the precursors are summarized in Table 4.2 and were derived from the corresponding observed values in Table 4.1. We assumed that the total stellar and SMBH masses were conserved during the respective dry galaxy and SMBH mergers, such that the precursor masses were half those of the observed galaxies. We further assumed that the precursors have Sersic profiles with index n identical to that observed for the remnants, but with half the effective radius r_e, as predicted by the virial theorem for dissipationless equal-mass merger (e.g. Binney & Tremaine, 2011; Barnes, 1992; Naab et al., 2009). Five out of six galaxies are brightest cluster galaxies (BCGs), such that their DM halos are contiguous with those of neighboring galaxies. Hence, their enclosed mass M_{200} at mean density 200 times the critical density was estimated to be $\sim 10^{14} M_\odot$, using its relation with M_* given by Correa & Schaye (2020). For NGC 1600, which is unusually isolated, we used half of the estimated mass of $\sim 15.8 \times 10^{14} M_\odot$ (Goulding et al., 2016) for the precursors.

Table 4.2: Parameters of the N-body models for the precursor galaxies.

Galaxy	$M_\bullet$ $(10^{10} M_\odot)$	M_* $(10^{12} M_\odot)$	$M_{\rm dm}$ $(10^{14} M_\odot)$	Scale Radius (kpc)	Cutoff Radius (Mpc)	n	$r_{\rm e}$ (kpc)	N_* (10^4)	$N_{\rm dm}$ (10^5)	Minimum Particle Mass $(10^6 M_\odot)$
NGC 1600	0.85	0.76	0.79	165	1.65	6.3	11.4	9.49	9.60	0.84
A2147-BCG	1.32	0.67	1.00	183	1.83	6.4	15.9	6.81	9.86	1.04
NGC 6166	2.40	1.69	1.00	183	1.83	9.0	41.7	15.34	9.02	1.17
4C +74.13	2.60	1.20	1.00	183	1.83	3.7	10.5	11.31	9.41	1.12
A2261-BCG	3.23	2.04	1.00	183	1.83	2.1	8.8	17.61	8.31	1.20
IC 1101	5.50	0.55	1.00	183	1.83	5.6	5.8	5.48	9.98	1.06

We used the AGAMA library (Vasiliev, 2019) to create equilibrium multicomponent models (SMBH, stellar bulge and DM halo). Sérsic (Sérsic, 1963) and Navarro-Frenk-White (Navarro et al., 1997) profiles were used for the bulge and halo components, respectively. For the former, AGAMA uses a deprojected profile in which the bulge mass can be used as a proxy for luminosity. Potential models of all three components and density models for bulge and halo were used to create spherical ergodic distribution functions. These were then sampled to provide the final galaxy N-body models.

The total particle number N was $\sim 10^6$, balancing resolution and resource usage. The number of bulge (N_*) and halo ($N_{\rm dm}$) particles were chosen so that the halo:bulge particle mass ratio (PMR) was ~ 10. However, central resolution was enhanced by the use of a mass refinement scheme (Attard et al., 2024), which over-samples the central particles by a factor of 10 as follows. Bulge and halo particles were each divided into four concentric zones by radius, respectively containing 1%, 11.5%, 38.5% and 49% of particles. The innermost zone was left with the full increased resolution. From the second zone outwards, particle numbers 70 are reduced, and particle masses correspondingly increased, by factors of ~ 2.53, 10 and 40, respectively, such that N is restored to the original value and the PMR is maintained in each zone.

The merger simulations were performed using the `griffin` N-body code that employs as gravity solver an adaptive fast multipole method with adjustable error (Dehnen, 2014), which we set to an average relative force error of 0.03%. Plummer-type softening was used, with a parameter of 3 pc for interactions involving the SMBHs and 30 pc for all other interactions.

The precursor galaxies were placed in a highly eccentric orbit ($e = 0.95$), mimicking those in cosmological simulations (Khochfar & Burkert, 2006; Fastidio et al., 2024), and resulting in faster orbital evolution (Gualandris et al., 2022). The initial separation was 80 kpc, providing adequate separation of the bulges.

The SMBHs were followed through the dynamical friction phase, which ends with the formation of a black hole binary (BHB) at a separation $a_{\rm f}$, defined as the separation where the mass enclosed, from the BHB COM, is equal to the mass of the BHB

$$M_* \left(r < a_{\rm f}\right) = 2\, M_\bullet \, . \tag{4.3}$$

The BHB then undergoes rapid hardening by three-body encounters with stars. Due to the triaxiality of the merger remnant (Gualandris et al., 2017; Bortolas et al., 2018b), this continues efficiently until the BHB reaches the hard binary separation

$$a_{\rm h} = \frac{G M_\bullet}{4\sigma^2} \ , \tag{4.4}$$

where σ is the stellar velocity dispersion. This corresponds to the distance at which the specific binding energy exceeds the specific kinetic energy (Milosavljević & Merritt, 2001). After BHB hardening, the N-body simulations are halted due to the high computational costs (owing to the very short time steps required to resolve the dynamics close to the BHB), and a phase of GW emission and subsequent coalescence of the BHB is assumed. To this end, the BHB in each model was replaced with a single SMBH of the same total mass and COM. The merged SMBH was then given a 'GW recoil kick', arbitrarily in the x-direction[1] with magnitude $v_{\rm k}$ equal to 0.1, 0.3 or 0.5 of the escape speed $v_{\rm esc}$ of the remnant, calculated from the combined bulge and halo potential. The N-body simulations

---

[1] We note that this choice is not exactly random as the orbital plane of the precursor orbit introduces a preferential direction. As a result, the x-direction deviates very slightly from the remnants' long axes.

were resumed with the single SMBH.

The SMBH motion following the kick can be characterized as a damped oscillator (Gualandris & Merritt, 2008) with passages in and out of the galaxy center until its velocity reaches the 'Brownian velocity' v_B, given by equipartition of kinetic energy with the stars (Smoluchowski, 1906; Merritt, 2001; Bortolas et al., 2016)

$$v_\mathrm{B}^2 = \frac{m}{M_\bullet}\sigma^2 \ , \tag{4.5}$$

where m is the mass of a stellar particle. We continued the simulations until the SMBH settles to Brownian motion. This time is clear from its maximum velocity relative to the COM of the stellar component, which shows a rapid drop to below the calculated Brownian velocity.

4.3 Results

4.3.1 Formation of the NSCs

Stellar density profiles, constructed in radial bins from individual densities estimated using an SPH-style kernel estimator (using Pynbody, Pontzen et al., 2013), are shown in Figure 4.2. These indicate that the density profiles become flattened by the time the kicked SMBH remnant reaches its first apocenter. When the SMBH returns to the nucleus at its first pericenter, the density profiles become steeper again, and remain so when the SMBH reaches Brownian motion at time t_Br. There are three possible outcomes. After the smallest GW kicks, with $v_\mathrm{k}/v_\mathrm{esc} = 0.1$, there may be little change compared to the profile after scouring, such as in IC 1101 or A2261. In other cases, and especially after larger kicks, the flattening of the profile extends further out, resulting in a prominent increased density at the nucleus after the SMBH settles. For example, this is clearly seen in NGC 1600, NGC 6166 and IC 1101 after kicks with $v_\mathrm{k}/v_\mathrm{esc} = 0.5$. We interpret these increased central densities as NSCs. In the third scenario, for example IC 1101 after kicks with $v_\mathrm{k}/v_\mathrm{esc} = 0.3$, an intermediate profile results, where the profile is more cuspy than after scouring alone, in contrast to the flat cores found after larger kicks (paper 1).

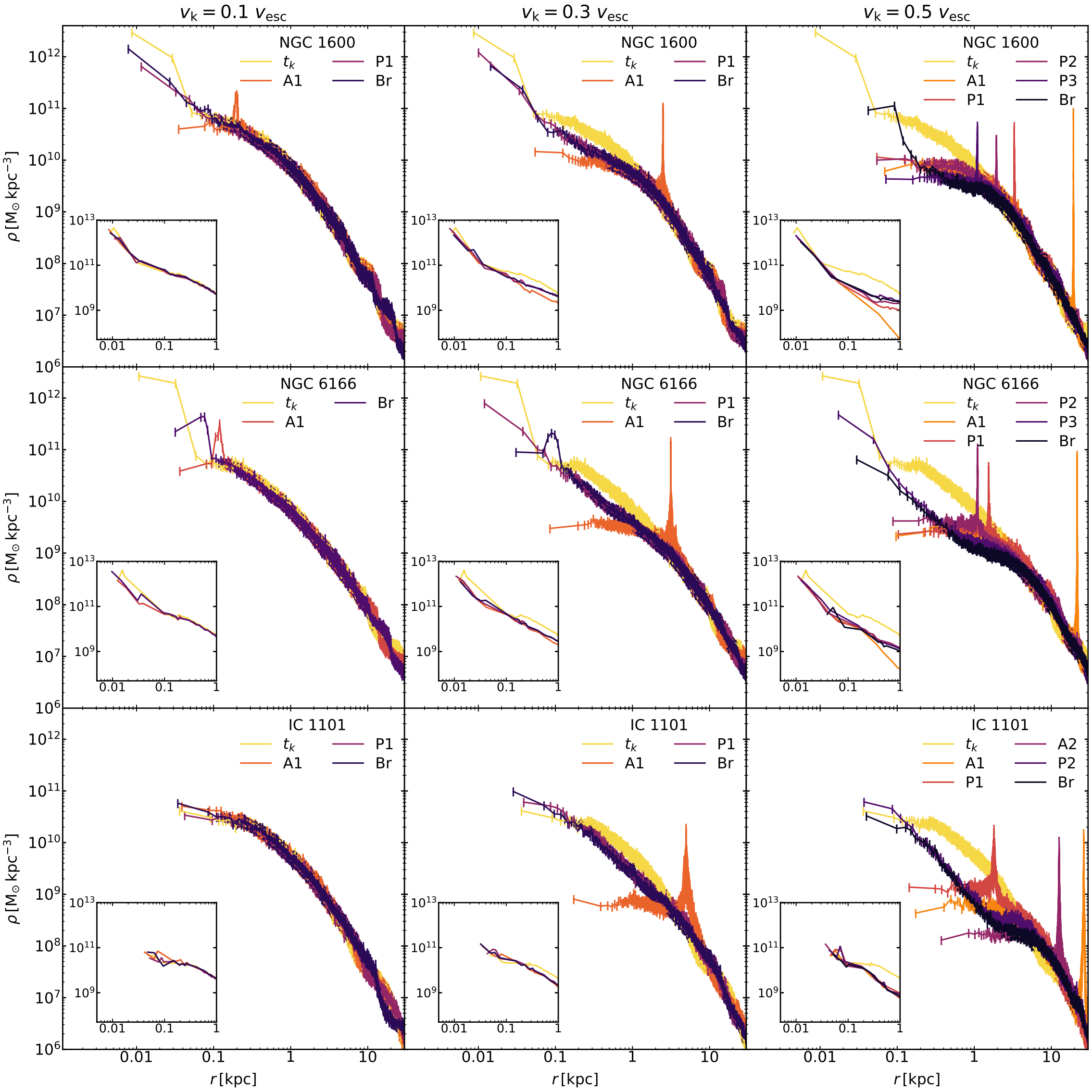

Figure 4.2: Volume density profiles, centered on the stellar COM, for the N-body merger remnant models of NGC 1600, NGC 6166 and IC 1101, using binned SPH profiles. The inset plots use spherical shells centered on the SMBH to show formation of the nucleus. Columns from left to right are for GW recoil kicks of $v_k/v_{esc} = 0.1$, 0.3 and 0.5 respectively. t_k is the time when the N-body simulation is paused for the SMBH merger and the GW recoil kick is given; 'An' and 'Pn' indicate nth apocenter and pericenter passages of the kicked SMBH; 'Br' indicates that the SMBH has settled into Brownian motion. Increases in central density are seen at 'Br' in almost all cases, with varying degrees of core formation outside them.

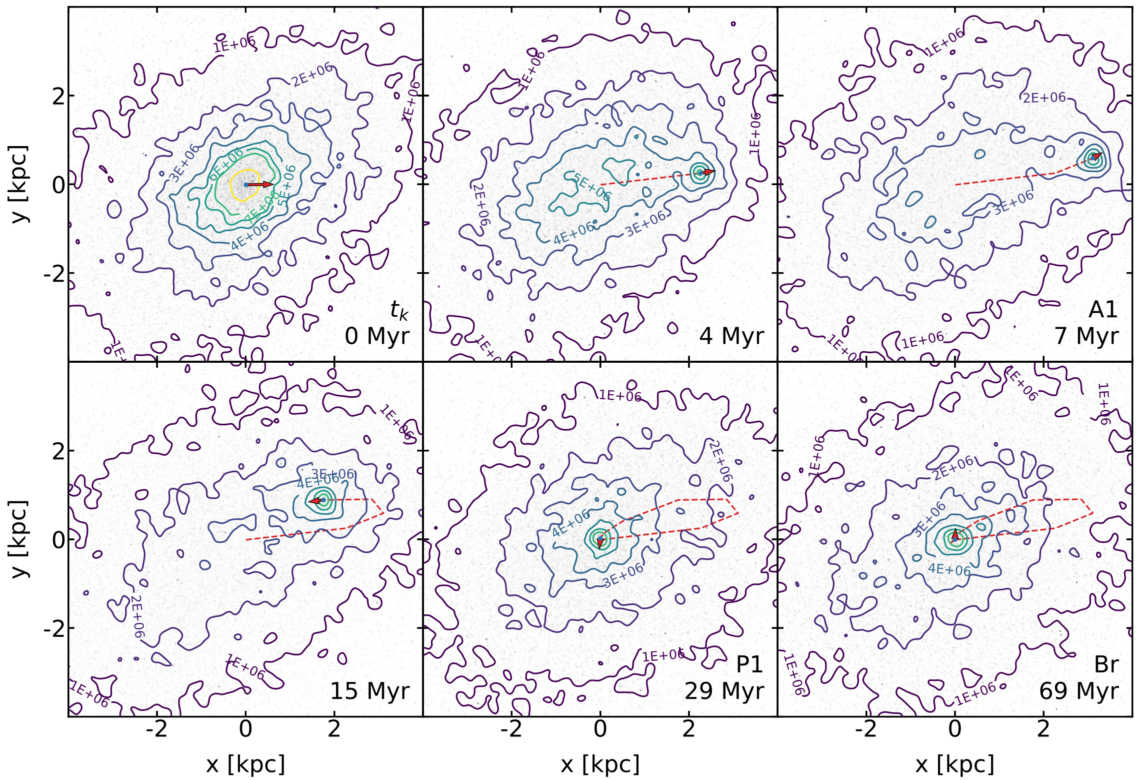

Figure 4.3: Contour plots of NGC 6166 with $v_\mathrm{k} = 0.3\,v_\mathrm{esc}$, projected along the z-axis. The blue dot is the position of the SMBH remnant, the red arrow indicates the direction and magnitude of its velocity, and the dashed red line its trajectory. The contour lines show surface densities in N-body units. ‘An’ and ‘Pn’ indicate nth apocenter and pericenter passages of the kicked SMBH; ‘Br’ indicates that the SMBH has settled into Brownian motion. Some of the denser region around the SMBH can be seen to follow it to ‘A1’, before returning with it to the center at ‘P1’, where the maximum density is less but the contour lines appear closer together.

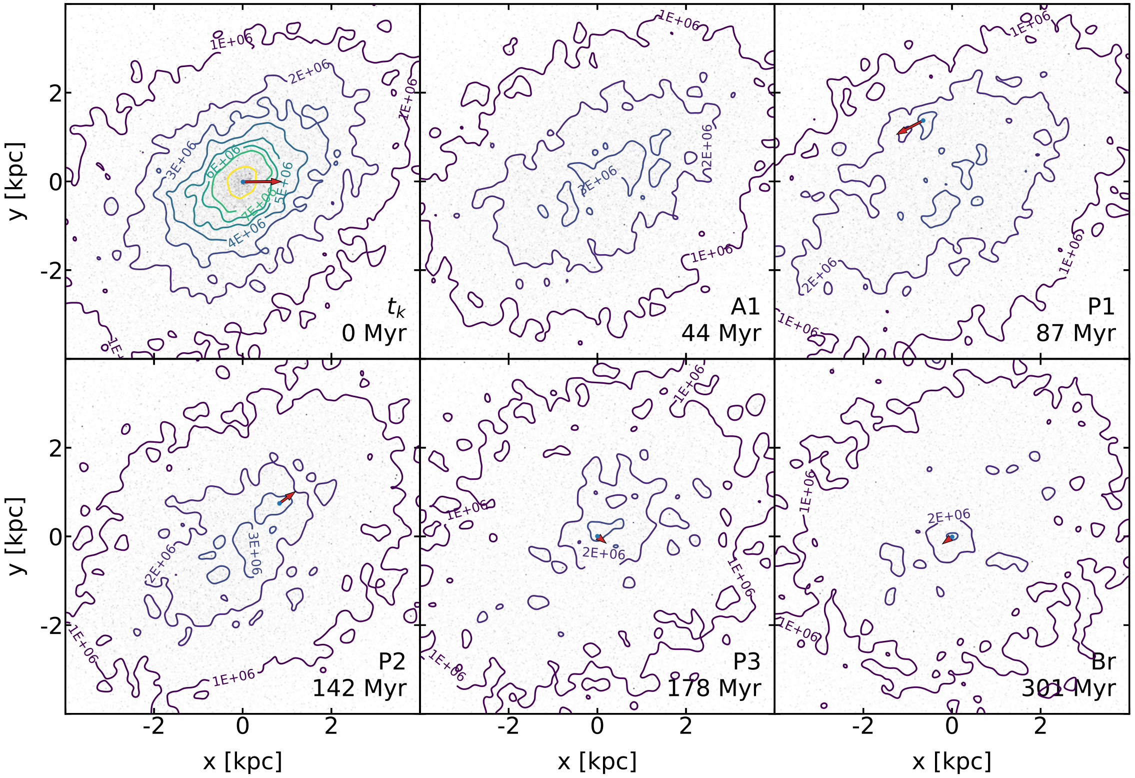

Figure 4.4: As for Figure 4.3 but for $v_\mathrm{k} = 0.5\,v_\mathrm{esc}$. The SMBH remnant leaves the area of the plot towards apocenter, hence its trajectory is not shown. An area of density is present around the SMBH after the kick, although smaller than for $v_\mathrm{k} = 0.3\,v_\mathrm{esc}$, and persists at 'Br', but here is surrounded by a flat core.

To investigate the possible formation mechanism of the NSCs, we examined the trajectories of the SMBH remnants after the GW kicks (Appendix 4.5.1). For the $v_{\rm k}/v_{\rm esc} = 0.1$ kicks, the remnant travels a relatively modest distance of $\sim 1\,{\rm kpc}$ and is quickly damped to Brownian motion. After the $v_{\rm k}/v_{\rm esc} = 0.3$ kicks, the SMBH travels further ($\sim 3-7\,{\rm kpc}$) but, in general, only reaches one apocenter before being damped at the first pericenter. The exception is IC 1101, which makes two passages. For the $v_{\rm k}/v_{\rm esc} = 0.5$ kicks, two or three passages are the norm, although A2147-BCG makes five, before Brownian motion is reached.

The combination of the trajectories and density profiles suggests the SMBHs may be bringing the stars to the nucleus. This is supported by the density contour plots (Figures 4.3 and 4.4) which show the nucleus of NGC 6166 after GW kicks with $v_{\rm k}/v_{\rm esc}$ of 0.3 and 0.5, respectively. After the $v_{\rm k}/v_{\rm esc} = 0.3$ kick, the flattening of the core as the SMBH moves away from the COM of the galaxy is evident. There is also clearly a higher density region around the SMBH, which moves out with it and returns to settle back at the center with the SMBH. Although the overall density is lower at the end of the kick, when the SMBH reaches Brownian motion, the contour lines are more closely spaced around the SMBH than at the time of the kick ($t_{\rm k}$). Similar initial flattening of the core is seen after the $v_{\rm k}/v_{\rm esc} = 0.5$ kick but the density continues to decrease and the core to enlarge with successive passages of the SMBH. In addition, the increased density around the SMBH is much less prominent. At the end of the kick an increased density around the SMBH remains, although less than that of the $v_{\rm k}/v_{\rm esc} = 0.3$ kick, but here it is surrounded by a flat core. This is likely due to the combination of the stars being dragged back to the dynamical center and heating by dynamical friction.

To confirm that the central density increase is due to this 'BH dragging' mechanism, we tagged the stars within the SMBH sphere of influence at first apocenter and then plotted their density profiles at the end of the kick, when the SMBH reached Brownian motion, separately from the remaining stars (Figure 4.5). These profiles, calculated using spherical shells, show three distinct scenarios: First, in the cases where the kick is relatively small and no increased central density is seen overall (eg. the $v_{\rm k}/v_{\rm esc}$ of 0.1 kicks and the $v_{\rm k}/v_{\rm esc}$ of 0.3 kicks for NGC 6166 and IC 1101), the tagged stars combine with the remainder to form a smooth profile; Second, for some of the largest kicks with no increased central density (eg. the $v_{\rm k}/v_{\rm esc}$ of 0.5 kick for NGC 1600), the tagged stars have a much lower density than the remainder; Finally, the most interesting cases are between these extremes (eg. the $v_{\rm k}/v_{\rm esc} = 0.3$ kick for NGC 1600 and the $v_{\rm k}/v_{\rm esc} = 0.5$ kicks for NGC 6166 and IC 1101), where the tagged stars rise steeply centrally above the flattened profile of the remainder, to form the increased nuclear density. We note that the radius of this inflection is larger than that seen in observed NSCs, but this may be due to the extremely large size of the simulated galaxies here.

The mass of stars bound to the SMBH remnant was calculated as the total mass of stars with negative total energy, that are also located within the influence radius of the SMBH ($r_{\rm i}$). The latter is defined as the radius enclosing stars with twice the mass of the SMBH. Figure 4.6 shows the bound mass for NGC 6166 with $v_{\rm k}$ from 0.1 to 0.5 of $v_{\rm esc}$ at the time of the kick and at each apocenter and pericenter following it. The higher the GW kick, the lower the bound mass at corresponding time-points. For the kicks with $v_{\rm k}/v_{\rm esc}$ of 0.1 and 0.3, the bound mass increases quickly as the motion of the SMBH remnant is damped and remains high. However, for the $v_{\rm k} = 0.5\,v_{\rm esc}$ kick, the bound mass increases as the SMBH slows to each apocenter, and then drops as the remnant increases speed towards each pericenter.

Markov chain Monte Carlo (MCMC) fitting of the surface density profiles was per-

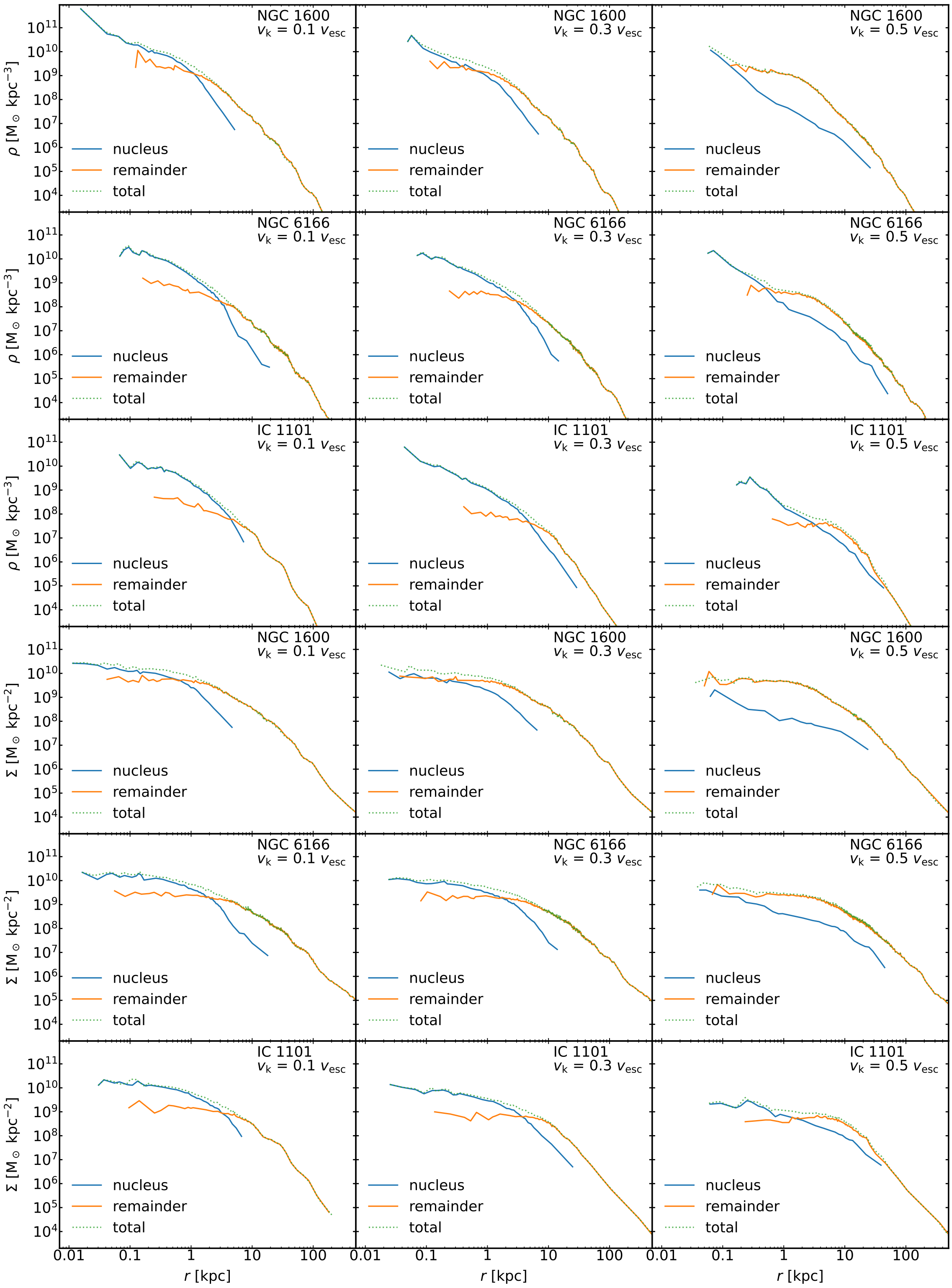

Figure 4.5: Volume (top three rows) and surface density (bottom three rows) profiles when the SMBH remnant has settled to Brownian motion for NGC 1600, NGC 6166 and IC 1101. Columns from left to right are for kicks with $v_\mathrm{k}/v_\mathrm{esc}$ of 0.1, 0.3 and 0.5 respectively. Profiles labelled 'nucleus' indicate those for particles that were within the influence radius of the SMBH at 1st apocenter (blue), and all other particles as 'remainder' (orange). The combined profiles are labeled 'total' (green dotted). The prominent increases in central density in NGC 1600 with $v_\mathrm{k} = 0.3\,v_\mathrm{esc}$, and for NGC 6166 and IC 1101 with $v_\mathrm{k} = 0.5\,v_\mathrm{esc}$ are seen to be due to the 'nucleus' particles.

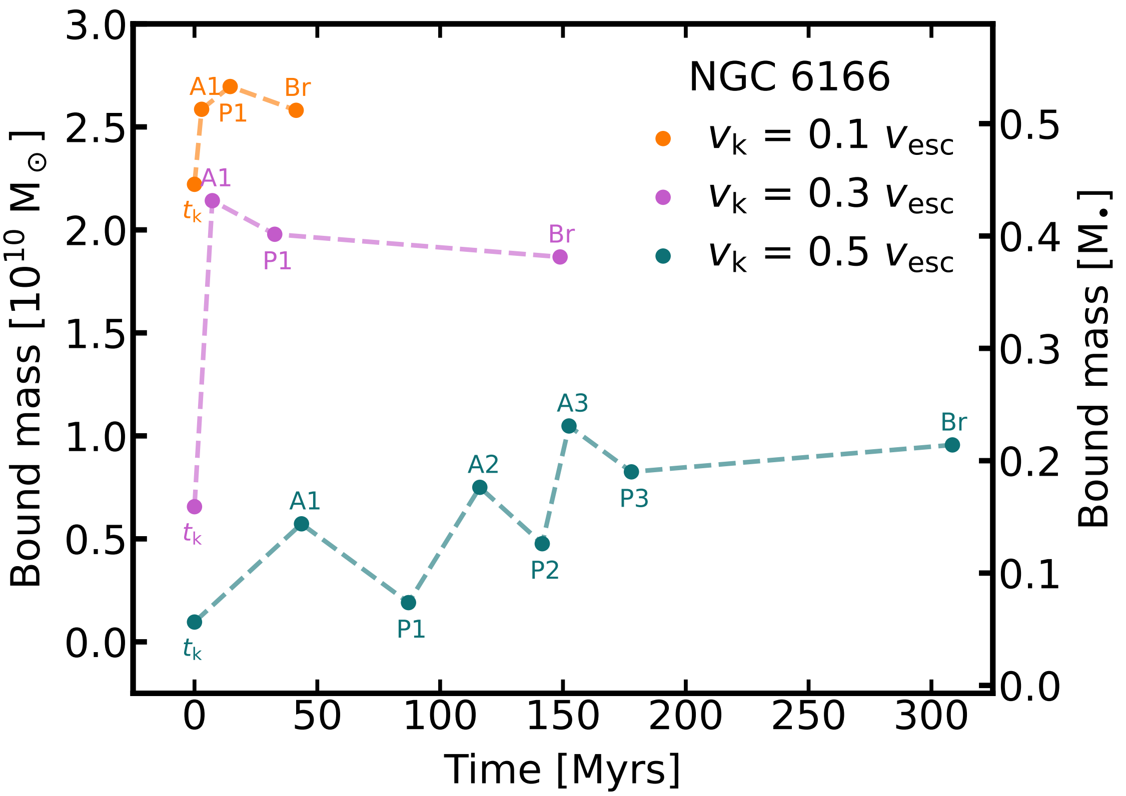

Figure 4.6: Bound mass to the SMBH remnant (here 'A' and 'P' indicate apocenter and pericenter passages, followed by the number of passages; 'Br' indicates the SMBH remnant has settled into Brownian motion) for galaxy NGC 6166 with $v_k/v_{esc} = 0.1, 0.3, 0.5$. The bound mass is lower at higher v_k/v_{esc}, for comparable phases after the kick. For the slower kicks, the bound mass quickly rises as the SMBH slows and remains high as the motion of the SMBH remnant is rapidly damped. For the $v_k/v_{esc} = 0.5$ kick, the bound mass is lower at each pericenter than the corresponding apocenter, as the SMBH speeds up and slows down.

formed as in paper 1 using the Core-Sérsic (CS) profile (Graham et al., 2003). The results of the fits, given in Table 4.3, confirm a progressive increase in r_b with increasing v_k/v_{esc}. As shown in paper 1, NGC 1600 and A2147-BCG do not require GW recoil to achieve their observed sizes, but NGC 6166 and A2261-BCG require a kick with $v_k/v_{esc} \lesssim 0.5$. For the two remaining galaxies, a GW kick with v_k/v_{esc} between 0.1 and 0.3 is required for both 4C +74.13 and IC 1101. A key finding in paper 1 was that GW kicks resulted in uniquely flat cores, especially in 3D. With the lower speed kicks in this study, we find that γ may actually increase (see Figure 4.7). This coincides with the presence of the increased nuclear density and is most promiment for $v_k/v_{esc} = 0.1$ in A2147-BCG AND NGC 6166, and for $v_k/v_{esc} = 0.3$ in NGC 6166 and IC 1101. In these cases, $\gamma \sim 0.5$, indicating the formation of a central cusp. In the cases of the $v_k/v_{esc} = 0.5$ kick for NGC 6166 and IC 1101, there are central cusps present but, due to the surrounding flat cores, they could be excluded from the fit so that the flat signature for high kicks is retained. This is not possible for the other cases described above.

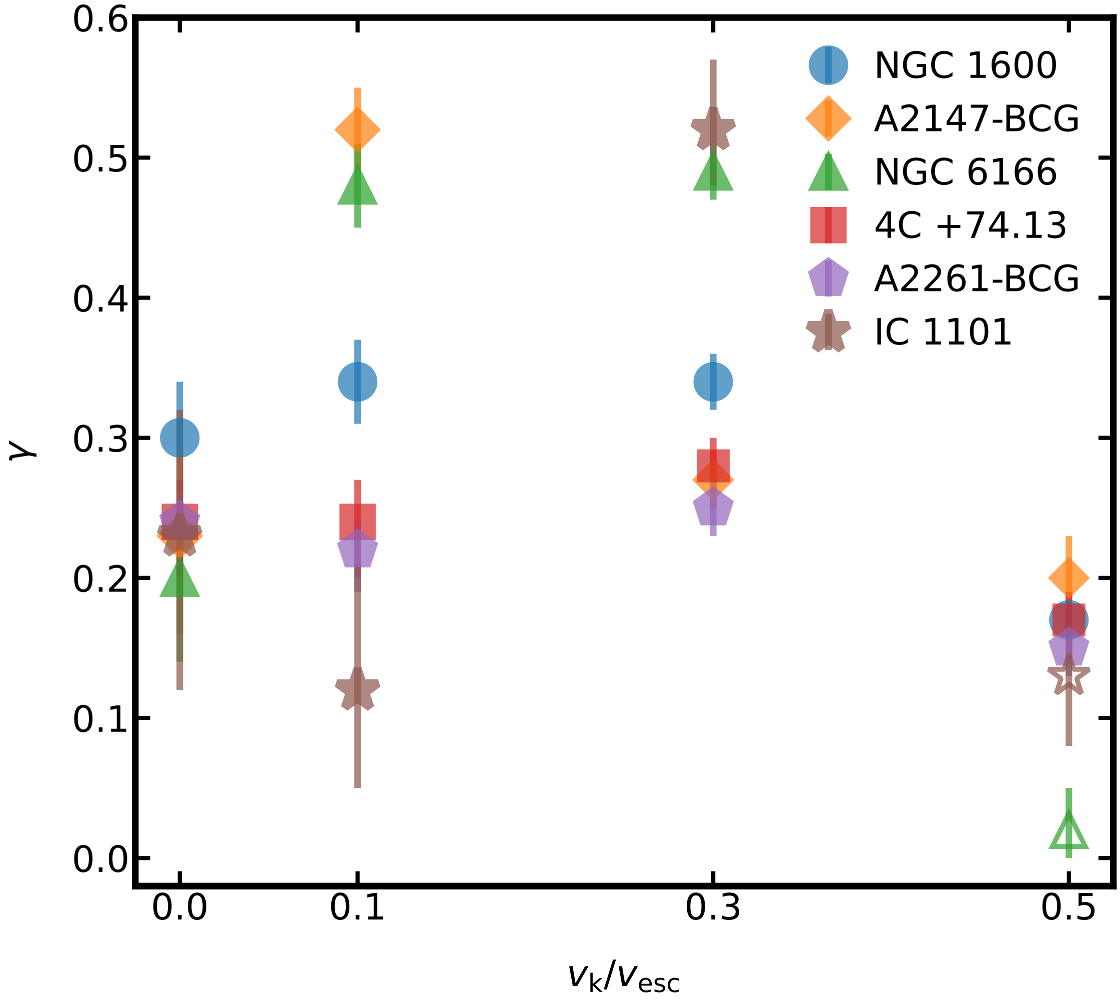

Figure 4.7: Inner logarithmic slope (γ) as a function of the ratio of kick velocity (v_{k}) to escape speed (v_{esc}) for all six galaxy remnants. A $v_{\mathrm{k}}/v_{\mathrm{esc}}$ of zero indicates scouring only. If the NSC cannot be excluded from the fit, there is a spike in γ due to its presence. Where the NSC is excluded (unfilled markers), the relation between γ and v_{esc} is restored.

Table 4.3: MCMC Core-Sérsic fits.

Galaxy	$v_\mathrm{k}/v_\mathrm{esc}$	v_k (km s^{-1})	r_b (kpc)	γ	α	n	r_e (kpc)	log ($\Sigma_\mathrm{b}/10^9\mathrm{M}_\odot\mathrm{kpc}^{-2}$)
NGC 1600	0.0	0	$0.68^{+0.04}_{-0.05}$	$0.30^{+0.04}_{-0.04}$	$3.0^{+0.5}_{-0.4}$	$6.0^{+0.1}_{-0.2}$	$22.3^{+0.4}_{-0.7}$	$23.07^{+0.05}_{-0.05}$
	0.1	309	$0.84^{+0.03}_{-0.04}$	$0.34^{+0.03}_{-0.03}$	$4.7^{+0.7}_{-0.5}$	$6.29^{+0.01}_{-0.01}$	$22.35^{+0.09}_{-0.04}$	$22.81^{+0.04}_{-0.03}$
	0.3	929	$1.30^{+0.03}_{-0.03}$	$0.34^{+0.02}_{-0.02}$	$17.3^{+30.7}_{-6.3}$	$6.29^{+0.01}_{-0.01}$	$22.35^{+0.08}_{-0.04}$	$22.37^{+0.02}_{-0.02}$
	0.5	1548	$1.75^{+0.03}_{-0.04}$	$0.17^{+0.02}_{-0.02}$	$7.8^{+1.1}_{-0.9}$	$6.29^{+0.01}_{-0.02}$	$22.4^{+0.1}_{-0.1}$	$21.92^{+0.02}_{-0.02}$
A2147-BCG	0.0	0	$1.32^{+0.15}_{-0.16}$	$0.23^{+0.06}_{-0.07}$	$1.4^{+0.2}_{-0.1}$	$6.3^{+0.1}_{-0.1}$	$24.7^{+2.5}_{-1.4}$	$21.95^{+0.10}_{-0.09}$
	0.1	323	$2.29^{+0.03}_{-0.04}$	$0.52^{+0.03}_{-0.03}$	$2.8^{+0.3}_{-0.3}$	$6.33^{+0.05}_{-0.08}$	$23.3^{+0.8}_{-0.4}$	$21.27^{+0.05}_{-0.05}$
	0.3	971	$2.91^{+0.07}_{-0.06}$	$0.27^{+0.02}_{-0.02}$	$5.7^{+0.7}_{-0.6}$	$6.34^{+0.04}_{-0.07}$	$23.2^{+0.6}_{-0.3}$	$21.07^{+0.02}_{-0.02}$
	0.5	1619	$3.65^{+0.01}_{-0.10}$	$0.20^{+0.03}_{-0.03}$	$4.7^{+0.6}_{-0.5}$	$6.3^{+0.1}_{-0.1}$	$24.6^{+2.5}_{-1.4}$	$20.47^{+0.02}_{-0.02}$
NGC 6166	0.0	0	$0.90^{+0.09}_{-0.09}$	$0.20^{+0.05}_{-0.06}$	$1.15^{+0.05}_{-0.05}$	$9.0^{+0.1}_{-0.1}$	$60.1^{+0.2}_{-0.1}$	$22.79^{+0.08}_{-0.08}$
	0.1	331	$1.12^{+0.05}_{-0.05}$	$0.48^{+0.03}_{-0.03}$	$4.8^{+0.7}_{-0.6}$	$9.08^{+0.01}_{-0.03}$	$60.3^{+0.6}_{-0.3}$	$22.42^{+0.04}_{-0.04}$
	0.3	994	$1.83^{+0.04}_{-0.04}$	$0.49^{+0.02}_{-0.02}$	$8.9^{+1.9}_{-1.2}$	$9.09^{+0.01}_{-0.01}$	$60.1^{+0.2}_{-0.1}$	$21.74^{+0.02}_{-0.02}$
	0.5	1657	$2.98^{+0.05}_{-0.04}$	$0.02^{+0.03}_{-0.02}$	$6.9^{+0.6}_{-0.5}$	$9.07^{+0.02}_{-0.05}$	$60.5^{+0.8}_{-0.4}$	$21.09^{+0.01}_{-0.01}$

Table 4.3 Continued from previous page

Galaxy	$v_\mathrm{k}/v_\mathrm{esc}$	v_k (km s^{-1})	r_b (kpc)	γ	α	n	r_e (kpc)	log ($\Sigma_\mathrm{b}/10^9\mathrm{M}_\odot\mathrm{kpc}^{-2}$)
4C +74.13	0.0	0	$1.22^{+0.06}_{-0.06}$	$0.24^{+0.03}_{-0.04}$	$5.0^{+0.9}_{-0.6}$	$3.89^{+0.01}_{-0.02}$	$16.9^{+0.1}_{-0.1}$	$22.40^{+0.03}_{-0.03}$
	0.1	339	$1.22^{+0.06}_{-0.06}$	$0.24^{+0.03}_{-0.04}$	$5.0^{+0.9}_{-0.6}$	$3.89^{+0.01}_{-0.02}$	$16.9^{+0.1}_{-0.1}$	$22.40^{+0.03}_{-0.03}$
	0.3	1019	$2.53^{+0.06}_{-0.06}$	$0.28^{+0.02}_{-0.02}$	$6.3^{+1.0}_{-0.7}$	$3.87^{+0.02}_{-0.05}$	$17.0^{+0.2}_{-0.1}$	$21.62^{+0.02}_{-0.02}$
	0.5	1698	$3.54^{+0.08}_{-0.08}$	$0.17^{+0.02}_{-0.02}$	$5.2^{+0.6}_{-0.5}$	$3.83^{+0.05}_{-0.08}$	$17.2^{+0.6}_{-0.3}$	$21.10^{+0.02}_{-0.02}$
A2261-BCG	0.0	0	$1.32^{+0.04}_{-0.05}$	$0.24^{+0.02}_{-0.02}$	$62.4^{+25.8}_{-28.7}$	$2.15^{+0.02}_{-0.02}$	$13.1^{+0.1}_{-0.1}$	$22.98^{+0.02}_{-0.02}$
	0.1	356	$0.96^{+0.05}_{-0.05}$	$0.22^{+0.02}_{-0.03}$	$52.9^{+32.0}_{-31.6}$	$2.199^{+0.001}_{-0.001}$	$12.905^{+0.008}_{-0.004}$	$22.79^{+0.03}_{-0.03}$
	0.3	1070	$2.08^{+0.05}_{-0.06}$	$0.25^{+0.02}_{-0.02}$	$32.9^{+40.9}_{-17.2}$	$2.08^{+0.05}_{-0.06}$	$12.91^{+0.02}_{-0.01}$	$22.20^{+0.02}_{-0.02}$
	0.5	1784	$2.65^{+0.06}_{-0.07}$	$0.15^{+0.02}_{-0.02}$	$8.8^{+2.0}_{-1.3}$	$2.19^{+0.01}_{-0.01}$	$12.93^{+0.05}_{-0.03}$	$21.90^{+0.02}_{-0.02}$
IC 1101	0.0	0	$0.61^{+0.07}_{-0.07}$	$0.23^{+0.09}_{-0.11}$	$3.1^{+1.0}_{-0.7}$	$5.2^{+0.2}_{-0.1}$	$11.7^{+0.2}_{-0.3}$	$22.55^{+0.09}_{-0.08}$
	0.1	318	$0.63^{+0.12}_{-0.10}$	$0.12^{+0.09}_{-0.07}$	$1.1^{+0.1}_{-0.1}$	$5.4^{+0.4}_{-0.3}$	$11.6^{+0.3}_{-0.4}$	$22.46^{+0.11}_{-0.14}$
	0.3	956	$4.78^{+0.36}_{-0.34}$	$0.52^{+0.05}_{-0.04}$	$1.2^{+0.2}_{-0.1}$	$5.5^{+0.3}_{-0.4}$	$11.5^{+0.3}_{-0.4}$	$20.00^{+0.09}_{-0.09}$
	0.5	1594	$6.54^{+0.16}_{-0.16}$	$0.13^{+0.05}_{-0.05}$	$4.8^{+0.8}_{-0.7}$	$5.5^{+0.3}_{-0.3}$	$11.5^{+0.3}_{-0.3}$	$19.12^{+0.03}_{-0.03}$

Note: The fits were performed on surface density profiles at the time the SMBH reaches Brownian motion.

4.3.2 Properties of the NSCs

Properties of the NSCs are shown in Table 4.4. Here, we analyse the clusters of stars bound to the MBH, but we return to the question whether these constitute NSCs in the observational sense in Section 4.4. We take the stellar mass bound to the SMBH remnant (M_b) at t_Br to be the mass of the NSC (M_N). A characteristic length is given by r_k, the theoretical linear extent of a bound cluster to an ejected SMBH (Merritt et al., 2009), given by

$$r_\mathrm{k} = \frac{GM_\bullet}{v_\mathrm{k}^2}\,, \tag{4.6}$$

which can be compared with the radius of influence of the SMBH at the time of the kick and the late time of settling to Brownian motion. The cluster mass M_N decreases with increasing v_k for all six galaxies. However, it is higher in the two galaxies with the most prominent NSCs. In the case of IC 1101, there is an order of magnitude difference between its value of M_N and that of NGC 1600. For NGC 6166, M_N is higher than in all four remaining galaxies. The ratio of M_N to $M_\bullet$ seems to be a particularly good measure of the likelihood of an NSC (Figure 4.8). It is highest in the galaxies whose density profiles indicate the most prominent NSCs, such as IC 1101 and NGC 6166, and lowest in A2261, which shows the least evidence of an NSC.

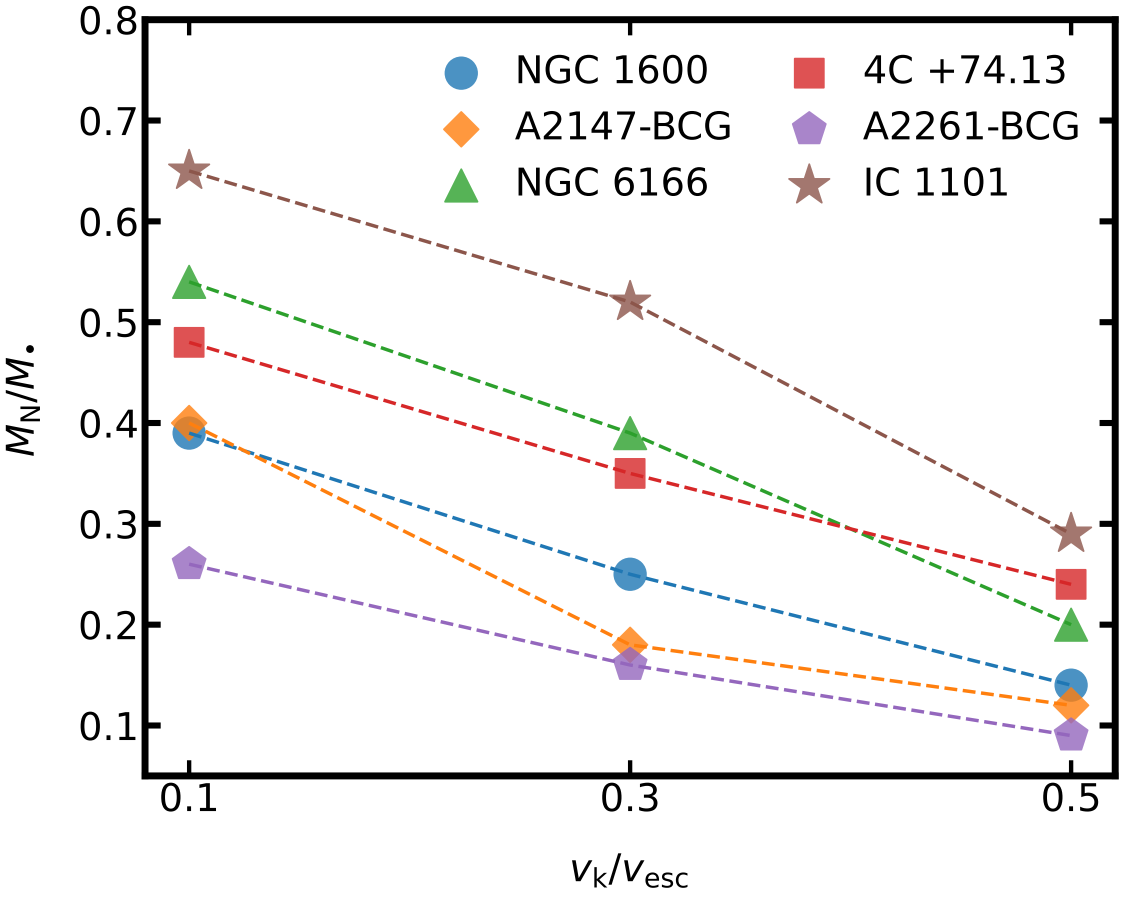

Figure 4.8: NSC mass (M_N) as a proportion of SMBH mass ($M_\bullet$) for each ratio $v_\mathrm{k}/v_\mathrm{esc}$ of kick to escape speed, for all six galaxy remnants. $M_\mathrm{N}/M_\bullet$ decreases with increasing $v_\mathrm{k}/v_\mathrm{esc}$. It is largest in galaxies with the most prominent NSCs and smallest in A2261, which has the least prominent NSC.

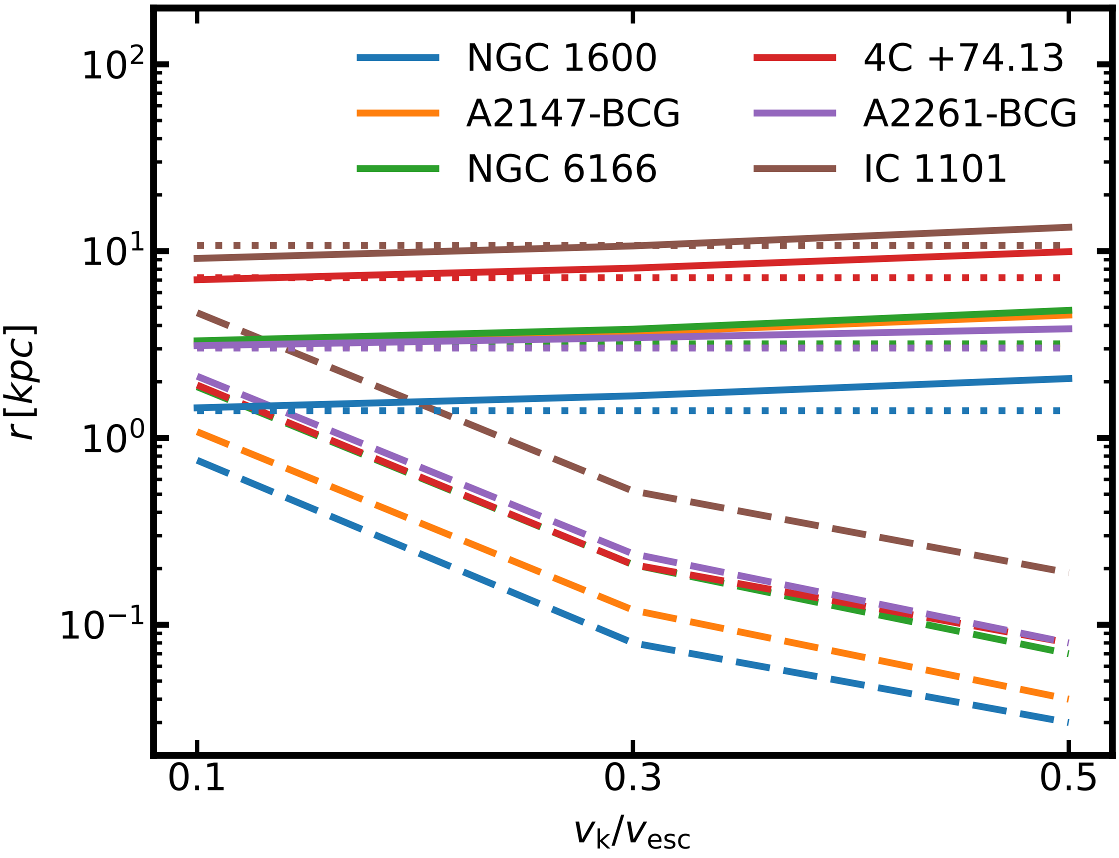

Figure 4.9: NSC radius as a function of the ratio $v_\mathrm{k}/v_\mathrm{esc}$ of kick to escape speed for all six galaxy remnants. The radius of influence of the SMBH remnant the time of the kick ($r_\mathrm{i}(t_\mathrm{k})$; dotted lines) is lower than when the SMBH is in Brownian motion ($r_\mathrm{i}(t_\mathrm{Br})$; solid lines). While the latter increases with $v_\mathrm{k}/v_\mathrm{esc}$, the value of r_k (dashed lines) decreases markedly.

Table 4.4: NSC properties

Galaxy	$v_\mathrm{k}/v_\mathrm{esc}$	r_k (kpc)	$r_\mathrm{i}(t_\mathrm{k})$ (kpc)	$r_\mathrm{i}(t_\mathrm{Br})$ (kpc)	$M_\mathrm{b}(t_\mathrm{k})$ $(\mathbf{10^{10}M_\odot})$	M_N $(\mathbf{10^{10}M_\odot})$	$M_\mathrm{N}/M_\bullet$	$\sigma_\mathrm{N}(t_\mathrm{Br})$ (km s^{-1})	N_N	f_hr
NGC 1600	0.1	0.76	1.40	1.45	0.59	0.70	0.39	725	4412	0.98
	0.3	0.08	1.40	1.68	0.15	0.42	0.25	747	2441	0.96
	0.5	0.03	1.40	2.08	0.01	0.24	0.14	763	1311	0.94
A2147-BCG	0.1	1.08	3.09	3.19	0.85	1.06	0.40	616	5180	0.96
	0.3	0.12	3.09	3.67	0.15	0.48	0.18	685	2089	0.93
	0.5	0.04	3.09	4.55	0.01	0.32	0.12	729	1252	0.88
NGC 6166	0.1	1.88	3.19	3.31	2.22	2.58	0.54	812	11636	0.99
	0.3	0.21	3.19	3.82	0.66	1.87	0.39	790	8070	0.98
	0.5	0.07	3.19	4.82	0.10	0.96	0.20	836	3792	0.95
4C +74.13	0.1	1.92	7.21	7.03	1.91	2.48	0.48	769	8454	0.96
	0.3	0.21	7.21	8.11	0.49	1.81	0.35	757	5794	0.95
	0.5	0.08	7.21	9.94	0.05	1.25	0.24	768	3633	0.93
A2261-BCG	0.1	2.14	3.03	3.12	1.54	1.65	0.26	988	6497	0.94
	0.3	0.24	3.03	3.44	0.68	1.06	0.16	1028	3601	0.89
	0.5	0.08	3.03	3.84	0.12	0.58	0.09	1141	1768	0.85
IC 1101	0.1	4.68	10.72	9.14	6.18	7.15	0.65	800	16710	0.77
	0.3	0.52	10.72	10.66	1.65	5.68	0.52	734	12457	0.75
	0.5	0.19	10.72	13.42	0.30	3.14	0.29	741	5949	0.68

At time t_{k}, for $v_{\mathrm{k}}/v_{\mathrm{esc}} = 0.1$, r_{i} is higher than r_{k} by up to a factor of four, and highest in IC 1101, which has the most massive SMBH (Figure 4.9). However, the value of r_{i} in 4C +74.13 is two to three times higher than that of A2261-BCG, despite a higher SMBH mass in the latter. Of course, r_{k} must drop as the inverse square of v_{k}. But at time t_{Br}, we find that r_{i} increases with v_{k}. The difference to r_{k} is expected due to the damped motion of the SMBH at the end of the kick, and the increase with v_{k} is explained by the fall in core density at t_{Br} with increasing v_{k}.

4.3.3 Relaxation Time

To ensure the above results are not affected by relaxation, we estimate the relaxation time using

$$t_{\mathrm{relax}} = 0.34 \frac{\sigma_{\mathrm{N}}^3}{G^2 m \rho \ln \Lambda} \tag{4.7}$$

(Binney & Tremaine, 2011), where σ_{N} is the mean stellar velocity dispersion in the nuclear cluster, ρ is its density and $\ln \Lambda$ is the Coulomb logarithm, where

$$\Lambda = \frac{b_{\mathrm{max}} v_{\mathrm{typ}}^2}{2Gm} . \tag{4.8}$$

Here, b_{max} is the maximum impact parameter and v_{typ} is the typical velocity of the cluster stars. This gives $t_{\mathrm{relax}} \approx 15$ Gyr at a radius of 1 kpc, far greater than the maximum time for the SMBH to settle into Brownian motion of 0.6 Gyr.

4.4 Discussion and Conclusions

We have studied the effect of relatively small GW recoil kicks following equal mass mergers and binary scouring to form some of the largest elliptical galaxies. We unexpectedly find that, unlike the flat cores which are a signature of GW recoil heating by larger kicks paper 1, the higher bound mass to the SMBH (M_{b}) typical of smaller kicks results in stars being pulled along with the SMBH remnant, a process we call ‘BH dragging.’

The total mass of stars with negative total energy, that are also located within the influence radius of the SMBH, which we denote with M_{b}, increases with decreasing kick speed (v_{k}) at the time of the kick (t_{k}), at the first apocenter and pericenter, and at the time the SMBH reaches Brownian motion (t_{Br}, Figure 4.6). Furthermore, for each kick, M_{b} increases between t_{k} and first apocenter, and remains higher than at t_{k}, showing how the NSC builds mass.

The final result depends on both the kick velocity and the galactic environment. Although the SMBH remnants have the highest bound mass for the smallest kicks studied, with $v_{\mathrm{k}}/v_{\mathrm{esc}} = 0.1$, there may be little change in the profile, as the SMBH moves only a small distance ($\lesssim 1$ kpc) and is quickly damped, so heating is minimal. For the kicks with a v_{k} of 0.3 or 0.5 of v_{esc}, there is usually a reduction in overall density further out due to the greater distance traveled by the SMBH. The combination of the stars being dragged back to the dynamical center and heating by dynamical friction results in the nuclear density being visible and distinct from the remainder of the stellar bulge. However, there is a possible intermediate scenario, where the heating is not as effective, but the BH dragging still occurs, which can result in a cuspy profile, with a higher γ than before the kick.

We have shown that the simulation profiles can be decomposed into the stars that were bound to the SMBH remnant at first apocenter and the remainder, and that it is the former which can cause the prominent central nuclear density. This is clear evidence that the BH dragging mechanism is real, and the decomposition is straightforward to implement in simulations. However, this is obviously not possible in the case of observed surface brightness profiles. Where the nucleus is distinct, we understand that observers would fit this separately, often using a Sérsic profile. Hence it was sensible and practicable to exclude the central density when fitting the Core-Sérsic profile here. However, neither method would be possible in the case of the cuspy profiles and so it is likely these galaxies would be classed as cusp rather than core galaxies. The increased cuspiness also leads to the possibility that galaxies after a small GW recoil would be classified as cusp rather than core galaxies.

It is open to debate whether or not the nuclear densities should be called NSCs. If one considers these to be only those in disc galaxies with effective radii of 1-9 pc and velocity dispersions of $\sim 20\,\mathrm{km\ s^{-1}}$ (Böker et al., 2002, 2004) or stellar nuclei of ~ 4 pc in dwarf ellipticals (Geha et al., 2002), then clearly those in this paper are 1-2 orders of magnitude larger. Similarly, we find M_{N} to be $\sim 10^{10}\mathrm{M}_{\odot}$, compared to observed masses of up to $\sim 10^{8}\mathrm{M}_{\odot}$ (e.g. Böker et al., 2004; Côté et al., 2006). In spiral galaxies, stellar discs have increased central brightness with similar radii to our simulations at ~ 500 pc and are called central excesses of light (Boker et al., 2003) or pseudobulges (Kormendy & Kennicutt Jr, 2004), but are cold and rotating. In elliptical galaxies, Lauer et al. (2005) finds the surface brightness profiles often have a point of inflection at $\sim$ 10-40 pc and calls these nuclei, stating that they could either be clusters or active galactic nuclei. Although the nuclei in this simulation are much larger, they are in particularly massive galaxies, with high central velocity dispersions. Since NSC masses are known to scale with both of these parameters (e.g. Carollo et al., 1997; Ferrarese et al., 2006) this could explain our high values of M_{N}. Hence, BH dragging in smaller galaxies could result in such smaller, less massive nuclei.

It is also possible that improved multiwavelength observations may allow detection of more massive nuclei in the most massive galaxies. For example, Dullo et al. (2024) finds hybrid nuclei with an NSC and AGN are three times more frequent than previously observed (e.g. Seth et al., 2008) in galaxies with stellar masses of $10^{10.6}$-$10^{11.8}$ $\mathrm{M}_{\odot}$, and finds NSC masses of up to $10^{9.8}$. Observational mass estimation is also not straightforward and different methods may be used, but they are predominantly photometric, by 1D or 2D decomposition of the surface brightness profile, using multiple components, and conversion of luminosities into mass using colors and stellar population mass-to-light ratios (e.g. Georgiev et al., 2016; Dullo et al., 2024).

A broader question is whether NSCs even exist in larger elliptical galaxies. Côté et al. (2006) found no nucleation in galaxies brighter than $\sim M_B$ -20.5, and suggest that any nuclei are erased by subsequent mergers or core formation. However, Lauer et al. (2005) find increased central densities in 29% of elliptical galaxies and Dullo et al. (2024) find nuclei in 10-20 % of core galaxies but 76 % of cusp galaxies. It is interesting to note that BH dragging occurs after the merger and core formation so these processes would not erase the nucleus unless a subsequent merger occurs, and that it results in a more cuspy profile. Furthermore, we calculate the relaxation time for these large galaxies to all be $>$ 10 Gyr, so that they will persist, although the massive SMBHs are likely to be fed by tidal disruption events. Detection of such clusters in giant elliptical galaxies could be used as a probe of low velocity recoil kicks. We will examine this in future work.

Finally, metallicity acts as an important differentiator between NSC formation mechanisms. Nuclei formed by infall of GCs should have lower metallicities than the remainder of the galaxy, whereas they should be higher in those from in situ star formation. BH dragging in gas-poor ellipticals would be expected to have the same metallicity as the central stars. Neumayer et al. (2020) find that nuclei in elliptical galaxies above $10^9 M_\odot$ generally have higher metallicities than their hosts, especially in spectroscopic observations, such that they favor in-situ star formation over GC infall in such massive ellipticals. Although we agree the data suggests formation by GC infall is less likely, the metallicity of galaxies has a general tendency to rise towards their centers (Fahrion et al., 2021), so that NSCs formed by BH dragging would be expected to have higher metallicities than the remainder of the galaxy. Clearly our simulations assume that these galaxies have so little gas that hydrodynamic simulations are unnecessary, but it may be interesting to examine the effect of adding a small density of gas in further work.

4.5 Appendices

4.5.1 Trajectories of the SMBH remnant

Figure 4.10 shows the trajectory of the SMBH remnant after the GW recoil kicks. It generally makes only 1-2 passages before being quickly damped to Brownian motion.

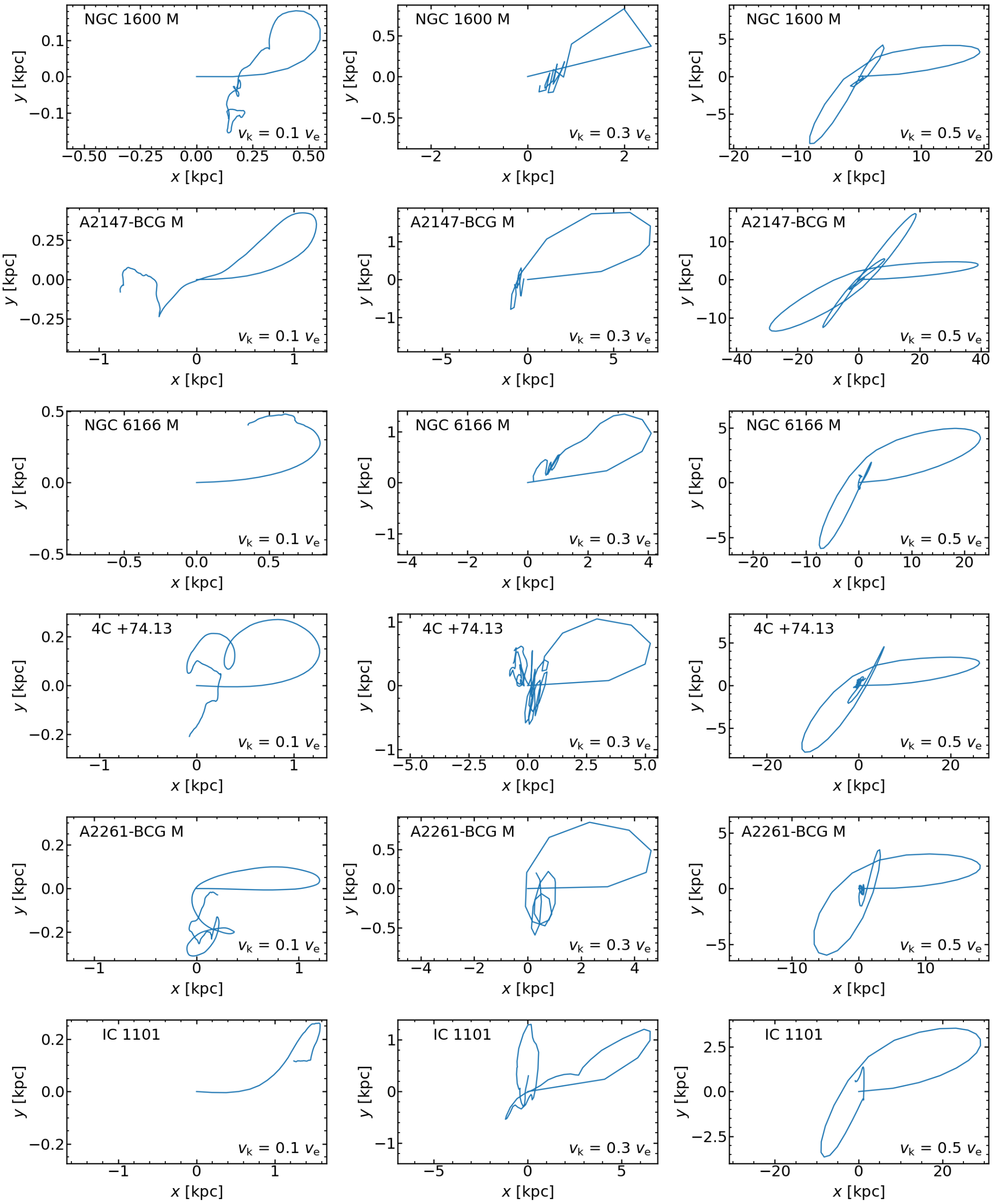

Figure 4.10: Trajectory of the SMBH remnant (recentered on the COM) from the time the GW kick recoil is applied. Rows (from top to bottom) correspond to galaxies NGC 1600, A2147 BCG, NGC 6166, 4C +74.13, A2261-BCG, IC 1101, respectively. Columns (from left to right) show results for v_k/v_{esc} of 0.1, 0.3 and 0.5, respectively. In contrast to the higher speed kicks in paper 1, the SMBH in general makes just one or two passages through the nucleus before being damped to Brownian motion.

4.5.2 Density profiles for A2147-BCG, 4C +74.13, and A2261-BCG

Figure 4.11 shows the volume density profiles for A2147-BCG, 4C +74.13, and A2261-BCG using binned SPH profiles. Figure 4.12 shows their volume and surface density profiles, divided into that for the NSC particles, and the remainder.

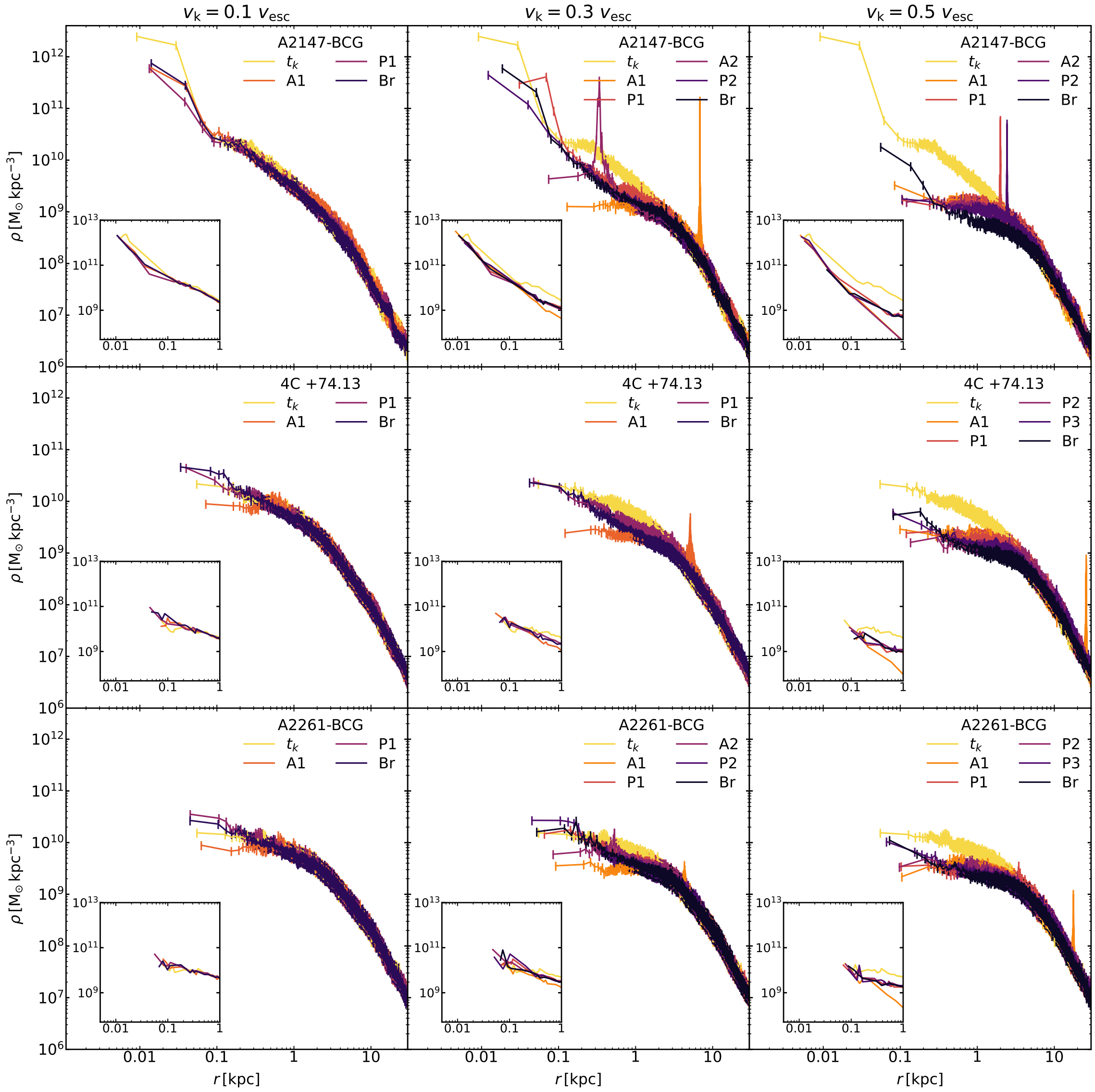

Figure 4.11: Volume density profiles, centered on the stellar COM, for the N-body merger remnant models of A2147-BCG, 4c +74.13 and A2261-BCG, using binned SPH profiles. The inset plots use spherical shells centered on the SMBH to show formation of the nucleus. Columns from left to right are for GW recoil kicks of $v_{\mathrm{k}}/v_{\mathrm{esc}} = 0.1$, 0.3 and 0.5 respectively. t_{k} is the time when the N-body simulation is paused for the SMBH merger and the GW recoil kick is given; 'An' and 'Pn' indicate nth apocenter and pericenter passages of the kicked SMBH; 'Br' indicates that the SMBH has settled into Brownian motion. Increases in central density are seen at 'Br' in almost all cases, with varying degrees of core formation outside them.

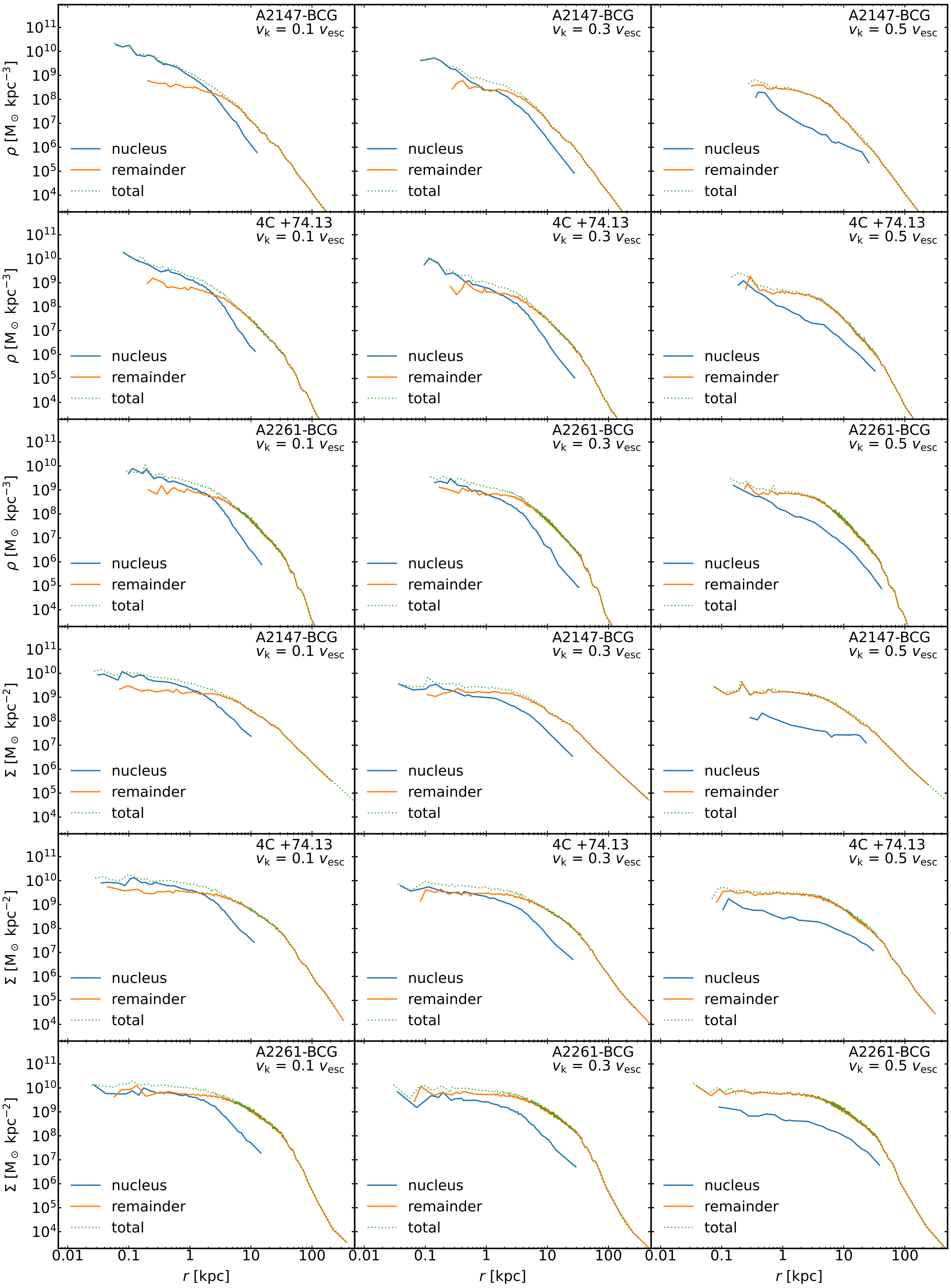

Figure 4.12: Volume (top three rows) and surface density (bottom three rows) profiles when the SMBH remnant has settled to Brownian motion for A2147-BCG, 4C +74.13, and A2261-BCG. Columns from left to right are for kicks with v_k/v_{esc} of 0.1, 0.3 and 0.5 respectively. Profiles labelled 'nucleus' indicate those for particles that were within the influence radius of the SMBH at 1st apocenter (blue), and all other particles as 'remainder' (orange). The combined profiles are labeled 'total' (green dotted).

Chapter 5

Prediction of Gravitational Wave Recoil in Giant Elliptical Galaxies

In this chapter, I re-analyse literature data for the surface brightness profiles of 24 bright elliptical galaxies with core size > 0.5 kpc. This creates the first self-consistent dataset for this group of galaxies, free from variations arising from the use of different models or fitting procedures. This lays the foundations for using these data to directly constrain the velocity distribution function of black hole kicks.

5.1 Introduction

The preceding two chapters examined the effects of GW recoil on the nuclei of elliptical galaxies. We found that higher speed recoil kicks lead to large, flat cores, but that smaller kicks may lead to a central excess of light, which may form a nuclear star cluster, often within a flatter core. We would next like to investigate whether this knowledge can be applied to observations of giant elliptical galaxies, to determine the likelihood they have undergone a recoil kick. In those galaxies which probably experienced a kick, can the likely speed of the kick be predicted? Given the preceding results, we may be able to do so using the observed core size and flatness.

The light profiles of elliptical galaxies are generally obtained by analysis of Hubble Space Telescope images, and consist of surface brightness in magnitudes against radius in arcseconds. The profiles are fitted to models by the observers, of which two are in common use: the five-parameter Nuker profile (Equation 1.5, Lauer et al., 1995) and the six-parameter core-Sérsic profile (Equation 1.6, Graham et al., 2003). In addition, each observer uses their own fitting procedure. Although both models have the most important two parameters in common, the core size r_{b} and flatness γ, there is clearly the risk that these will vary for a given surface brightness profile, depending on the model and fitting algorithm used. Indeed, Graham et al. (2003) showed that the value of r_{b} obtained with the Nuker profile depends on the radial range used for the fit.

To predict GW recoil using observed fits, it is important to use a self-consistent dataset, which avoids differences in r_{b} and γ due to either the choice of model or differences in fitting algorithm. In this chapter, we present just such a dataset.

5.2 Method

I obtained the original surface brightness profiles for 24 galaxies, which had $r_\mathrm{b} > 0.5$ kpc when originally fitted, from the observers. 6 galaxies had fits from two observers, one using the Nuker profile, and the other using the core-Sérsic profile. I converted the values μ in magnitudes per square arcsecond to an arbitrary linear surface brightness Σ, given by:

$$\log \Sigma = \frac{\mu_0 - \mu}{2.5}\,, \tag{5.1}$$

normalised by setting μ_0 equal to the faintest original value. I refitted all galaxies with a core-Sérsic profile, but 4 had additional nuclear light in their profiles, to which I fitted an additional three-parameter Sérsic model. I performed these Sérsic fits simultaneously with the core-Sérsic fits, to give a combined nine-parameter profile. I performed all fits using a Markov chain Monte Carlo (MCMC) algorithm, with wide, flat priors, where possible. In the case of degeneracy preventing a good fit being found, I restricted the effective radius to a narrow range: that obtained by measuring the overall light ±1 kpc.

5.3 Results

As examples of the fitting procedure, the surface brightness profiles and overplots of the MCMC fits for NGC 4889, A3571-BCG, NGC 4486, and NGC 5576 are given in Figures 5.1, 5.3, 5.5, and 5.7, and corner plots for these galaxies are shown in Figures 5.2, 5.4, 5.6, and 5.8, respectively.

NGC 4889 is a good example of a galaxy where a good fit is obtained with open priors. Figure 5.1 shows that the MCMC fit matches the surface brightness profile well at all radii. However, in Figure 5.2, some degeneracy can be seen between r_b, r_e and n, and this can also be seen when fitting other galaxies.

A3571-BCG is an example of a galaxy where intracluster light is present, and also where r_e had to be fixed to get a good MCMC fit. Figure 5.3 also shows that a good fit to the inner part of the profile is achievable by excluding the data at larger radii. The intracluster light is clearly causing the profile to diverge from the outer Sérsic part of the profile, but the important part which informs r_b and γ is well fitted.

NGC 4486 is one of the galaxies from Dullo (2019) with additional nuclear light. Figure 5.5 shows how the nine-parameter combination of Sérsic profile to fit the additional light plus core-Sérsic profile to fit the remainder, can match the profile well in its entirety.

The results of all the core-Sérsic fits are given in Table 5.1, and the combined Sérsic and core-Sérsic fits in Table 5.2.

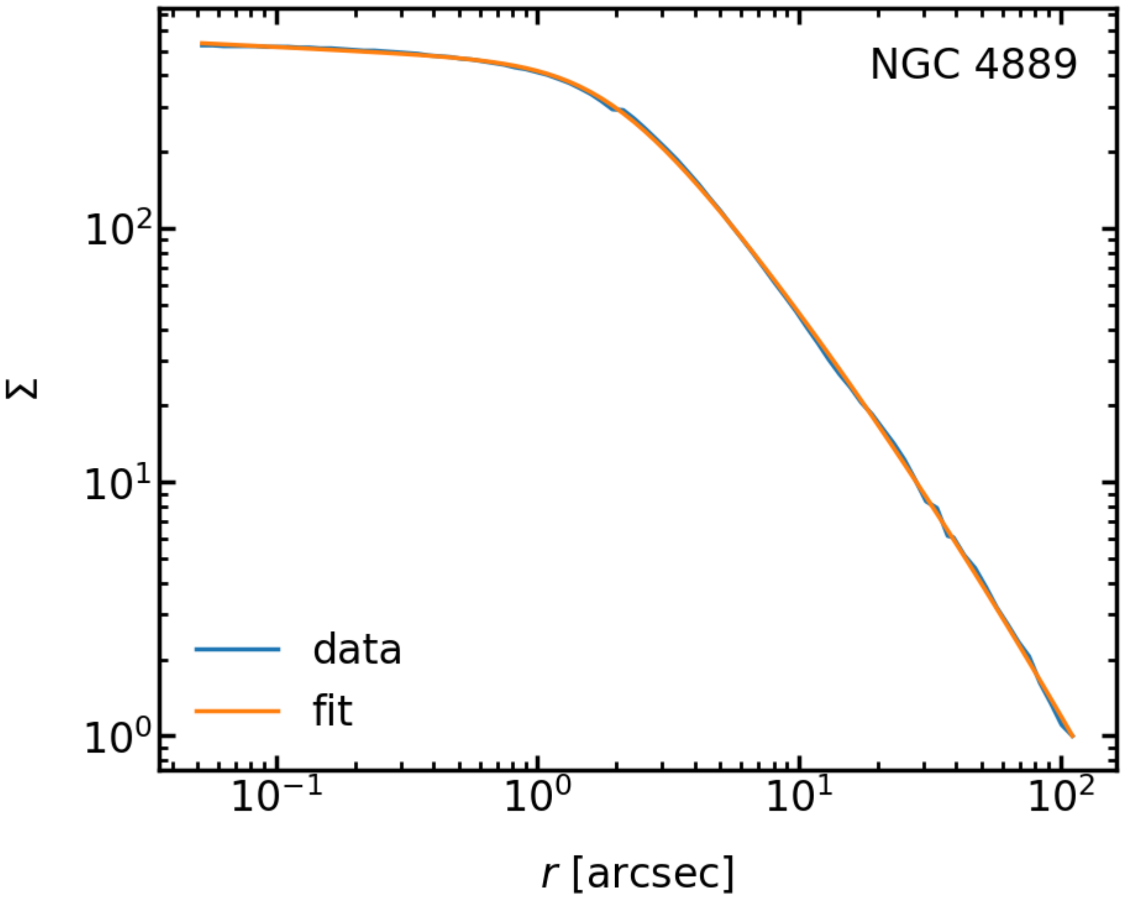

Figure 5.1: MCMC fit of NGC 4889, with open priors. A good fit is achieved without the need to fix any parameters.

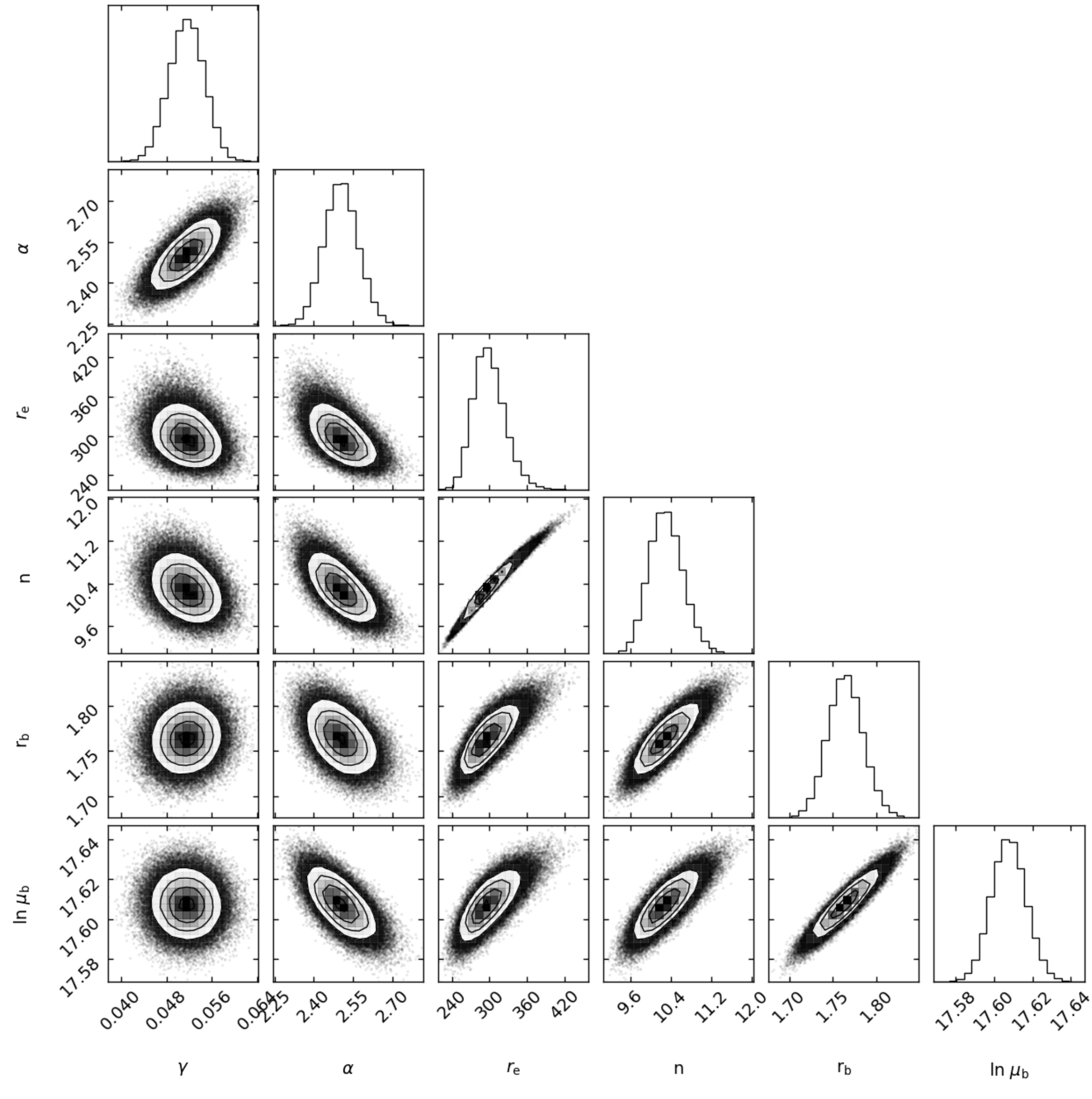

Figure 5.2: Corner plot of fit for NGC 4889. Notice the degeneracy between r_b, r_e and n.

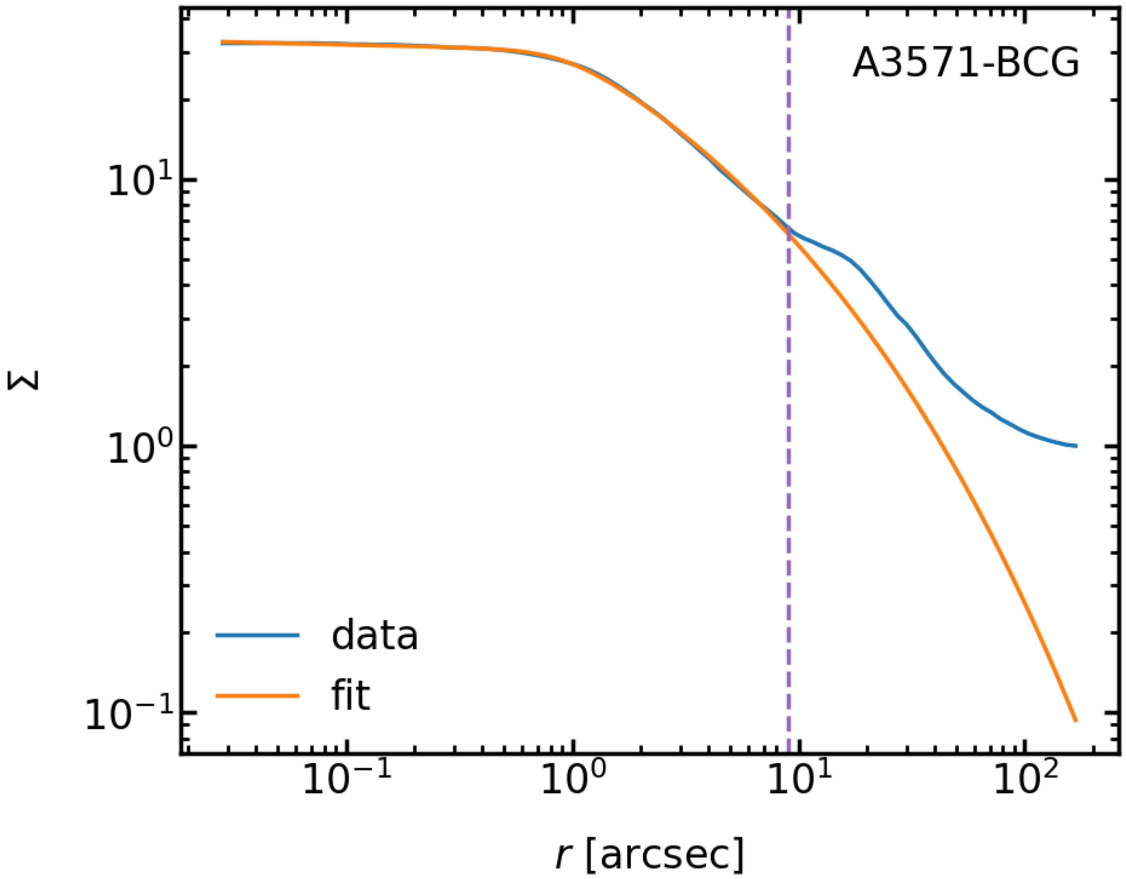

Figure 5.3: MCMC fit of A3571-BCG, with fixed r_e. Although there is intracluster light, a good fit can still be obtained by restriction to smaller radii, here < 9 arcsec (dashed line).

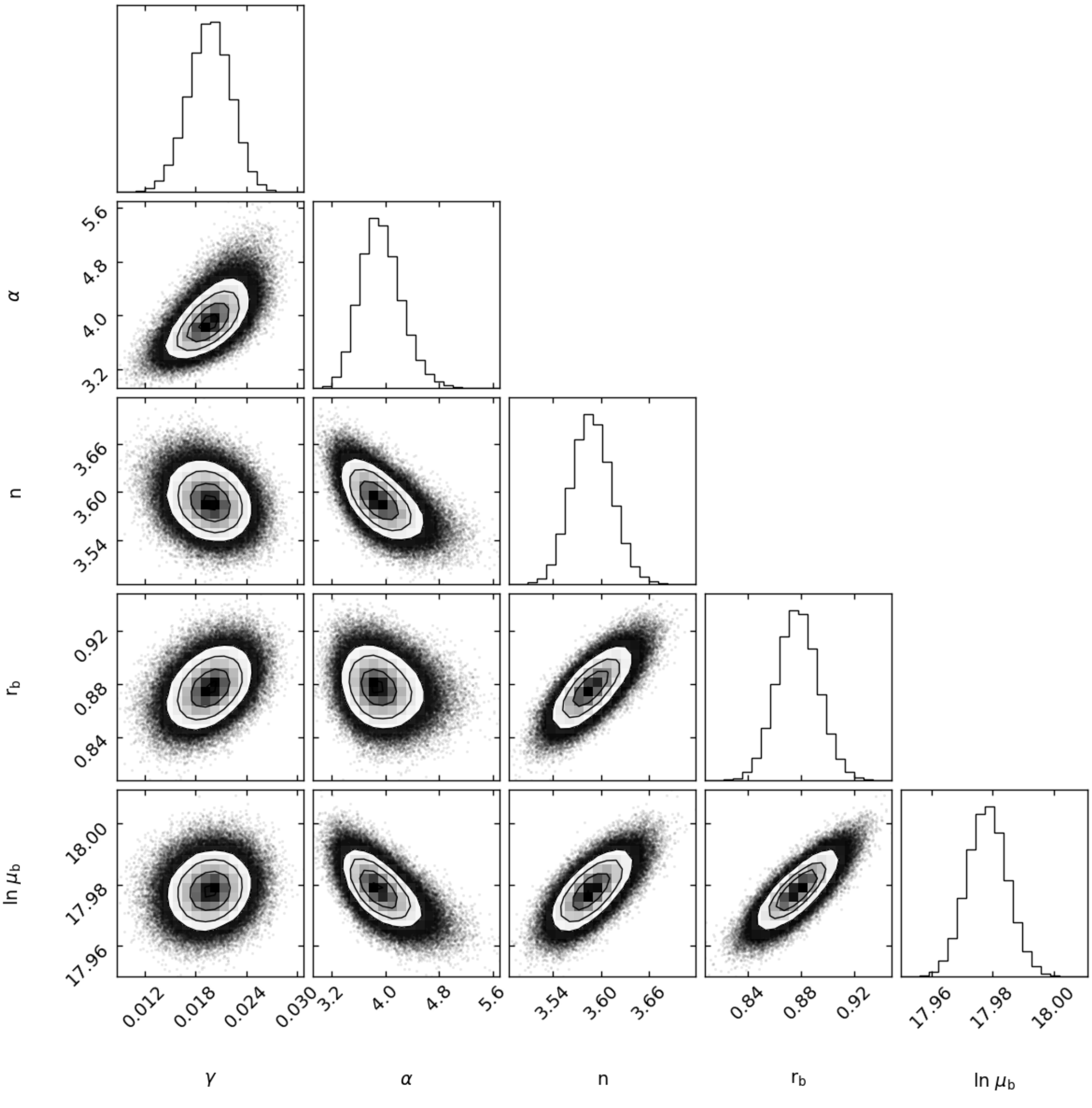

Figure 5.4: Corner plot of fit for A3571-BCG. r_e has been restricted and so is omitted from the plot.

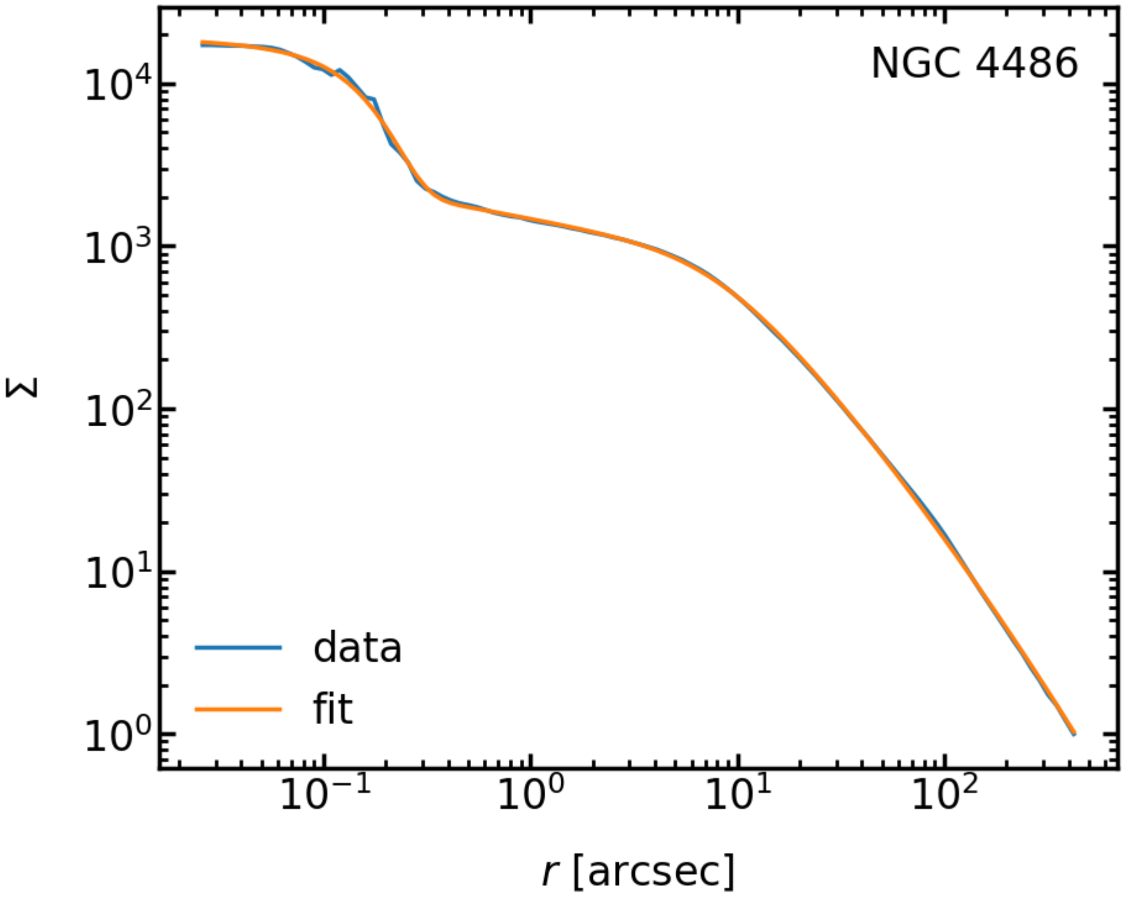

Figure 5.5: MCMC fit of NGC 4486, with open priors. Here the nine-parameter joint fit is used and achieves a good fit to the entire profile.

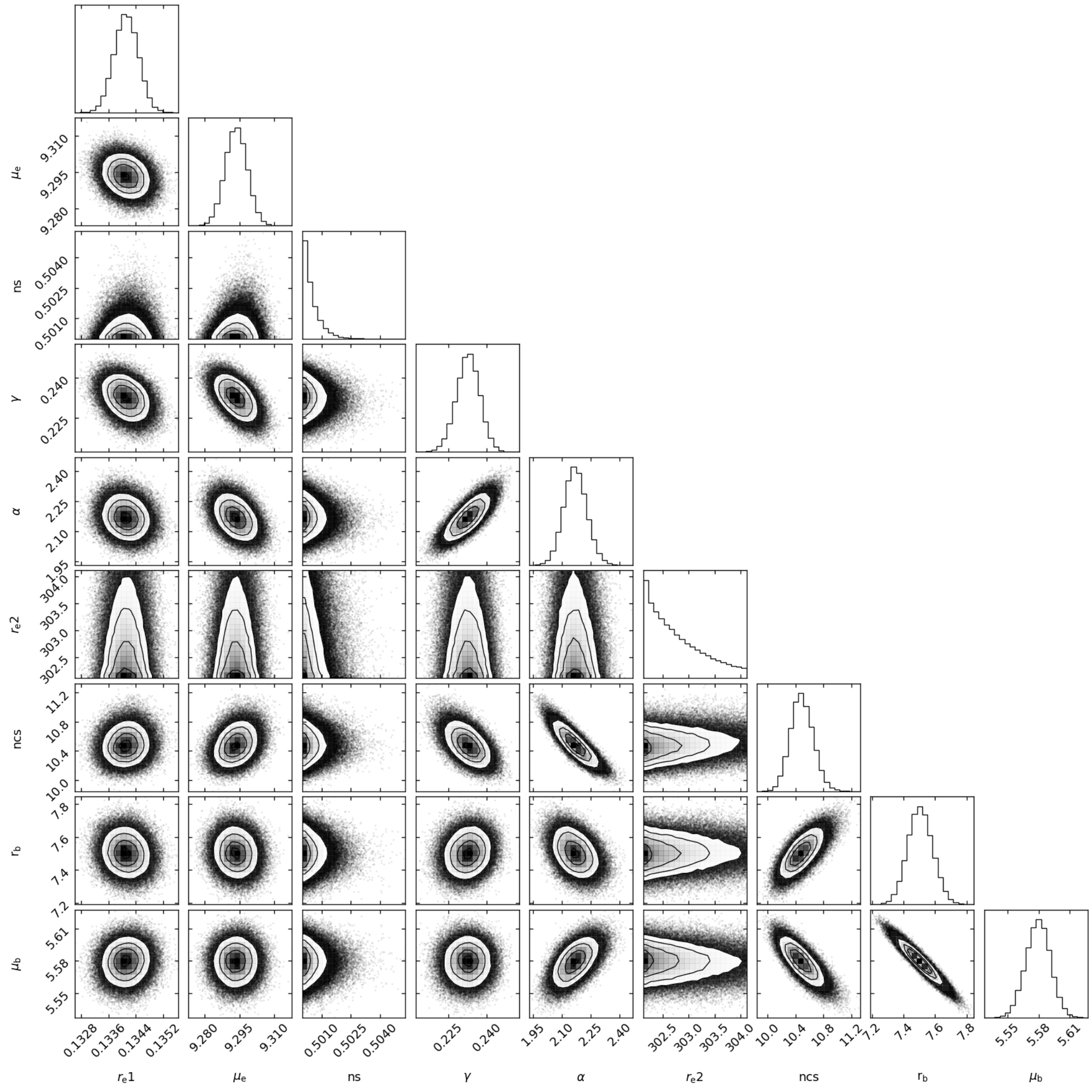

Figure 5.6: Corner plot of fit for NGC 4486. The first three parameters, $r_\mathrm{e}1$, μ_e and ns are the effective radius, surface brightness at the effective radius and Sérsic index for the Sérsic fit to the additional central light. The remaining parameters are from the core-Sérsic fit, where ncs is the Sérsic index of the core-Sérsic profile.

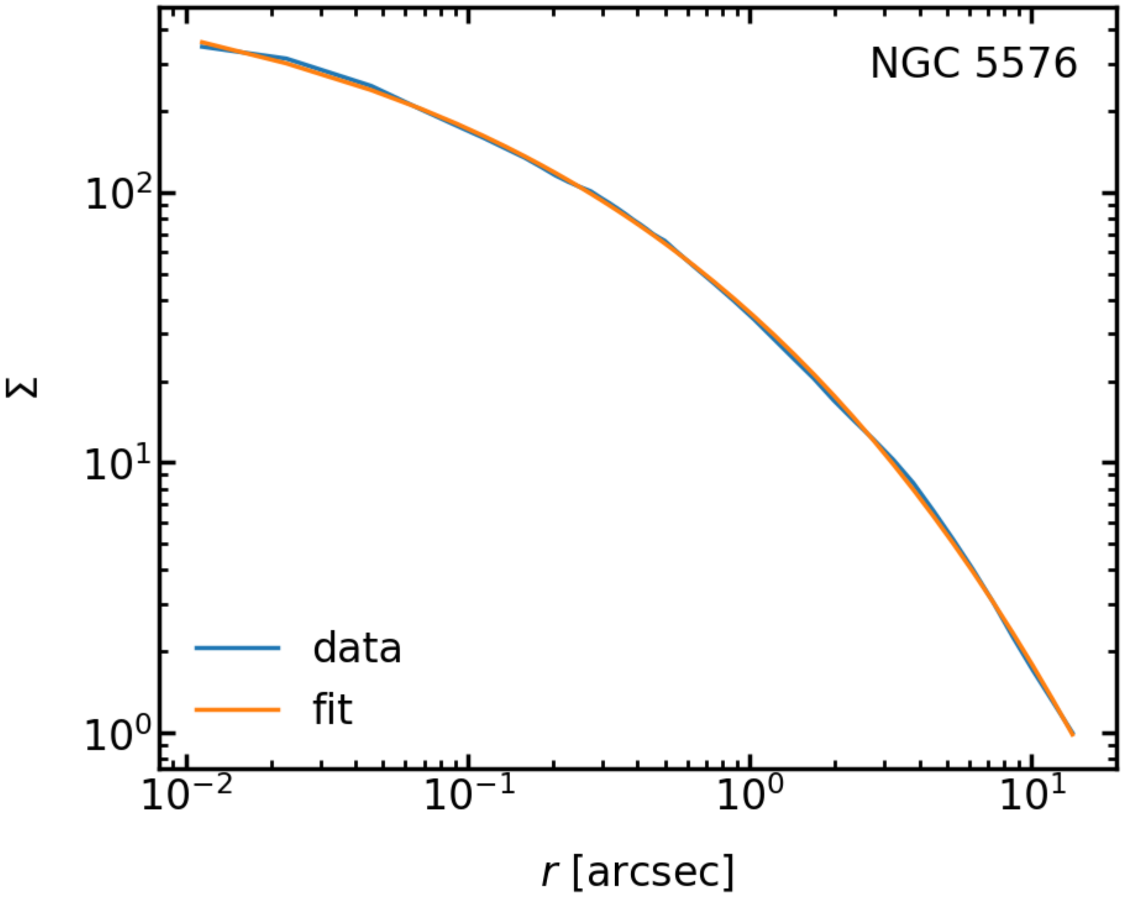

Figure 5.7: MCMC fit of NGC 5576, with open priors. A good fit appears to be achieved but the value of r_b is markedly different from that in Lauer et al. (2005). This is likely due to the degeneracy of parameters seen in Figure 5.8.

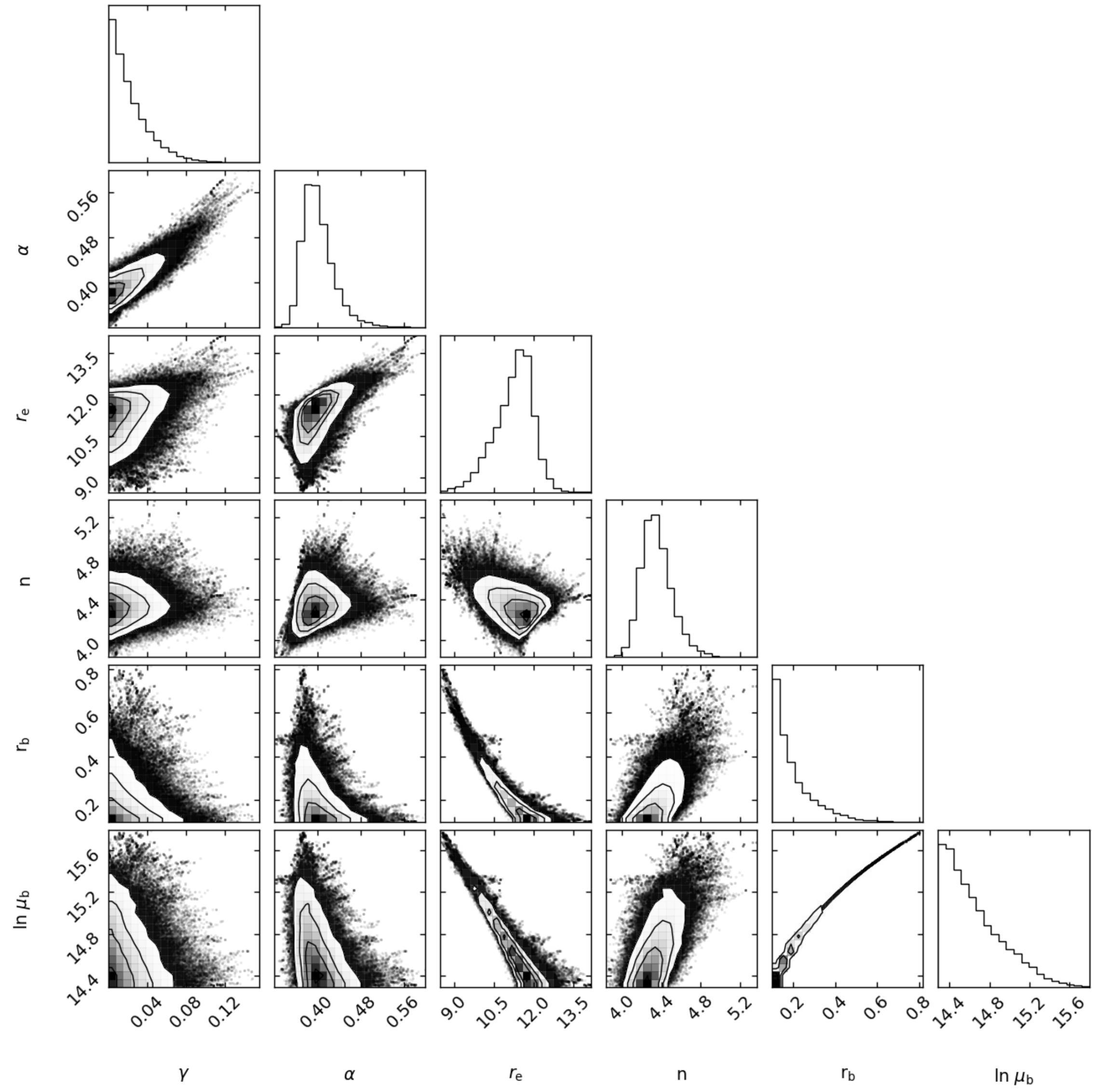

Figure 5.8: Corner plot of fit for NGC 5576, showing severe degeneracy.

Table 5.1: 6-parameter Core-Sersic fit.

Galaxy	Fit	Profile	γ	α	r_{e} [arcsec]	r_{e} [kpc]	n	r_{b} [arcsec]	r_{b} [kpc]	μ_b
A1689-BCG	MCMC	CS*	$0.042^{+0.003}_{-0.003}$	$2.80^{+0.09}_{-0.09}$		$263.4^{+0.7}_{-0.7}$	$12.89^{+0.08}_{-0.18}$		$3.29^{+0.03}_{-0.03}$	$19.860^{+0.009}_{-0.009}$
	A-M	CS				8.3	1.6		3.8	20.1
	A-M	CS				6.3	1.4		3.0	20.1
	A-M	CS				20.3	8.7		4.0	20.1
NGC 1600	MCMC	CS	$0.03^{+0.02}_{-0.02}$	$2.3^{+0.6}_{-1.7}$	$64.2^{+3.8}_{-4.7}$	$20.2^{+1.2}_{-1.5}$	$5.1^{+0.5}_{-0.8}$	$1.7^{+0.2}_{-0.3}$	$0.54^{+0.06}_{-0.09}$	$15.0^{+0.1}_{-0.1}$
	Dullo	CS	0.04	2	72.6	22.8	6.3	2.08	0.65	15.14
A2147-BCG	MCMC	CS*	$0.11^{+0.02}_{-0.02}$	$1.51^{+0.10}_{-0.08}$	$131.6^{+0.7}_{-0.7}$	$94.6^{+0.5}_{-0.5}$	$7.8^{+0.6}_{-0.4}$	$1.09^{+0.07}_{-0.06}$	$1.6^{+0.2}_{-0.2}$	$17.97^{+0.05}_{-0.05}$
	Dullo	CS	0.14	2	44.6	31.8	6.4	1.79	1.28	18.09
A2147-BCG	MCMC	CS *	$0.166^{+0.007}_{-0.007}$	$1.4^{+0.1}_{-0.1}$	$50.4^{+0.7}_{-0.7}$	$33.1^{+0.4}_{-0.5}$	7^{+1}_{-1}	$2.1^{+0.3}_{-0.2}$	$1.4^{+0.2}_{-0.1}$	$18.0^{+0.1}_{-0.1}$
	Lauer	Nuker	0.18					2.21	1.50	
A2261-BCG	MCMC	CS *	$0.00^{+0.01}_{-0.01}$	$4.4^{+0.8}_{-0.6}$	$18.1^{+0.5}_{-0.7}$	$68.5^{+1.8}_{-2.7}$	$4.5^{+0.2}_{-0.2}$	$0.87^{+0.03}_{-0.02}$	$3.29^{+0.11}_{-0.08}$	$18.71^{+0.02}_{-0.02}$
	Dullo	CS	0.00	5	4.9	17.6	2.1	0.75	2.71	18.69
4C +74.13	MCMC	CS *	$0.03^{+0.01}_{-0.01}$	$1.24^{+0.05}_{-0.05}$	$26.47^{+0.37}_{-0.68}$	$97.30^{+1.35}_{-2.49}$	$9.86^{+0.79}_{-0.59}$	$0.61^{+0.03}_{-0.02}$	$2.26^{+0.10}_{-0.08}$	$18.79^{+0.03}_{-0.03}$
	Dullo	CS	0.28	2	6.0	20.9	3.7	0.64	2.24	18.83
NGC 4889	MCMC	CS	$0.051^{+0.003}_{-0.003}$	$2.50^{+0.07}_{-0.06}$	297^{+27}_{-23}	183^{+16}_{-14}	$10.3^{+0.3}_{-0.3}$	$1.76^{+0.02}_{-0.02}$	$1.08^{+0.01}_{-0.01}$	$17.608^{+0.009}_{-0.009}$
	Dullo	CS	0.04	2	563.9	256.7	13.3	1.89	0.86	17.68

Table 5.1: 6-parameter Core-Sersic fit.

Galaxy	Fit	Profile	γ	α	r_{e} [arcsec]	r_{e} [kpc]	n	r_{b} [arcsec]	r_{b} [kpc]	μ_b
A0119-BCG	MCMC	CS *	$0.06^{+0.00}_{-0.00}$	$3.89^{+0.18}_{-0.17}$	$141.17^{+0.63}_{-0.72}$	$121.94^{+0.54}_{-0.62}$	$7.17^{+0.05}_{-0.04}$	$0.75^{+0.01}_{-0.01}$	$0.65^{+0.01}_{-0.01}$	$17.33^{+0.01}_{-0.01}$
	Dullo	CS	0.10	5	112.5	96.1	6.8	0.78	0.67	17.34
A0119-BCG	MCMC	CS *	$0.064^{+0.004}_{-0.004}$	$5.4^{+0.5}_{-0.4}$	$36.74^{+0.07}_{-0.15}$	$30.46^{+0.06}_{-0.13}$	$3.97^{+0.02}_{-0.02}$	$0.579^{+0.009}_{-0.008}$	$0.480^{+0.007}_{-0.007}$	$16.987^{+0.007}_{-0.007}$
	Lauer	Nuker	0.06					0.80	0.69	
A3558-BCG	MCMC	CS	$0.03^{+0.00}_{-0.00}$	$2.14^{+0.07}_{-0.07}$	$119.85^{+3.09}_{-2.89}$	$113.74^{+2.93}_{-2.74}$	$5.09^{+0.08}_{-0.08}$	$1.30^{+0.02}_{-0.02}$	$1.23^{+0.02}_{-0.02}$	$18.04^{+0.01}_{-0.01}$
	Dullo	CS	0.03	2	131.9	123.7	5.4	1.39	1.30	18.08
A3558-BCG	MCMC	CS *	$0.058^{+0.004}_{-0.004}$	$2.6^{+0.2}_{-0.1}$	$99.9^{+0.7}_{-0.7}$	$84.1^{+0.6}_{-0.6}$	$4.52^{+0.07}_{-0.06}$	$1.23^{+0.03}_{-0.03}$	$1.03^{+0.03}_{-0.02}$	$17.79^{+0.01}_{-0.01}$
	Lauer	Nuker	0.05					1.73	1.52	
A3562-BCG	MCMC	CS *	$0.002^{+0.003}_{-0.001}$	$1.50^{+0.03}_{-0.03}$	$71.13^{+0.67}_{-0.69}$	$70.14^{+0.66}_{-0.68}$	$6.35^{+0.11}_{-0.10}$	$0.79^{+0.02}_{-0.02}$	$0.77^{+0.02}_{-0.02}$	$17.74^{+0.02}_{-0.01}$
	Dullo	CS	0.06	2	18.9	18.4	3.6	0.66	0.64	17.66
A3562-BCG	MCMC	CS	$0.013^{+0.011}_{-0.008}$	$1.4^{+0.2}_{-0.1}$	72^{+89}_{-25}	62^{+76}_{-21}	6^{+2}_{-1}	$0.7^{+0.1}_{-0.1}$	$0.6^{+0.1}_{-0.1}$	$17.43^{+0.10}_{-0.08}$
	Lauer	Nuker	0.00					1.15	1.03	
NGC 4874	MCMC	CS	$0.103^{+0.003}_{-0.004}$	$1.90^{+0.07}_{-0.07}$	$18.11^{+7.64}_{-5.26}$	$9.12^{+3.85}_{-2.65}$	$11.52^{+1.09}_{-1.96}$	$3.29^{+0.15}_{-0.14}$	$1.66^{+0.08}_{-0.07}$	$18.96^{+0.05}_{-0.04}$
	Dullo	CS	0.13	2	4.9	2.5	4.0	3.25	1.63	19.05
NGC 4874	MCMC	CS	$0.051^{+0.003}_{-0.003}$	$2.90^{+0.09}_{-0.09}$	83^{+14}_{-17}	42^{+7}_{-8}	$12.3^{+0.5}_{-1.0}$	$1.97^{+0.03}_{-0.03}$	$0.99^{+0.01}_{-0.01}$	$17.72^{+0.01}_{-0.01}$
	Lauer	Nuker	0.12					3.35	1.73	

Table 5.1: 6-parameter Core-Sersic fit.

Galaxy	Fit	Profile	γ	α	$r_{\rm e}$ [arcsec]	$r_{\rm e}$ [kpc]	n	$r_{\rm b}$ [arcsec]	$r_{\rm b}$ [kpc]	μ_b
A3571-BCG	MCMC	CS *	$0.019^{+0.002}_{-0.003}$	$3.68^{+0.29}_{-0.26}$	$118.81^{+0.65}_{-0.71}$	$93.74^{+0.51}_{-0.56}$	$3.64^{+0.03}_{-0.03}$	$0.90^{+0.02}_{-0.02}$	$0.71^{+0.01}_{-0.01}$	$17.99^{+0.01}_{-0.01}$
	Dullo	CS	0.01	2	68.9	53.8	10.2	1.70	1.33	18.56
A3571-BCG	MCMC	CS *	$0.023^{+0.004}_{-0.004}$	$4.3^{+0.4}_{-0.4}$	$137.5^{+0.6}_{-0.7}$	$97.5^{+0.4}_{-0.5}$	$3.61^{+0.02}_{-0.02}$	$0.82^{+0.02}_{-0.02}$	$0.58^{+0.01}_{-0.01}$	$17.766^{+0.007}_{-0.007}$
	Lauer	Nuker	0.02					1.15	0.84	
IC 1101	MCMC	CS	$0.118^{+0.002}_{-0.003}$	$4.2^{+0.2}_{-0.2}$	86^{+1}_{-1}	140^{+2}_{-2}	$4.43^{+0.05}_{-0.05}$	$1.59^{+0.02}_{-0.02}$	$2.58^{+0.03}_{-0.03}$	$18.821^{+0.007}_{-0.007}$
	Dullo	CS	0.05	2	5.3	8.0	6.32	2.52	3.8	19.33
A3376-BCG	MCMC	CS	$0.051^{+0.003}_{-0.003}$	$2.90^{+0.09}_{-0.09}$	83^{+14}_{-16}	68^{+12}_{-13}	$12.3^{+0.5}_{-1.0}$	$1.97^{+0.03}_{-0.03}$	$1.62^{+0.02}_{-0.02}$	$17.72^{+0.01}_{-0.01}$
	Lauer	Nuker	0.05					1.95	1.66	
A0397-BCG	MCMC	CS	$0.073^{+0.004}_{-0.004}$	$2.99^{+0.09}_{-0.09}$	169^{+11}_{-14}	106^{+7}_{-9}	$12.8^{+0.1}_{-0.3}$	$0.965^{+0.008}_{-0.008}$	$0.603^{+0.005}_{-0.005}$	$16.544^{+0.008}_{-0.008}$
	Lauer	Nuker	0.07					1.06	0.68	
A0376-BCG	MCMC	CS *	$0.194^{+0.006}_{-0.007}$	$3.2^{+0.2}_{-0.2}$	$31.34^{+0.06}_{-0.13}$	$28.40^{+0.05}_{-0.12}$	$5.10^{+0.03}_{-0.03}$	$0.447^{+0.009}_{-0.009}$	$0.405^{+0.008}_{-0.008}$	$16.68^{+0.01}_{-0.01}$
	Lauer	Nuker	0.19					0.68	0.64	
NGC 1016	MCMC	CS	$0.09^{+0.01}_{-0.01}$	$1.07^{+0.07}_{-0.06}$	26^{+7}_{-5}	9^{+3}_{-2}	10^{+2}_{-3}	$1.08^{+0.10}_{-0.17}$	$0.39^{+0.04}_{-0.06}$	$17.59^{+0.08}_{-0.14}$
	Lauer	Nuker	0.09					1.68	0.62	

Table 5.1: 6-parameter Core-Sersic fit.

Galaxy	Fit	Profile	γ	α	r_{e} [arcsec]	r_{e} [kpc]	n	r_{b} [arcsec]	r_{b} [kpc]	μ_b
A3528-BCG	MCMC	CS *	$0.187^{+0.005}_{-0.005}$	$3.2^{+0.1}_{-0.1}$	$99.4^{+0.6}_{-0.7}$	$94.2^{+0.5}_{-0.7}$	$8.87^{+0.07}_{-0.06}$	$0.498^{+0.006}_{-0.006}$	$0.472^{+0.006}_{-0.006}$	$16.254^{+0.010}_{-0.010}$
	Lauer	Nuker	0.18					0.61	0.61	
NGC 7727	MCMC	CS *	$0.618^{+0.006}_{-0.004}$	$1.04^{+0.03}_{-0.02}$	$9.89^{+0.01}_{-0.03}$	$1.030^{+0.001}_{-0.003}$	$2.3^{+0.2}_{-0.2}$	$5.58^{+0.03}_{-0.11}$	$0.581^{+0.004}_{-0.012}$	$18.311^{+0.007}_{-0.028}$
	Lauer	Nuker	0.43					5.74	0.60	
NGC 5576	MCMC	CS	$0.02^{+0.02}_{-0.01}$	$0.40^{+0.03}_{-0.02}$	$11.3^{+0.6}_{-0.9}$	$1.48^{+0.07}_{-0.11}$	$4.3^{+0.2}_{-0.1}$	$0.17^{+0.13}_{-0.05}$	$0.02^{+0.02}_{-0.01}$	$14.6^{+0.4}_{-0.2}$
	Lauer	Nuker	0.01					4.18	0.55	
NGC 3842	MCMC	CS	$0.175^{+0.005}_{-0.005}$	$3.0^{+0.2}_{-0.2}$	189^{+133}_{-63}	87^{+61}_{-29}	9^{+1}_{-1}	$0.80^{+0.03}_{-0.02}$	$0.37^{+0.01}_{-0.01}$	$17.51^{+0.02}_{-0.02}$
	Lauer	Nuker	0.15					1.08	0.51	
A0295-BCG	MCMC	CS *	$0.132^{+0.004}_{-0.004}$	$5.8^{+0.4}_{-0.4}$	$39.3^{+0.1}_{-0.3}$	$30.88^{+0.09}_{-0.20}$	$5.80^{+0.03}_{-0.03}$	$0.508^{+0.006}_{-0.006}$	$0.398^{+0.005}_{-0.005}$	$16.395^{+0.007}_{-0.007}$
	Lauer	Nuker	0.13					0.63	0.51	

Notes: An asterisk indicated the effective radius was fixed to achieve the fit.
Fit column: MCMC indicates the core-Sérsic Markov chain Monte Carlo fit performed in this study, Dullo indicates a core-Sérsic fit from Dullo (2019), and Lauer indicates a Nuker fit from Lauer et al. (1995) or Lauer et al. (2005).
A galaxy is listed twice if two sets of observer surface brightness profiles and fits are available.

Table 5.2: Combined Sérsic fit and core-Sérsic fit for galaxies with central light excess.

Galaxy	Fit	Sérsic				Core-Sérsic/Nuker							
		r_e	r_e	μ_e	n	γ	α	r_e	r_e	n	r_b	r_b	μ_b
			[kpc]						[kpc]			[kpc]	
NGC 6166	MCMC	0.07	0.05	$16.17^{+0.05}_{-0.05}$	$0.89^{+0.04}_{-0.03}$	$0.13^{+0.01}_{-0.01}$	$2.7^{+0.1}_{-0.1}$	$170.8^{+0.4}_{-0.7}$	$104.9^{+0.2}_{-0.4}$	$6.19^{+0.04}_{-0.04}$	$2.73^{+0.03}_{-0.03}$	$1.67^{+0.02}_{-0.02}$	18.12
	Dullo	0.02	0.01	13.44	0.66	0.05	2.00	136.50	83.10	9.00	3.46	2.11	18.26
NGC 4486	MCMC	0.13	0.01	13.26	0.50	$0.23^{+0.00}_{-0.01}$	$2.17^{+0.06}_{-0.06}$	$302.6^{+0.7}_{-0.4}$	$33.57^{+0.08}_{-0.04}$	$10.5^{+0.2}_{-0.2}$	$7.50^{+0.08}_{-0.07}$	$0.83^{+0.01}_{-0.01}$	$16.68^{+0.01}_{-0.01}$
	Dullo	–	–	–	–	0.24	5	185.9	20.6	6.2	5.8	0.64	16.41
NGC 4889	MCMC	8^{+9}_{-7}	3^{+4}_{-3}	18^{+3}_{-4}	11^{+2}_{-4}	$0.07^{+0.00}_{-0.02}$	1^{+29}_{-0}	$8.0^{+0.3}_{-1.1}$	$3.5^{+0.1}_{-0.5}$	10^{+2}_{-9}	$4.4^{+0.1}_{-4.2}$	$1.94^{+0.05}_{-1.85}$	$19.67^{+0.03}_{-1.21}$
	Lauer	–	–	–	–	0.06	–	–	–	–	1.68	0.74	–
A1831-BCG	MCMC	18^{+2}_{-4}	24^{+2}_{-6}	$21.67^{+0.06}_{-1.00}$	$0.85^{+7.14}_{-0.08}$	$0.11^{+0.01}_{-0.01}$	8^{+46}_{-2}	$4.70^{+1.50}_{-0.40}$	6^{+2}_{-0}	$3.2^{+0.3}_{-0.9}$	$0.42^{+0.01}_{-0.13}$	$0.54^{+0.01}_{-0.17}$	$18.59^{+0.02}_{-0.17}$
	Lauer	–	–	–	–	0.24	–	–	–	–	0.50	0.64	–

Notes: Fit column: MCMC indicates the core-Sérsic Markov chain Monte Carlo fit performed in this study, Dullo indicates a core-Sérsic fit from Dullo (2019), and Lauer indicates a Nuker fit from Lauer et al. (1995).
Errors of < 0.01 are omitted for clarity.

The differences between the core sizes and γ values of the original and new fits are shown in Figure 5.9.

A truncated version of 3.7, showing the $M_\bullet$ - r_b relation for the galaxies in Dullo (2019), but with the addition of the refitted values, is shown in Figure 5.10. Unfortunately, these are the only galaxies with both SMBH masses and refitted profiles, and so the number of points is limited. In general, the refitted r_b and γ values are close to the originals, but there is no obvious pattern, with some closer to the overall relation and others further away.

The r_b-γ relation is shown in Figure 5.11. Although galaxies with small cores have a range of γ values, so that there are galaxies with small cores and flatter cores, the refitted profiles show no galaxies with large cores and cuspier profiles. Galaxies with small cores show a large scatter in gamma, while those with larger cores favour a gamma close to zero.

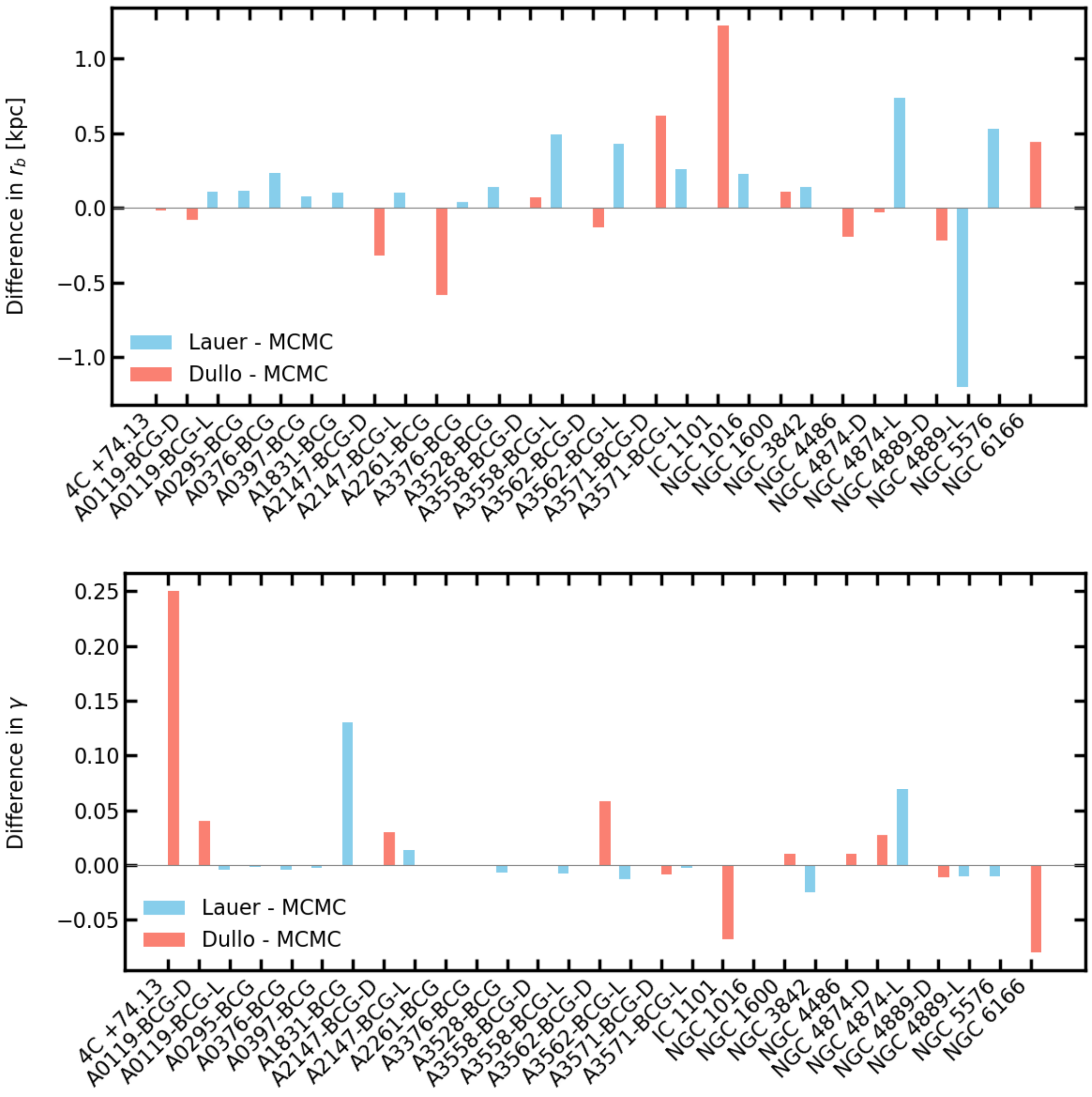

Figure 5.9: Differences between the original core sizes (top) and γ values (bottom) for galaxies from Lauer et al. (1995) or Lauer et al. (2005) (blue, suffix -L) and Dullo (2019) (red, suffix -D) and the refitted MCMC values. Suffixes are used after a galaxy name if surface brightness data was available from both sources.

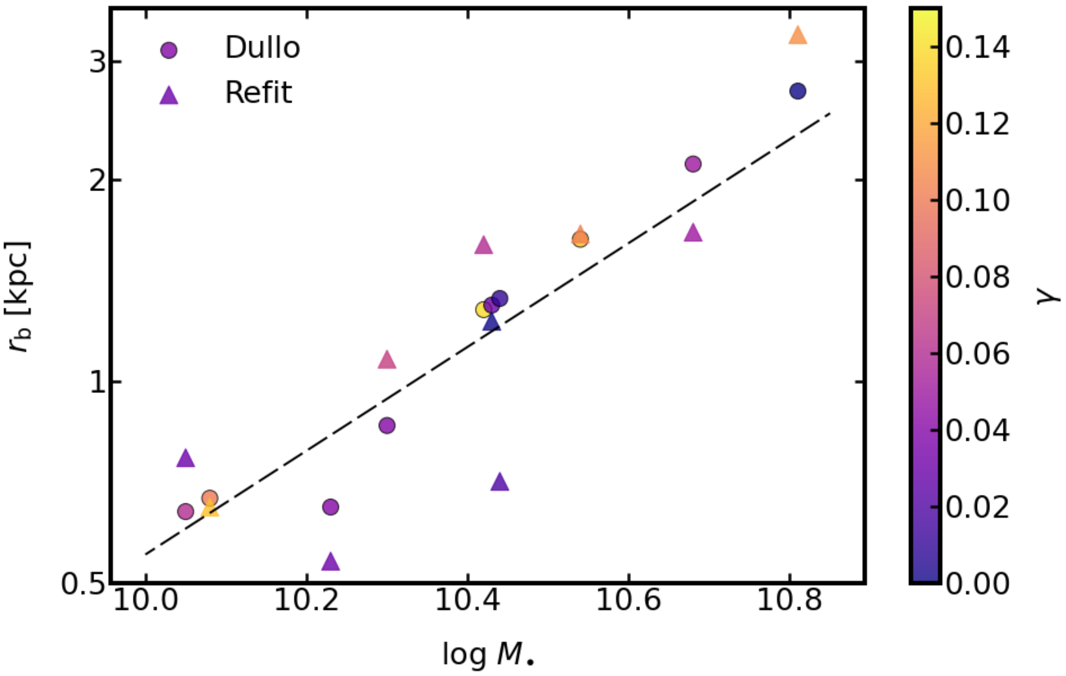

Figure 5.10: The BH mass - core size scaling relation for the galaxies in Dullo (2019). The original fits are shown as circles and the refitted values as triangles. The dashed line shows the best fitting relation for all galaxies with available BH masses from Khonji et al. (2024).

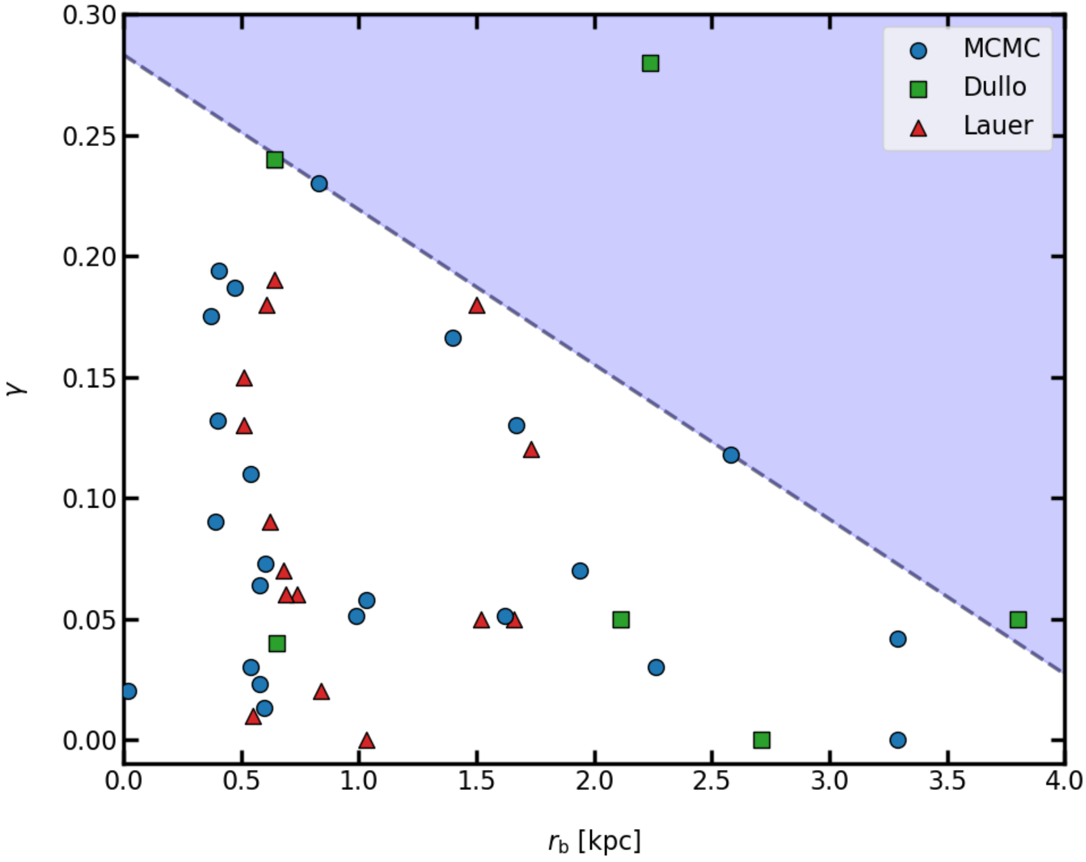

Figure 5.11: The r_b-γ relation for the sample of 24 observed galaxies. Although there are a few galaxies with small cores and flat cores, large cores appear to exclude more cuspy profiles (blue shaded area).

5.4 Discussion

As can be seen in Table 5.1, the majority of fits are in reasonable agreement with the original fits by the observers, in terms of r_b and γ. However, in general, we find that we obtain core sizes lower than the Nuker fits from Lauer et al. (2005) and Lauer et al. (2005). This is consistent with previous findings in Graham et al. (2003). On the other hand, the agreement with γ is generally good for both Nuker and core-Sérsic observer fits (Figure 5.9). There are also occasional outliers, such as NGC 5576, where we obtain a core size less than 10% of that reported in Lauer et al. (2005). This is likely due the profile having severe degeneracy, with no clear break radius visible.

The r_b-γ relation (Figure 5.11) indicates that very large cores, which Khonji et al. (2024) show require GW recoil to form, cannot have cuspy profiles. This is consistent with them having experienced a significantly large recoil kick. The presence of flatter small cores emphasises that the flatness of the profile is influenced by other galaxy parameters, such as SMBH mass, bulge stellar mass, effective radius, and Sérsic index. To fully understand these relationships, it is likely that this parameter space will need to be explored.

Chapter 6

Conclusions and Future Work

In this thesis, we have studied the effects of GW recoil in giant elliptical galaxies. We found that, in combination with black hole binary scouring, recoil may result in the formation of the very large cores, seen in some of these massive elliptical galaxies.

We performed equal-mass merger simulations of multicomponent galaxy models, based on the observed parameters of four massive elliptical galaxies with cores $> 0.5\,\mathrm{kpc}$. After binary scouring and hardening, the merged SMBH remnant is given a range of GW recoil kicks with 0.5-0.9 of the escape speed of the galaxy.

We found that binary scouring alone can form cores of up to ~ 1.3 kpc, such as those observed in NGC 1600 and A2147-BCG. However, an additional process is required to form the largest cores, greater than 2 kpc, as observed in galaxies such as NGC 6166 and A2261-BCG.

We showed that GW recoil can form these very large cores with kicks of less than half of the escape speed of the remnant galaxy. This corresponds to kick velocities of $\lesssim 2000\,\mathrm{km\ s}^{-1}$, well below the theoretical maximum recoil for spin-dominated kicks at $\sim 5000\,\mathrm{km\ s}^{-1}$.

We also found that GW recoil leads to flatter inner density profiles than binary scouring alone. Interestingly, the values of the inner logarithmic slope γ found after GW kicks are much closer to those of the observed profiles of these galaxies than those with binary scouring alone. This indicates that GW recoil may be a common phenomenon in such galaxies. Indeed, γ could be a marker for the occurrence of recoil.

We studied the effect of relatively small GW recoil kicks and unexpectedly found that the higher bound mass to the SMBH results in stars being pulled along with the SMBH remnant, a process we call 'BH dragging.' The final result depends on both the kick velocity and the galactic environment. For the smallest kicks the SMBH remnants have the highest bound mass, but there may be little change in the profile, since the SMBH moves only a small distance and is quickly damped, so recoil heating is minimal. For kicks with speeds 0.3-0.5 of v_{esc}, there is usually a reduction in overall density further out due to the greater distance traveled by the SMBH. In this situation, the combination of 'BH dragging' and recoil heating results in the nuclear density being distinct above the remainder of the stellar bulge. This new mechnism could explain the additional nuclear light, perhaps due to nuclear star clusters, seen in $\sim 20\%$ of galaxies with large cores Lauer et al. (1995); Dullo (2019).

Finally, we refitted the surface brightness profiles of 25 galaxies with cores > 0.5 kpc. By using a single model (the core-Sérsic profile) and fitting algorithm, we obtained the most comprehensive self-consistent dataset of the parameters of galaxies with large cores. We find reasonable agreement with previous fits, but in general the refitted core sizes are smaller than those fitted with the Nuker profile. The γ values are in much better agreement with the fits performed by the observers. However, some outlying galaxies exist, whose profiles have severe degeneracy. We find that the presence of large cores appears to exclude cuspy profiles, but that smaller cores can have a range of inner slopes, from cuspy to flat. This emphasises the influence of other factors, such as the parameters of the galactic environment. Nevertheless, this dataset is the first step towards predicting GW recoil with observations.

There are several potential avenues for future work, based on this thesis. Other potential causes of large core formation, such as multiple SMBHs and stalled perturbers, could be modelled and compared with the effects of GW recoil. Higher resolution simulations could be performed to further validate the 'BH dragging' mechanism. However, perhaps the most exciting prospect is in using observations to predict the likelihood that a galaxy has undergone GW recoil and, if so, the likely strength of the kick.

There are still significant obstacles to be overcome. The effect of recoil depends on multiple different galaxy parameters, such as SMBH mass, stellar mass, effective radius, and Sérsic index, as well as the kick velocity. If this parameter space could be explored, an emulator could be developed to predict recoil, which could lead to the first recoil velocity distribution for giant elliptical galaxies from observations. In combination with the theoretical recoil velocity distribution for SMBH spin, this could even provide bounds on the spins of SMBHs in these galaxies, and inform their origin and history.

Bibliography

Aarseth, S., & Zare, K. 1974, Celestial mechanics, 10, 185

Aarseth, S. J., & Hoyle, F. 1963, Monthly Notices of the Royal Astronomical Society, 126, 223

Abbott, B. P., Abbott, R., Abbott, T., et al. 2016, Physical review letters, 116, 061102

Abramowicz, M., Czerny, B., Lasota, J., & Szuszkiewicz, E. 1988, Astrophysical Journal, Part 1 (ISSN 0004-637X), vol. 332, Sept. 15, 1988, p. 646-658. Research supported by Observatoire de Paris and NASA., 332, 646

Agazie, G., Anumarlapudi, A., Archibald, A. M., et al. 2023, The Astrophysical Journal Letters, 951, L8

Akiyama, K., Alberdi, A., Alef, W., et al. 2019, The Astrophysical Journal Letters, 875, L4

—. 2022, The Astrophysical Journal Letters, 930, L12

Alamo-Martínez, K., & Blakeslee, J. 2017, The Astrophysical Journal, 849, 6

Antoniadis, J., Arumugam, P., Arumugam, S., et al. 2023, Astronomy & Astrophysics, 678, A50

Antoniadis, J., Arumugam, P., Arumugam, S., et al. 2023, arXiv e-prints, arXiv:2306.16227, doi: `10.48550/arXiv.2306.16227`

Antonini, F. 2013, The Astrophysical Journal, 763, 62

Antonini, F., Barausse, E., & Silk, J. 2015, The Astrophysical Journal, 812, 72

Antonini, F., Capuzzo-Dolcetta, R., Mastrobuono-Battisti, A., & Merritt, D. 2012, The Astrophysical Journal, 750, 111

Antonini, F., & Merritt, D. 2011, The Astrophysical Journal, 745, 83

Archive, H. L. 2024, Hubble Legacy Archive. `https://hla.stsci.edu`

Attard, K., Gualandris, A., Read, J. I., & Dehnen, W. 2024, arXiv e-prints, arXiv:2402.10709. `https://arxiv.org/abs/2402.10709`

Attard, K., Gualandris, A., Read, J. I., & Dehnen, W. 2024, Monthly Notices of the Royal Astronomical Society, 529, 2150

Baker, J. G., Centrella, J., Choi, D.-I., et al. 2006, The Astrophysical Journal, 653, L93

Balcells, M., Graham, A. W., Domínguez-Palmero, L., & Peletier, R. F. 2002, The Astrophysical Journal, 582, L79

Balick, B., & Brown, R. L. 1974, Astrophysical Journal, vol. 194, Dec. 1, 1974, pt. 1, p. 265-270., 194, 265

Bardeen, J., Bond, J., Kaiser, N., & Szalay, A. 1986, Astrophys. J.;(United States), 304

Barnes, J., & Hut, P. 1986, nature, 324, 446

Barnes, J. E. 1992, Astrophysical Journal, Part 1 (ISSN 0004-637X), vol. 393, no. 2, July 10, 1992, p. 484-507. Research supported by Canadian Institute for Theoretical Astrophysics., 393, 484

Begelman, M. C., Blandford, R. D., & Rees, M. J. 1980, Nature, 287, 307

Begelman, M. C., & Rees, M. J. 1978, Monthly Notices of the Royal Astronomical Society, 185, 847
Begelman, M. C., Volonteri, M., & Rees, M. J. 2006, Monthly Notices of the Royal Astronomical Society, 370, 289
Bekenstein, J. D. 1973, The Astrophysical Journal, 183, 657
Bekki, K. 2007, Publications of the Astronomical Society of Australia, 24, 77
Bekki, K., & Couch, W. J. 2011, Monthly Notices of the Royal Astronomical Society, 415, 1783
Bekki, K., & Graham, A. W. 2010, The Astrophysical Journal Letters, 714, L313
Bell, E. F., McIntosh, D. H., Katz, N., & Weinberg, M. D. 2003, The Astrophysical Journal Supplement Series, 149, 289
Bender, R., Kormendy, J., Cornell, M. E., & Fisher, D. B. 2015, The astrophysical journal, 807, 56
Berczik, P., Merritt, D., & Spurzem, R. 2005, The Astrophysical Journal, 633, 680
Berti, E., Yagi, K., Yang, H., & Yunes, N. 2018, General Relativity and Gravitation, 50, 1
Binney, J., & Tremaine, S. 2011, Galactic dynamics, Vol. 13 (Princeton university press)
Blumenthal, G. R., Faber, S., Primack, J. R., & Rees, M. J. 1984, Nature, 311, 517
Boco, L., Lapi, A., & Danese, L. 2020, The Astrophysical Journal, 891, 94
Böker, T., Laine, S., van der Marel, R. P., et al. 2002, The Astronomical Journal, 123, 1389
Böker, T., Sarzi, M., McLaughlin, D. E., et al. 2004, The Astronomical Journal, 127, 105
Boker, T., Stanek, R., & van der Marel, R. 2003, ASTRONOMICAL JOURNAL, 125, 1073
Bolton, J., & Stanley, G. 1948, Nature, 161, 312
Bolton, J. G., Stanley, G. J., & Slee, O. 1949, Nature, 164, 101
Bondi, H., & Gold, T. 1948, Monthly Notices of the Royal Astronomical Society, 108, 252
Bondi, H., Van der Burg, M. G. J., & Metzner, A. 1962, Proceedings of the Royal Society of London. Series A. Mathematical and Physical Sciences, 269, 21
Bonfini, P., & Graham, A. W. 2016, The Astrophysical Journal, 829, 81
Bortolas, E., Gualandris, A., Dotti, M., & Read, J. I. 2018a, MNRAS, 477, 2310, doi: 10.1093/mnras/sty775
—. 2018b, MNRAS, 477, 2310, doi: 10.1093/mnras/sty775
Bortolas, E., Gualandris, A., Dotti, M., Spera, M., & Mapelli, M. 2016, Monthly Notices of the Royal Astronomical Society, 461, 1023
Bournaud, F., Jog, C. J., & Combes, F. 2007, Astronomy & Astrophysics, 476, 1179
Boylan-Kolchin, M., Ma, C.-P., & Quataert, E. 2004, The Astrophysical Journal, 613, L37
Brown, R. L. 1982, ApJ, 262, 110, doi: 10.1086/160401
Byun, Y.-I., Grillmair, C. J., Faber, S., et al. 1996, arXiv preprint astro-ph/9602117
Campanelli, M. 2005, Classical and Quantum Gravity, 22, S387
Campanelli, M., Lousto, C., Zlochower, Y., & Merritt, D. 2007a, The Astrophysical Journal, 659, L5
Campanelli, M., Lousto, C. O., Zlochower, Y., & Merritt, D. 2007b, Physical Review Letters, 98, 231102
Caon, N., Capaccioli, M., & D'Onofrio, M. 1993, Monthly Notices of the Royal Astronomical Society, 265, 1013
Capuzzo-Dolcetta, R., & Mastrobuono-Battisti, A. 2009, Astronomy & Astrophysics, 507, 183

Capuzzo-Dolcetta, R., & Miocchi, P. 2008, Monthly Notices of the Royal Astronomical Society: Letters, 388, L69

Carollo, C., Stiavelli, M., De Zeeuw, P., & Mack, J. 1997, Astronomical Journal v. 114, p. 2366, 114, 2366

Carollo, C. M., Stiavelli, M., Seigar, M., de Zeeuw, P. T., & Dejonghe, H. 2002, The Astronomical Journal, 123, 159

Celoria, M., Oliveri, R., Sesana, A., & Mapelli, M. 2018, arXiv preprint arXiv:1807.11489

Chandrasekhar, S. 1943, Astrophysical Journal, 97, 255

Clausius, R. 1870, The London, Edinburgh, and Dublin Philosophical Magazine and Journal of Science, 40, 122

Correa, C. A., & Schaye, J. 2020, Monthly Notices of the Royal Astronomical Society, 499, 3578

Côté, P., Piatek, S., Ferrarese, L., et al. 2006, The Astrophysical Journal Supplement Series, 165, 57

Couch, W. J., Barger, A. J., Smail, I., Ellis, R. S., & Sharples, R. M. 1998, The Astrophysical Journal, 497, 188

Damour, T., & Gopakumar, A. 2006, Physical Review D—Particles, Fields, Gravitation, and Cosmology, 73, 124006

Davidson, P. A. 2017, Introduction to magnetohydrodynamics, Vol. 55 (Cambridge university press)

Davies, R. L., Efstathiou, G., Fall, S. M., Illingworth, G., & Schechter, P. L. 1983, ApJ, 266, 41, doi: `10.1086/160757`

Davis, M., & Geller, M. J. 1976, ApJ, 208, 13, doi: `10.1086/154575`

de Vaucouleurs, G. 1948, in Annales d'Astrophysique, Vol. 11, 247

de Vaucouleurs, G., & Capaccioli, M. 1979, ApJS, 40, 699, doi: `10.1086/190602`

de Zeeuw, T. 1985, Monthly Notices of the Royal Astronomical Society, 216, 273

Dehnen, W. 2000, The Astrophysical Journal, 536, L39

—. 2002, Journal of Computational Physics, 179, 27

—. 2005, Monthly Notices of the Royal Astronomical Society, 360, 892

—. 2014, Computational Astrophysics and Cosmology, 1, 1

Dehnen, W., & Read, J. I. 2011, The European Physical Journal Plus, 126, 55

Den Brok, M., Peletier, R. F., Seth, A., et al. 2014, Monthly Notices of the Royal Astronomical Society, 445, 2385

Djorgovski, S., & Davis, M. 1987, Astrophysical Journal, Part 1 (ISSN 0004-637X), vol. 313, Feb. 1, 1987, p. 59-68., 313, 59

Dosopoulou, F., Greene, J. E., & Ma, C.-P. 2021, The Astrophysical Journal, 922, 40

Dressler, A. 1980, ApJ, 236, 351, doi: `10.1086/157753`

Dressler, A., Lynden-Bell, D., Burstein, D., et al. 1987, Astrophysical Journal, Part 1 (ISSN 0004-637X), vol. 313, Feb. 1, 1987, p. 42-58., 313, 42

Dressler, A., & Richstone, D. O. 1988, The Astrophysical Journal, 324, 701

Driver, S. P., Popescu, C. C., Tuffs, R. J., et al. 2007, Monthly Notices of the Royal Astronomical Society, 379, 1022

Dullo, B., Knapen, J., Baldi, R., et al. 2024, Monthly Notices of the Royal Astronomical Society, 532, 4729

Dullo, B. T. 2019, The Astrophysical Journal, 886, 80

Dullo, B. T., de Paz, A. G., & Knapen, J. H. 2021, The Astrophysical Journal, 908, 134

Dullo, B. T., & Graham, A. W. 2014, Monthly Notices of the Royal Astronomical Society, 444, 2700

Dullo, B. T., Graham, A. W., & Knapen, J. H. 2017, Monthly Notices of the Royal Astronomical Society, 471, 2321

Dutton, A. A., & Maccio, A. V. 2014, Monthly Notices of the Royal Astronomical Society, 441, 3359

Ebisuzaki, T., Makino, J., & Okumura, S. 1991, Nature, 354, 212

Eckart, A., & Genzel, R. 1997, Monthly Notices of the Royal Astronomical Society, 284, 576

Eddington, A. 1916, Monthly Notices of the Royal Astronomical Society, 76, 572

Eddington, A. S. 1926, The Internal Constitution of the Stars (Cambridge, UK: Cambridge University Press)

Eggen, O., Lynden-Bell, D., & Sandage, A. 1962, Astrophysical Journal, vol. 136, p. 748, 136, 748

Enoki, M., Inoue, K. T., Nagashima, M., & Sugiyama, N. 2004, The Astrophysical Journal, 615, 19

Euler, L. 1767, Novi commentarii academiae scientiarum Petropolitanae, 144

Event Horizon Telescope Collaboration, Akiyama, K., Alberdi, A., et al. 2019, ApJ, 875, L1, doi: 10.3847/2041-8213/ab0ec7

—. 2022, ApJ, 930, L12, doi: 10.3847/2041-8213/ac6674

Faber, S. M., & Jackson, R. E. 1976, ApJ, 204, 668, doi: 10.1086/154215

Faber, S. M., Tremaine, S., Ajhar, E. A., et al. 1996, arXiv preprint astro-ph/9610055

Fahrion, K., Lyubenova, M., Van De Ven, G., et al. 2021, Astronomy & Astrophysics, 650, A137

Farouki, R. T., Shapiro, S. L., & Duncan, M. J. 1983, Astrophysical Journal, Part 1, vol. 265, Feb. 15, 1983, p. 597-605., 265, 597

Fastidio, F., Gualandris, A., Sesana, A., Bortolas, E., & Dehnen, W. 2024, Monthly Notices of the Royal Astronomical Society, stae1411

Fastidio, F., Gualandris, A., Sesana, A., Bortolas, E., & Dehnen, W. 2024, MNRAS, 532, 295, doi: 10.1093/mnras/stae1411

Ferrarese, L., & Merritt, D. 2000, The Astrophysical Journal, 539, L9

Ferrarese, L., van den Bosch, F. C., Ford, H. C., Jaffe, W., & O'Connell, R. W. 1994, The Astronomical Journal, 108, 1598

Ferrarese, L., Côté, P., Dalla Bontà, E., et al. 2006, The Astrophysical Journal, 644, L21

Ferreira, L., Adams, N., Conselice, C. J., et al. 2022, arXiv preprint arXiv:2207.09428

Fitchett, M. 1983, Monthly Notices of the Royal Astronomical Society, 203, 1049

Flanagan, E. E., & Hughes, S. A. 2005, New Journal of Physics, 7, 204

Foster III, R. S. 1990, Constructing a pulsar timing array (University of California, Berkeley)

Frigo, M., Naab, T., Rantala, A., et al. 2021, Monthly Notices of the Royal Astronomical Society, 508, 4610

Gamow, G. 1954, Proceedings of the National Academy of Sciences, 40, 480

Gebhardt, K., Bender, R., Bower, G., et al. 2000, The Astrophysical Journal, 539, L13

Geha, M., Guhathakurta, P., & Van Der Marel, R. 2002, The Astronomical Journal, 124, 3073

Georgakakis, A., Hopkins, A., Caulton, A., et al. 2001, Monthly Notices of the Royal Astronomical Society, 326, 1431

Georgiev, I. Y., Böker, T., Leigh, N., Lützgendorf, N., & Neumayer, N. 2016, Monthly Notices of the Royal Astronomical Society, 457, 2122

Georgiev, I. Y., Hilker, M., Puzia, T. H., Goudfrooij, P., & Baumgardt, H. 2009, Monthly Notices of the Royal Astronomical Society, 396, 1075

Gnedin, O. Y., Ostriker, J. P., & Tremaine, S. 2014, The Astrophysical Journal, 785, 71

Goerdt, T., Moore, B., Read, J., & Stadel, J. 2010, The Astrophysical Journal, 725, 1707

Gonzalez, J. A., Sperhake, U., Bruegmann, B., Hannam, M., & Husa, S. 2007, Physical Review Letters, 98, 091101

Goulding, A. D., Greene, J. E., Ma, C.-P., et al. 2016, The Astrophysical Journal, 826, 167

Graham, A. W., & Driver, S. P. 2007, The Astrophysical Journal, 655, 77

Graham, A. W., Erwin, P., Caon, N., & Trujillo, I. 2001, The Astrophysical Journal, 563, L11

Graham, A. W., Erwin, P., Trujillo, I., & Ramos, A. A. 2003, The Astronomical Journal, 125, 2951

Graham, A. W., & Scott, N. 2013, The Astrophysical Journal, 764, 151

Gray, E. I., Read, J. I., Taylor, E., et al. 2024, arXiv preprint arXiv:2405.19286

Greene, J. E., & Ho, L. C. 2006, The Astrophysical Journal, 641, L21

Greengard, L., & Rokhlin, V. 1987, Journal of computational physics, 73, 325

Gualandris, A., Khan, F. M., Bortolas, E., et al. 2022, Monthly Notices of the Royal Astronomical Society, 511, 4753

Gualandris, A., & Merritt, D. 2008, The Astrophysical Journal, 678, 780

—. 2011, The Astrophysical Journal, 744, 74

Gualandris, A., & Merritt, D. 2012, ApJ, 744, 74, doi: 10.1088/0004-637X/744/1/74

Gualandris, A., Read, J. I., Dehnen, W., & Bortolas, E. 2017, Monthly Notices of the Royal Astronomical Society, 464, 2301

Gültekin, K., Richstone, D. O., Gebhardt, K., et al. 2009, The Astrophysical Journal, 698, 198

Guth, A. H. 1981, Physical Review D, 23, 347

Guth, A. H., & Pi, S.-Y. 1982, Physical Review Letters, 49, 1110

Harris, W. E. 2010, arXiv preprint arXiv:1012.3224

Hartmann, M., Debattista, V. P., Seth, A., Cappellari, M., & Quinn, T. R. 2011, Monthly Notices of the Royal Astronomical Society, 418, 2697

Hawking, S., & Israel, W., eds. 1979, General Relativity: An Einstein Centenary Survey (Cambridge University Press)

Heggie, D. C. 1974, Celestial mechanics, 10, 217

Herrmann, F., Hinder, I., Shoemaker, D., & Laguna, P. 2007, Classical and Quantum Gravity, 24, S33

Herschel, J. F. 1847, Results of Astronomical Observations Made During the Years 1834, 5, 6, 7, 8, at the Cape of Good Hope; Being the Completion of a Telescopic Survey of the Whole Surface of the Visible Heavens, Commenced in 1825 (Smith, Elder and Company)

Hey, J. S., Parsons, S. J., & Phillips, J. W. 1946, Nature, 158, 234, doi: 10.1038/158234a0

Hills, J. 1983, Astronomical Journal (ISSN 0004-6256), vol. 88, Aug. 1983, p. 1269-1283., 88, 1269

Hodge, P. W. 1963, AJ, 68, 691, doi: 10.1086/109196

Holmberg, E. 1941, Astrophysical Journal, vol. 94, p. 385, 94, 385

Hoyle, F. 1953, Astrophysical Journal, vol. 118, p. 513, 118, 513

Hoyle, F., Burgers, J., & van De Hulst, H. 1949, Central Air Documents, Office, Dayton, OH

Hubble, E. 1929, Proceedings of the national academy of sciences, 15, 168

—. 1936, Realm of the Nebulae. Yale University Press, New Haven

Hubble, E. P. 1926, The Astrophysical Journal, 64

—. 1930, The Astrophysical Journal, 71
Iwasawa, M., Funato, Y., & Makino, J. 2006, The Astrophysical Journal, 651, 1059
Jaffe, W., Ford, H. C., Ferrarese, L., van den Bosch, F., & O'Connell, R. W. 1993, Nature, 364, 213
Jeans, J. 1928, Astronomy and cosmogony, Cambridge University, Cambridge Press
Jeans, J. H. 1915, Monthly Notices of the Royal Astronomical Society, Vol. 76, p. 70-84, 76, 70
Kashlinsky, A., & Rees, M. 1983, Monthly Notices of the Royal Astronomical Society, 205, 955
Kerr, R. P. 1963, Physical review letters, 11, 237
Khan, F. M., Just, A., & Merritt, D. 2011, The Astrophysical Journal, 732, 89
Khochfar, S., & Burkert, A. 2003, The Astrophysical Journal, 597, L117
—. 2006, Astronomy & Astrophysics, 445, 403
Khonji, N., Gualandris, A., Read, J. I., & Dehnen, W. 2024, The Astrophysical Journal, 974, 204
King, I. 1978, The Astrophysical Journal, 222, 1
King, I. R. 1966, The Astronomical Journal, 71, 64
Kormendy, J. 1977, ApJ, 218, 333, doi: 10.1086/155687
Kormendy, J. 1985, Astrophysical Journal, Part 2-Letters to the Editor (ISSN 0004-637X), vol. 292, May 1, 1985, p. L9-L13., 292, L9
Kormendy, J., & Bender, R. 1996, The Astrophysical Journal, 464, L119
Kormendy, J., Bender, R., & Cornell, M. 2011, Nature, 469, 374
Kormendy, J., Fisher, D. B., Cornell, M. E., & Bender, R. 2009, The Astrophysical Journal Supplement Series, 182, 216
Kormendy, J., & Kennicutt Jr, R. C. 2004, Annu. Rev. Astron. Astrophys., 42, 603
Kormendy, J., & Sanders, D. B. 1992, Astrophysical Journal, Part 2-Letters (ISSN 0004-637X), vol. 390, no. 2, May 10, 1992, p. L53-L56., 390, L53
Kulkarni, G., & Loeb, A. 2012, Monthly Notices of the Royal Astronomical Society, 422, 1306
Kuo, C., Braatz, J., Condon, J., et al. 2010, The Astrophysical Journal, 727, 20
Kustaanheimo, P., Schinzel, A., Davenport, H., & Stiefel, E. 1965
Lagos, C. d. P., Stevens, A. R., Bower, R. G., et al. 2018, Monthly Notices of the Royal Astronomical Society, 473, 4956
Lagrange, J.-L. 1772, Prix de l'académie royale des Sciences de paris, 9, 292
Latif, M. A., & Ferrara, A. 2016, Publications of the Astronomical Society of Australia, 33, e051
Lauer, T. R. 1985, The Astrophysical Journal, 292, 104
Lauer, T. R., Ajhar, E. A., Byun, Y.-I., et al. 1995, The Astronomical Journal, 110, 2622
Lauer, T. R., Faber, S., Gebhardt, K., et al. 2005, The Astronomical Journal, 129, 2138
Lauer, T. R., Gebhardt, K., Faber, S. M., et al. 2007, ApJ, 664, 226, doi: 10.1086/519229
Lauer, T. R., Faber, S., Richstone, D., et al. 2007, The Astrophysical Journal, 662, 808
Lemaître, G. 1931, Nature, 127, 706
Lin, C. C., & Shu, F. H. 1964, ApJ, 140, 646, doi: 10.1086/147955
Liu, Q., Van Paradijs, J., & Van Den Heuvel, E. 2006, Astronomy & Astrophysics, 455, 1165
—. 2007, Astronomy & Astrophysics, 469, 807
Liu, X., Shen, Y., & Strauss, M. A. 2011, The Astrophysical Journal Letters, 736, L7
Loewenstein, M., & White III, R. E. 1999, The Astrophysical Journal, 518, 50

Loose, H., Kruegel, E., & Tutukov, A. 1982, Astronomy and Astrophysics, vol. 105, no. 2, Jan. 1982, p. 342-350. Research supported by the Deutsche Forschungsgemeinschaft., 105, 342

Lotz, J. M., Telford, R., Ferguson, H. C., et al. 2001, The Astrophysical Journal, 552, 572

Lousto, C. O., & Healy, J. 2019, Physical Review D, 100, 104039

Lousto, C. O., & Zlochower, Y. 2008, Physical Review D, 77, 024034

—. 2011, Physical Review Letters, 107, 231102

Lynden-Bell, D. 1967, Monthly Notices of the Royal Astronomical Society, Vol. 136, p. 101, 136, 101

—. 1969, Nature, 223

Macchetto, F., Marconi, A., Axon, D. J., et al. 1997, The Astrophysical Journal, 489, 579

Magorrian, J., Tremaine, S., Richstone, D., et al. 1998, The Astronomical Journal, 115, 2285

Makino, J. 1991, Publications of the Astronomical Society of Japan, v. 43, p. 859-876., 43, 859

Makino, J., & Funato, Y. 2004, The Astrophysical Journal, 602, 93

Marconi, A., & Hunt, L. K. 2003, The Astrophysical Journal, 589, L21

Matthews, T. A., Morgan, W. W., & Schmidt, M. 1964, Astrophysical Journal, vol. 140, p. 35, 140, 35

Matthews, T. A., & Sandage, A. R. 1963, Astrophysical Journal, vol. 138, p. 30, 138, 30

McConnell, N. J., & Ma, C.-P. 2013, The Astrophysical Journal, 764, 184

McConnell, N. J., Ma, C.-P., Gebhardt, K., et al. 2011, Nature, 480, 215

McLure, R. J., & Dunlop, J. 2002, Monthly Notices of the Royal Astronomical Society, 331, 795

Merritt, D. 2001, The Astrophysical Journal, 556, 245

—. 2006, The Astrophysical Journal, 648, 976

—. 2013, Classical and Quantum Gravity, 30, 244005

Merritt, D., Milosavljević, M., Favata, M., Hughes, S. A., & Holz, D. E. 2004, The Astrophysical Journal, 607, L9

Merritt, D., Schnittman, J. D., & Komossa, S. 2009, The Astrophysical Journal, 699, 1690

Michell, J. 1784, Philosophical transactions of the Royal Society of London, 35

Mihos, J. C., & Hernquist, L. 1994, Astrophysical Journal, Part 2-Letters (ISSN 0004-637X), vol. 437, no. 1, p. L47-L50, 437, L47

—. 1996, The Astrophysical Journal, 464, 641

Mikkola, S., & Aarseth, S. J. 1989, Celestial Mechanics and Dynamical Astronomy, 47, 375

Milosavljević, M., & Merritt, D. 2001, The Astrophysical Journal, 563, 34

Milosavljević, M., & Merritt, D. 2003in , American Institute of Physics, 201–210

Miyoshi, M., Moran, J., Herrnstein, J., et al. 1995, nature, 373, 127

Moore, B., Katz, N., Lake, G., Dressler, A., & Oemler, A. 1996, nature, 379, 613

Mortlock, D. J., Warren, S. J., Venemans, B. P., et al. 2011, Nature, 474, 616

Muñoz, R. P., Eigenthaler, P., Puzia, T. H., et al. 2015, The Astrophysical Journal Letters, 813, L15

Naab, T., Johansson, P. H., & Ostriker, J. P. 2009, The Astrophysical Journal, 699, L178

Naab, T., Khochfar, S., & Burkert, A. 2006, The Astrophysical Journal, 636, L81

Nasim, I. T., Gualandris, A., Read, J. I., et al. 2021, Monthly Notices of the Royal Astronomical Society, 502, 4794

Navarro, J. F., & Benz, W. 1991, Astrophysical Journal, Part 1 (ISSN 0004-637X), vol. 380, Oct. 20, 1991, p. 320-329. Research supported by SNSF and CONICET., 380, 320

Navarro, J. F., Frenk, C. S., & White, S. D. 1997, The Astrophysical Journal, 490, 493

Navarro, J. F., & White, S. D. 1993, Monthly Notices of the Royal Astronomical Society, 265, 271

Neumayer, N., Seth, A., & Böker, T. 2020, The Astronomy and Astrophysics Review, 28, 4

Neumayer, N., Walcher, C. J., Andersen, D., et al. 2011, Monthly Notices of the Royal Astronomical Society, 413, 1875

Oemler, Jr., A. 1974, ApJ, 194, 1, doi: 10.1086/153216

Peebles, P. 1972, The Astrophysical Journal, 178, 371

—. 1982, Astrophysical Journal, Letters to the Editor, 263, L1

Peebles, P. J. E. 1965, Astrophysical Journal, vol. 142, p. 1317, 142, 1317

Penzias, A., & Wilson, R. 1965, Astrophysical Journal, vol. 142, p. 419-421, 142, 419

Perlmutter, S., Aldering, G., Goldhaber, G., et al. 1999, The Astrophysical Journal, 517, 565

Peters, P. C., & Mathews, J. 1963, Physical Review, 131, 435

Peterson, B. M. 1993, Publications of the Astronomical Society of the Pacific, 105, 247

Plummer, H. C. 1911, Monthly Notices of the Royal Astronomical Society, Vol. 71, p. 460-470, 71, 460

Pontzen, A., Roškar, R., Stinson, G. S., et al. 2013, pynbody: Astrophysics Simulation Analysis for Python

Portegies Zwart, S. F., Baumgardt, H., Hut, P., Makino, J., & McMillan, S. L. 2004, Nature, 428, 724

Postman, M., Lauer, T. R., Donahue, M., et al. 2012, The Astrophysical Journal, 756, 159

Press, W. H. 1971, Astrophysical Journal, vol. 170, p. L105, 170, L105

Press, W. H., & Schechter, P. 1974, Astrophysical Journal, Vol. 187, pp. 425-438 (1974), 187, 425

Pretorius, F. 2005, Physical review letters, 95, 121101

Quinlan, G. D. 1996, New Astronomy, 1, 35

Quinlan, G. D., & Hernquist, L. 1997, New Astronomy, 2, 533

Rantala, A., Johansson, P. H., Naab, T., Thomas, J., & Frigo, M. 2018, The Astrophysical Journal, 864, 113

Ravi, V., Wyithe, J., Shannon, R., Hobbs, G., & Manchester, R. 2014, Monthly Notices of the Royal Astronomical Society, 442, 56

Rawlings, A., Keitaanranta, A., Mattero, M., et al. 2025, Monthly Notices of the Royal Astronomical Society, staf238

Read, J., Goerdt, T., Moore, B., et al. 2006, Monthly Notices of the Royal Astronomical Society, 373, 1451

Read, J., & Trentham, N. 2005, Philosophical Transactions of the Royal Society A: Mathematical, Physical and Engineering Sciences, 363, 2693

Reardon, D. J., Zic, A., Shannon, R. M., et al. 2023, The Astrophysical Journal Letters, 951, L6

Redmount, I., & Rees, M. 1989, Comments on Astrophysics, 14, 165

Rees, M. J., & Ostriker, J. 1977, Monthly Notices of the Royal Astronomical Society, 179, 541

Regan, J., & Volonteri, M. 2024, arXiv preprint arXiv:2405.17975

Rest, A., Van Den Bosch, F. C., Jaffe, W., et al. 2001, The Astronomical Journal, 121, 2431

Richstone, D. O., & Tremaine, S. 1988, Astrophysical Journal, Part 1 (ISSN 0004-637X), vol. 327, April 1, 1988, p. 82-88., 327, 82

Riess, A. G., Filippenko, A. V., Challis, P., et al. 1998, The astronomical journal, 116, 1009

Rindler, W. 1956, Monthly Notices of the Royal Astronomical Society, 116, 662

Robinson, D. C. 1975, Physical Review Letters, 34, 905

Rossa, J., Van der Marel, R. P., Böker, T., et al. 2006, The Astronomical Journal, 132, 1074

Rubin, V. C., Ford, Jr., W. K., & D'Odorico, S. 1970, ApJ, 160, 801, doi: 10.1086/150473

Rubin, V. C., & Ford Jr, W. K. 1970, Astrophysical Journal, vol. 159, p. 379, 159, 379

Rubin, V. C., Ford Jr, W. K., & Thonnard, N. 1980, Astrophysical Journal, Part 1, vol. 238, June 1, 1980, p. 471-487., 238, 471

Rusli, S., Erwin, P., Saglia, R., et al. 2013, The Astronomical Journal, 146, 160

Sachs, R. K. 1962, Proceedings of the Royal Society of London. Series A. Mathematical and Physical Sciences, 270, 103

Sadowski, A. 2009, The Astrophysical Journal Supplement Series, 183, 171

Saitoh, T. R., & Makino, J. 2012, New Astronomy, 17, 76

Salpeter, E. 1964, Publications, 1, 165

Sampson, L., Cornish, N. J., & McWilliams, S. T. 2015, Physical Review D, 91, 084055

Sánchez-Janssen, R., Côté, P., Ferrarese, L., et al. 2019, The Astrophysical Journal, 878, 18

Saracco, P., Marchesini, D., La Barbera, F., et al. 2020, The Astrophysical Journal, 905, 40

Sargent, W. L. W., Young, P. J., Boksenberg, A., et al. 1978, ApJ, 221, 731, doi: 10.1086/156077

Schechter, P. L. 1980, AJ, 85, 801, doi: 10.1086/112742

Schinnerer, E., Böker, T., Emsellem, E., & Lisenfeld, U. 2006, The Astrophysical Journal, 649, 181

Schmidt, M. 1963, A Century of Nature, Twenty One Discoveries That Changed Science and the World

Schnittman, J. D., & Buonanno, A. 2007, The Astrophysical Journal, 662, L63

Schödel, R., Merritt, D., & Eckart, A. 2009, Astronomy & Astrophysics, 502, 91

Schwarzschild, K. 1916, Sitzungsberichte der königlich preussischen Akademie der Wissenschaften, 189

Scott, N., & Graham, A. W. 2013, The Astrophysical Journal, 763, 76

Scott, N., Graham, A. W., & Schombert, J. 2013, The Astrophysical Journal, 768, 76

Sérsic, J. 1963, Boletin de la Asociacion Argentina de Astronomia La Plata Argentina, 6, 41

Sesana, A. 2013a, Classical and Quantum Gravity, 30, 224014

—. 2013b, Classical and Quantum Gravity, 30, 244009

Sesana, A., Haardt, F., & Madau, P. 2006, The Astrophysical Journal, 651, 392

Sesana, A., Haiman, Z., Kocsis, B., & Kelley, L. Z. 2018, The Astrophysical Journal, 856, 42

Seth, A., Agüeros, M., Lee, D., & Basu-Zych, A. 2008, The Astrophysical Journal, 678, 116

Seyfert, C. K. 1943, ApJ, 97, 28, doi: 10.1086/144488

Shakura, N. I., & Sunyaev, R. A. 1973, Astronomy and Astrophysics, Vol. 24, p. 337-355, 24, 337

Shlosman, I., Begelman, M. C., & Frank, J. 1990, Nature, 345, 679

Shull, J. M., Smith, B. D., & Danforth, C. W. 2012, The Astrophysical Journal, 759, 23

Silk, J. 1968, Nature, 218, 453

Slipher, V. M. 1917, Lowell Observatory Bulletin, 3, 59

Smoluchowski, M. 1906, Essai d'une théorie cinétique du mouvement Brownien et des milieux troublés (Acad. Litterarum Cracoviensis)

Sopuerta, C. F., Yunes, N., & Laguna, P. 2006, Physical Review D—Particles, Fields, Gravitation, and Cosmology, 74, 124010

Spengler, C., Côté, P., Roediger, J., et al. 2017, The Astrophysical Journal, 849, 55

Springel, V. 2010, Annual Review of Astronomy and Astrophysics, 48, 391

Starobinsky, A. A. 1982, Physics Letters B, 117, 175

Strömberg, G. 1934, Astrophysical Journal, vol. 80, p. 327, 80, 327

Terlevich, A. I., & Forbes, D. A. 2002, Monthly Notices of the Royal Astronomical Society, 330, 547

Thacker, R. J., & Couchman, H. M. P. 2001, ApJ, 555, L17, doi: 10.1086/321739

Thanjavur, K., Simard, L., Bluck, A. F., & Mendel, T. 2016, Monthly Notices of the Royal Astronomical Society, 459, 44

Thomas, D., Maraston, C., Bender, R., & De Oliveira, C. M. 2005, The Astrophysical Journal, 621, 673

Thomas, J., Ma, C.-P., McConnell, N. J., et al. 2016, Nature, 532, 340

Thomas, J., Saglia, R., Bender, R., Erwin, P., & Fabricius, M. 2014, The Astrophysical Journal, 782, 39

Thorne, K. S. 1974, Astrophysical Journal, Vol. 191, pp. 507-520 (1974), 191, 507

Tinsley, B. 1978, Astrophysical Journal, Part 1, vol. 222, May 15, 1978, p. 14-22. Research supported by the Alfred P. Sloan Foundation, 222, 14

Toomre, A., & Toomre, J. 1972, Astrophysical Journal, Vol. 178, pp. 623-666 (1972), 178, 623

Tremaine, S., Gebhardt, K., Bender, R., et al. 2002, The Astrophysical Journal, 574, 740

Tremaine, S. D., Ostriker, J., & Spitzer Jr, L. 1975, Astrophysical Journal, vol. 196, Mar. 1, 1975, pt. 1, p. 407-411., 196, 407

Tremonti, C. A., Heckman, T. M., Kauffmann, G., et al. 2004, The Astrophysical Journal, 613, 898

Umemura, M., Loeb, A., & Turner, E. L. 1993, arXiv preprint astro-ph/9303004

Valtaoja, L., Valtonen, M., & Byrd, G. 1989, Astrophysical Journal, Part 1 (ISSN 0004-637X), vol. 343, Aug. 1, 1989, p. 47-53. Research supported by the Academy of Finland., 343, 47

van Dokkum, P. G., & Conroy, C. 2010, nature, 468, 940

Van Dokkum, P. G., Franx, M., Kriek, M., et al. 2008, The Astrophysical Journal, 677, L5

Vasiliev, E. 2019, Monthly Notices of the Royal Astronomical Society, 482, 1525

Vasiliev, E., Antonini, F., & Merritt, D. 2014, ApJ, 785, 163, doi: 10.1088/0004-637X/785/2/163

Vasiliev, E., Antonini, F., & Merritt, D. 2015, The Astrophysical Journal, 810, 49

Vasiliev, E., Antonini, F., & Merritt, D. 2015, ApJ, 810, 49, doi: 10.1088/0004-637X/810/1/49

Verolme, E., Cappellari, M., Copin, Y., et al. 2002, Monthly Notices of the Royal Astronomical Society, 335, 517

Von Weizsäcker, C. 1951, Astrophysical Journal, vol. 114, p. 165, 114, 165

Wang, F., Yang, J., Fan, X., et al. 2019, The Astrophysical Journal, 884, 30

—. 2021, The Astrophysical Journal Letters, 907, L1

Weinberg, S. 1972, New York

Wheeler, J. A. 1968, The American Scholar, 248

White, S. D., Frenk, C. S., & Davis, M. 1983, Astrophysical Journal, Part 2-Letters to the Editor (ISSN 0004-637X), vol. 274, Nov. 1, 1983, p. L1-L5., 274, L1

White, S. D., & Rees, M. J. 1978, Monthly Notices of the Royal Astronomical Society, 183, 341

Whitmore, B. C., & Schweizer, F. 1995, AJ, 109, 960, doi: 10.1086/117334

Wiklind, T., Combes, F., & Henkel, C. 1995, Astronomy and Astrophysics, 297, 643

Williams, R. E., Blacker, B., Dickinson, M., et al. 1996, The Astronomical Journal, 112, 1335

Woosley, S., & Heger, A. 2021, The Astrophysical Journal Letters, 912, L31

Worthey, G. 1994, The Astrophysical Journal Supplement Series, 95, 107

Xiao, T., Barth, A. J., Greene, J. E., et al. 2011, The Astrophysical Journal, 739, 28

Xu, H., Chen, S., Guo, Y., et al. 2023, arXiv preprint arXiv:2306.16216

Young, P. J., Westphal, J. A., Kristian, J., Wilson, C. P., & Landauer, F. P. 1978, Astrophysical Journal, Part 1, vol. 221, May 1, 1978, p. 721-730., 221, 721

Zwicky, F. 1933, Helvetica Physica Acta, Vol. 6, p. 110-127, 6, 110